AN EXPERIMENTAL AND COMPUTATIONAL ANALYSIS OF AIRFLOW MIXING AT THE INTERFACE OF THE BUILT ENVIRONMENT

A Dissertation

by

PAUL HENRY NAGY

Submitted to the Office of Graduate and Professional Studies of
Texas A&M University
in partial fulfillment of the requirements for the degree of

DOCTOR OF PHILOSOPHY

Chair of Committee	Michael B. Pate
Committee Members	Jorge L. Alvarado
	Jonathan R. Felts
	Bryan P. Rasmussen
Head of Department	Andreas A. Polycarpou

December 2020

Major Subject: Mechanical Engineering

ABSTRACT

Performance enhancements of HVAC systems are paramount for designers and manufacturers, as HVAC accounts for nearly 50% of energy use in the United States. Building energy reductions mandated by ASHRAE standards have raised predictions for the global heat and energy recover ventilator (HERV's) market to surpass $4 billion USD by 2023. A major factor in HERV design and installation is the proximate placement of the exhaust and intake ports to mitigate excessive duct lengths and pressure losses. Presently there are no standards or past studies concerning residential HERV exhaust or intake placement and its effect on airstream mixing.

The research presented herein is a major contribution to advancing HERV technology as locational factors affecting exhaust-to-intake airflow mixing are evaluated for the first time. In support of this endeavor, a novel testing facility was designed, constructed, and used to experimentally collect mixing data for 9 distinct intake and exhaust geometries at 4 volumetric flowrates. The significance being that optimal placements of the exhaust and intake were determined with intentions of mitigating undesirable mixing from the exhaust air to the intake, common with HERV installations. Mixing, or crossover, is defined as a ratio of the concentration of injected carbon dioxide in the exhaust duct to the intake duct. The experimental data revealed a wide crossover range for vertically aligned ducts, revealing maximums and minimums of 76.8% and 6.3%, while horizontally aligned ducts revealed a narrower range of 14.0% and 10.2%, respectively.

Mixing was simulated using CFD and the maximum differences in crossover between the experimental and CFD simulations were -3.3% and 3.0% for the vertical and horizontal alignment, while minimum differences for the same geometries were -1.1% and -0.8%, respectively. Upon verification of the CFD model, low-temperature CFD simulations provided air enthalpy values to calculate and predict energy savings, which were shown to vary between 9W and 1.39kW for ERV applications.

The above residential intake and exhaust mixing results identified in this research study are of upmost importance to system designers, and they are foundational for maintaining occupant comfort and health within existing standards while also further reducing HVAC system energy usage.

DEDICATION

This dissertation is dedicated to my parents for their encouragement and support throughout my academic career.

CONTRIBUTORS AND FUNDING SOURCES

Contributors

This work was supported by a graduate committee consisting of Dr. Pate (Chair), Dr. Felts and Dr. Rasmussen of the Department of Mechanical Engineering and Dr. Alvarado of the Department of Engineering Technology and Industrial Distribution.

All work conducted for this thesis was completed by the student independently.

Funding Sources

This dissertation and associated research were supported by the RELLIS Energy Efficiency Laboratory (REEL) at Texas A&M University

TABLE OF CONTENTS

Page

LIST OF FIGURES

LIST OF TABLES

Page

CHAPTER I

INTRODUCTION

Commercial and residential buildings accounted for approximately 40 percent of the total energy consumption in the United States of America in 2015, equating to 39 quadrillion BTU’s (EIA 2016). A survey conducted in 2009 revealed that residential heating and cooling combined accounted for 47.7% of the total energy use in the USA (EIA 2009). With building HVAC applications responsible for almost half of all the annual energy use, advancements to improve the efficiency of HVAC technology and systems can have a significant effect on the discharge of carbon dioxide to earth’s atmosphere. One such technology that has demonstrated promise for reductions in future building energy use is the ERV, otherwise known as the Energy Recovery Ventilator. Of special importance, ASHRAE 62.1 Ventilation for Acceptable Indoor Air Quality has driven the implementation of Energy Recovery Ventilators (ERV’s) in conjunction with ASHRAE 90.1 Energy Standard for Buildings Except Low-Rise Residential Buildings, requiring 50% enthalpy recovery effectiveness, and ASHRAE 189.1 Standard for the Design of High-Performance Green Buildings Except Low-Rise Residential Buildings, requiring 60% enthalpy recovery effectiveness, with these values being climate region, and system size specific.

For proper operation ERV’s require both an exhaust and intake duct that are in close vicinity to each other. In this regard, the objective of the research herein is to investigate and quantify the effects of exhaust and intake parameters such as spacing, geometry, and orientations on flow mixing at an outdoor building interface for the purpose of optimizing these parameters. The data to be collected and analyzed in support of this research objective will be obtained experimentally by recording and analyzing data measurements from a novel experimental test setup. Therefore, an important step in achieving the research objective was the design and construction of a novel test facility to accommodate the airflow mixing experiments. This facility primarily focuses on achieving maximum volumetric flowrates and carbon dioxide concentrations of 250 cubic feet per minute (cfm) and 2,000 parts-per-million (ppm), respectively, in a 6-inch duct, which is the standard duct size for most residential ERV's.

In addition to the experimental tests, ANSYS Fluent 19.2, a Computational Fluid Dynamics (CFD) software package, was used to simulate the intake and exhaust geometries and experimental flows. The CFD was used for studies of equivalent temperature test conditions (equal exhaust and ambient temperatures), which are in-line with the experimental setup, and in addition to low temperature environmental conditions, which are not readily achievable with experiments. An analysis regarding the impact of the exhaust-to-intake mixing on ERV apparent effectiveness resulting from the low-temperature CFD simulations will also be presented in order to quantify and predict the performance increase or decrease to a system when used in conjunction with an ERV.

CHAPTER II

BACKGROUND

Because of the large amount of energy used by HVAC systems to overcome uncontrolled outdoor air infiltration, energy efficiency implementations in building construction science have focused on making buildings tighter. As a result of these buildings constructed to tighter standards, uncontrolled infiltration is avoided as it produces inadequate fresh air from an Indoor Air Quality (IAQ) standpoint. One solution being implemented to supply fresh, adequate air from the outside, in an energy efficient manner, consists of utilizing energy recovery. This energy recovery is made possible by Heat Recovery Ventilators (HRV) and Energy/Enthalpy Recovery Ventilators (ERV) in conjunction with a standard HVAC system.

HERV's (signifying either an HRV or ERV), are ideal solutions for recovering energy from stale exhaust air leaving a building, while simultaneously bringing an equal amount of fresh air. The primary difference between HRV and ERV devices is that a flat-plate HRV transfers only sensible heat, based on an air temperature change, on the order of 50%-80% depending on flow orientation and volume (Idayu and Riffat 2012). In contrast, an ERV recovers both sensible and latent heat dependent on air temperature and humidity changes, which result in a higher overall effectiveness for an ERV compared to the HRV.

Recent advances in ERV membrane and mechanical control technology have enabled their expansion into additional climate zones that are beyond their original applications, which were typically colder regions, resulting in a wider temperature operating range (Garber-Slaght et al., 2014). In other words, they have become suitable for implementation across a larger portion of the world. Additionally, in cold, dry climates because moisture is transferred in an ERV, the IAQ is improved as less moisture is exhausted to the environment (due to the retention of the existing indoor air moisture), which coincidentally results in less moisture needing to be added to the entering outdoor air to maintain a comfortable indoor environment; however, recent studies have shown contaminants may also be transferred across the membrane. Due to the close positioning of the exhaust and intake for these devices, and to maintain indoor occupant health and comfort, the identification and mitigation of contaminant transfer from the exhaust-to-intake airstream at the interface of a building and the environment is of special importance.

Airflow Interaction

Heat and energy recovery ventilators (HERV's) are similar in their principle of operation and in their physical layout, with two major differences being the types of energy transfer through the surface located at the interface of the two airflow streams (i.e exhaust and intake), which also dictate the type of material separating the airstreams. For clarity the airstreams are defined in Figure 1 and the nomenclature presented will be maintained throughout this document.

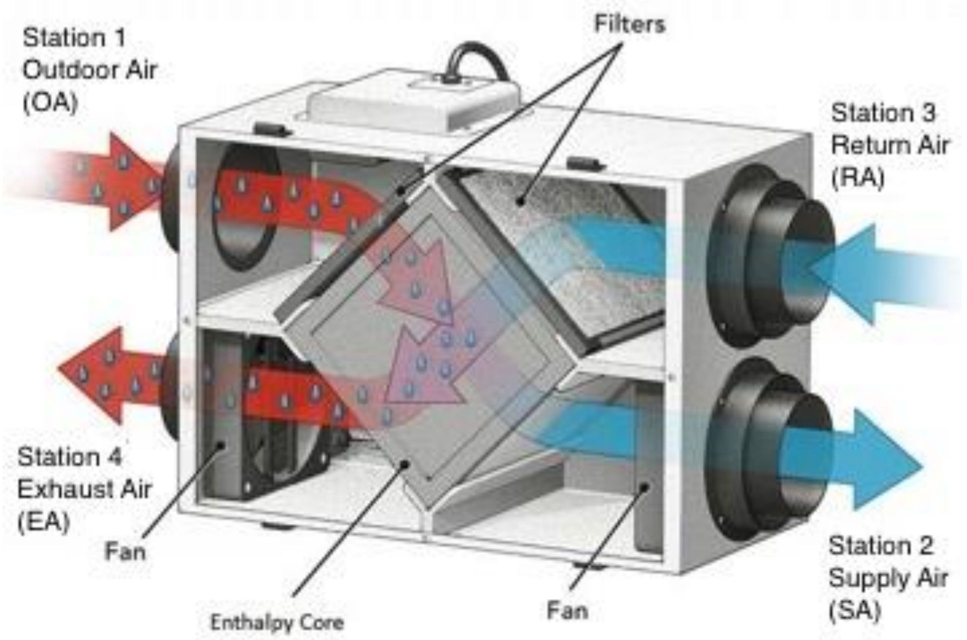

Figure 1: Airflow for HERV's - Adapted (EP Sales, 2017)

Energy contained in the Return Air (RA), or Station 3, from inside the building is passed through the enthalpy core and transferred to the Outdoor Air (OA), or Station 1. The air properties after energy transfer occurs in the core are obtained from the two outlets, which are the Exhaust Air (EA) outlet where stale air is exhausted to the outdoors, also known as Station 4, and the Supply Air (SA) outlet where fresh air is exhausted to the building, also known as Station 2.

A typical installation of these devices is near an exterior wall for shorter duct runs and as a by-product, these shorter duct runs result in small distances between the intake and exhaust, which can cause cross contamination as the intake is inadvertently pulling in air that is being exhausted. An example of a typical installation is shown in Figure 2 with screened vents while other vent caps may be used at the outdoor building interface.

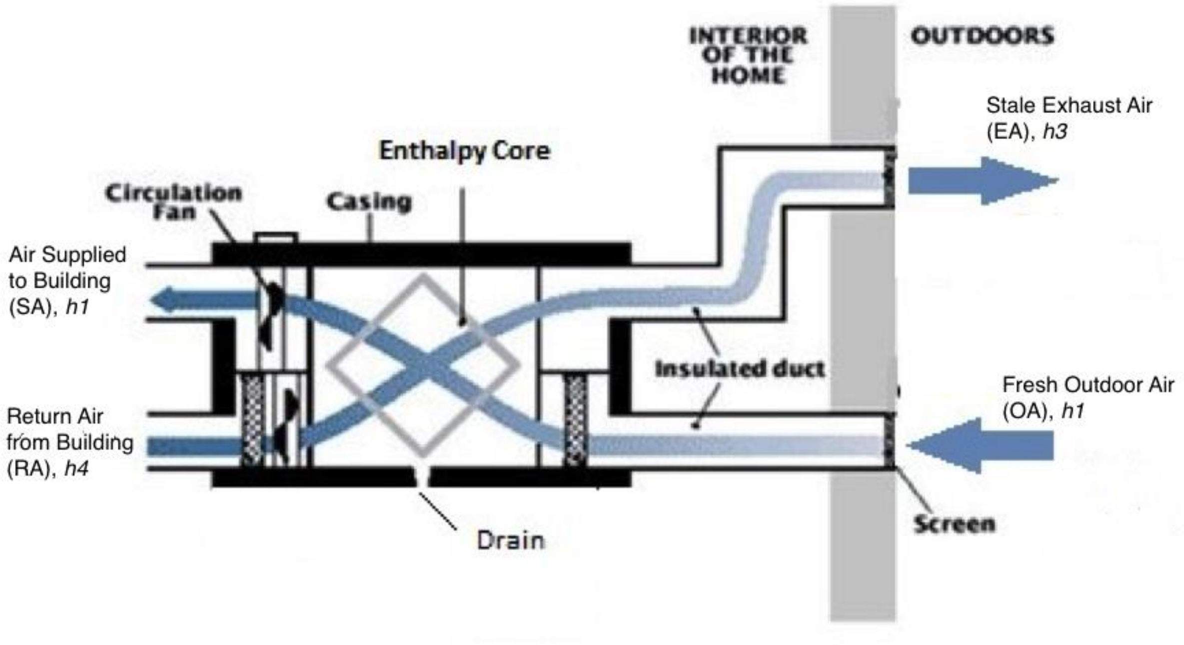

Figure 2: HERV Installation - Adapted (Mara Air, 2014)

The apparent effectiveness of an ERV can be determined by using temperature, humidity and flowrate data collected at the inlets and outlets, in conjunction with an equation that represents the ratio of the actual energy transferred to the maximum possible energy transfer with the result being shown below in Equation 1.

$$\varepsilon = \frac{\dot{m}_{OA}(h_1 - h_2)}{\dot{m}_{min}(h_1 - h_3)} \tag{1}$$

where,

ε = apparent effectiveness
$\dot{m}_{OA}$ = mass flow rate of the outdoor air (OA)
$\dot{m}_{min}$ = mass flow rate of the exhaust (EA) or supply (SA)
h = enthalpy at points 1-3 which correspond to OA, SA, and RA, respectively

It is important to note that Equation 1 does not take into consideration the Exhaust Air-Transfer Ratio (EATR), which occurs during actual ERV operating conditions and represents air leakage between the two airflow streams due to the construction or membrane material. The EATR, while not experimentally verified in this research, will invariably add to any mixing results obtained from the exhaust to intake crossover experiments presented in the later chapters. This addition is because a small amount of air will "leak" from the exhaust to the intake airstream inside the device due to manufacturing tolerances, poor seals, or membrane materials.

Classes of Air

As referenced from the ASHRAE 62.1 standard, there are four classes of air that are important for determining the impacts of the experimental and simulated results from this research. This impact is related to the maximum exhaust air that is allowed to be returned to a building, and are defined below based on class designations.

Class 1: Low contaminant concentration, inoffensive odor or sensory irritation

Class 2: Moderate contaminant concentration, mildly offensive odor or sensory irritation

Class 3: High contaminant concentration or sensory irritation

Class 4: Excessive contaminant concentration, considered harmful or containing dangerous particles.

The only class of air that may be recirculated in any space is Class 1 air. Class 2 air is unsuitable for recirculation within spaces containing Class 1 air, or non-similar spaces containing Class 2 or 3 air, for example recirculating air from a cafeteria to a gymnasium. Class 3 and 4 air should not be recirculated to any other space.

Class 2 and Class 3 air may be re-designated to Class 1 if the air is diluted enough with outdoor air. The final airstream may be re-designated as Class 1 if it contains maximums of 10% and 5% of the initial Class 2 or Class 3 air, respectively (AirXchange Inc.). Ideal placement of the exhaust and intake for HVAC equipment will result in close to 100% outdoor air being pulled into the intake; however, in these scenarios there are strict guidelines that govern the maximum exhaust air that can be returned into the building. These classes of air can be used to determine if the percentage of exhaust-to-intake air transfer exceeds the maximum amounts for a specific application. For instance, while some geometries may permit recirculation of air from a cafeteria (10% crossover or less), they may not be suitable for recirculation of air from restrooms (5% crossover or less). This is important for designers to keep in mind as the results of this research are presented in later chapters.

Market Analysis

A concise study on the market impact of Energy Recovery Ventilators has been conducted in the past, and it reveals significant growth in the sector. Specifically, North America revenues accounted for $324.6 Million USD in 2006 with projected revenues doubling to $778.7 Million USD in 2012 according to Frost & Sullivan. In August of 2015, Navigant Research released a report revealing 2014 worldwide revenues of $1.6 billion USD with projected worldwide revenues of $2.8 billion in 2020 with a Compound Annual Growth Rate (CAGR) of 8.8%. More recently, Markets and Markets reported in July of 2016 that the 2021 projected worldwide revenues would grow from $1.76 billion USD in 2016 to $3.39 billion USD in 2022 with a CAGR of 11.4%. Additionally, a report published in July 2018 forecast the ERV market to have a CAGR of 11.9% from $2.15 billion USD in 2017 to $4.22 billion USD worldwide in 2023 (Global Info Research).

There are three major takeaways from these economic reports. Firstly, the market has continued to grow at slightly higher than expected rates, and it is logical to expect the energy recovery market to exceed $5 billion USD in the near future. Secondly, from 2015 to 2018 the projected CAGR has increased from 8.8% to 11.9%, a 52% increase, revealing strong confidence in the market. Finally, a driving factor behind the growth in the HRV and ERV sector partly corresponds to regulations requiring mandatory installation of energy recovery devices in new building construction in various countries. The importance of this research as it relates to future growth is that as ERV's become more commonplace, then the understanding acquired of how intake and exhaust spacing or geometry affects contaminant crossover in low-flowrate applications will be incorporated into future ERV designs resulting in increased efficiencies and higher indoor air qualities for future installations worldwide.

State of the Art

In support of this research, an extensive literature search was performed on relevant topics, such as exhaust and intake airflow mixing, contaminant transfer as a result of the mixing, and applicable research on Energy Recovery Ventilators. The published research to date has primarily focused on operating performance characteristics of ERV's for various indoor flow rates and mixing elements and or ERV design focusing on flow orientations and membrane material as it relates to internal contaminant transport.

One of the few relatable studies conducted to date on thermal mixing was not for an ERV, but rather for the outdoor and return airflows inside a standard package air handling unit, and it was solely experimental based. Eight flow configurations were experimented on using parallel blade dampers for airflow rates of up to 13,600 and 4,800 cfm for return air and outdoor air, respectively. It was concluded that the flow momentums of the streams and the damper orientation played a significant role in the mixing of the airstreams, with higher values of mixing coinciding primarily with higher airflow velocities (M. Mainkar et al.). The fact that this is the only reported study of air mixing for intake and exhaust ducting in close vicinity in a HVAC application demonstrated the need for further research performed herein.

Searches were conducted to procure literature on jet airflow mixing or contaminant transfer mixing in the built environment, with the result being few studies have been conducted thus far with the majority being research using Computational Fluid Dynamics (CFD) software. One particular relevant CFD study which involved modeling and simulating wall confluent jets for heating an indoor room, revealed the jet velocity profile was more sensitive to the air velocity than to the temperature difference (D. Tan et al). The ratio of vent-size (D) to room-size volume (L) was given as a dimensionless ratio D/L and values from 0.2 to 0.6 resulted in a reduced CO2 concentration with increased Air Changes per Hour (ACH), while values from 0.8 to 1.0 showed an increased CO2 concentration with ACH’s over 16 (S. Cao et al.). Studies into impinging ventilation jets versus standard mixing ventilation revealed a 37-47% reduction in the mean age of air due to the different mixing patterns (X Ye et al.).

Additional CFD studies on multiple in-line non-directional jets with high supply momentum and the effect on thermal stratification in a building have also been examined (F. Espinosa). Wall jets versus ceiling diffusers were studied at various flow-rates for an indoor office scenario and it was determined that the ceiling diffuser generated better mixing throughout the control volume (E. Lee et al.) however; this did not take into account contaminant transfer.

Steady state experiments were conducted to determine distribution of indoor contaminant concentrations as functions of inlet and exhaust locations for isothermal air. It was determined that the relative density of the contaminant effected the contaminant distribution at low flow rates while having a negligible effect at high flow rates. Near-source concentrations, these being contaminant concentrations near the intake, were significantly less for jet inlets than diffuser inlets (J Kahn et al.).

On the topic of airflow mixing for CFD studies there have been several to date that focus on forced ventilation airflow mixing. An investigation into Reynolds Averaged Navier-Stokes (RANS) for forced internal ventilation showed the standard k-ε method matched most closely with physical measurements (T Hooff et al.). In terms of contaminant mixing, a high wall jet inlet simulation was performed at 9 exhaust locations and 8 source locations. A uniform turbulent diffusivity model revealed differences between the model concentration estimates and the CFD results of 126% and 236% depending on the location of the measurement taken (C. E. Feigley et al); however; the study was conducted in 2006 and modeling software has progressed significantly since that time.

Flow path orientations such as counter, quasi, cross, and concurrent flow have been evaluated with CFD models in an effort to identify the highest to lowest sensible and latent effectiveness, as functions of flowrate. For example, a 40% reduction in total efficiency resulted when the volumetric flow rate was increased by a factor of 5 from 22.9 to 114.5 cfm (Zhang). Furthermore, research into balanced and unbalanced flows in a cross-flow ERV found that in order to obtain a high efficiency, the Reynolds number must be decreased for balanced flow (as applicable to this research), which occurs when both supply inlets have equal airflow rates, and increased for unbalanced flow, which occurs when supply inlets have different flowrates (Sebai, Chouikh & Guizani).

Few articles have been published regarding contaminant transfer in a membrane based ERV, which is an application this research can be applied to. One study showed that formaldehyde crossover ranged from 0.3% to 9.6% depending on the membrane material (R. Huizing et al.) and 6.8% to 12% for the entire exchanger including leakage effects (Fisk et al.). In another study, a wide variety of membranes were tested for volatile organic compound (VOC) and moisture transfer selectivity. The PVA/LiCl membranes revealed the best water vapor permeability to VOC transfer (L.Z Zhang et al.) while fouling studies determined coarse dust loading had minimal impact on sensible and latent effectiveness. Ultrafine aerosols (~0.1um) resulted in a <5% reduction in vapor permanence; however, under wet conditions, vapor flux reductions of up to 15% were documented (A. Engarnevis et al.). This is an important series of studies as it shows that there is additional contaminant transfer that occurs when using an ERV as opposed to strictly mixing from the exhaust airstream at a building interface. In other words, small amounts of contaminant transfer will take place inside a residential ERV which will add to the results encountered in this research.

To date there have been no studies have been identified that conducted experimental, numerical or simulation based research on external contaminant transfer due to exhaust and supply airflow mixing at a building interface, nor has research been conducted of the impact of this mixing on the apparent effectiveness for ERV’s.

Original Contributions to the Technology

The investigation and analysis of mixing air at the indoor-outdoor interface as reported herein, is an original contribution to the existing body of knowledge in two distinct ways. Firstly, by researching and determining the optimal geometry and orientation of the airflow intake and exhaust that reduces the mixing phenomena, the IAQ of the building can be increased. Specifically, by returning exhausted air back into the building, high levels of CO_2, or potentially worse contaminants are brought back into the occupied building, which can result in detrimental health effects to the occupants. Additionally, insight into mixing of the exhaust-intake interface is gained by comparing the effects of different outdoor environmental conditions with CFD simulations.

For example, the effect of thermal buoyancy due to higher exhaust air temperatures can be visualized and quantified. Secondly, while the impact of exhaust air transfer and contaminant transfer across a membrane inside an ERV has been studied, the impact on the apparent effectiveness of an ERV exhaust to intake mixing at the interface of a building has not been quantified. Even though the effectiveness of an ERV is beyond the scope herein, a first step is to quantify the mixing for various parameters which is the objective of this study.

Additional major contributions of this study are that a novel, well-instrumented test facility was designed and constructed, along with a detailed method of test procedure, to support the mixing experiments performed herein. This same facility with minor modifications, was designed to be used to support future ERV performance tests with respect to the CAN/CSA C439 method of test.

CHAPTER III

EXPERIMENTAL TEST FACILITY DESIGN

A major component of this research study was the design, development, and construction of a well-instrumented facility that simulates the intake-exhaust interface of a typical residential HVAC in the real world. This facility goes well beyond a real-world setup in that a multitude of instruments are installed along with equipment and controls to set and vary test conditions. Preparations were also made for follow-up ERV studies by installing additional equipment and instruments. A concise description of the hardware that was not utilized for this research, but selected and incorporated for future performance evaluations based on the CAN/CSA C439 *Laboratory methods of test for rating the performance of heat/energy-recovery ventilators* is presented in Appendix B

Design Considerations and Constraints

The test facility was designed for a specific set of environmental air conditions, namely volumetric flow rates of up to 250 cfm in a 6-inch diameter (D) duct and carbon dioxide insertion rates, which are a key parameter for determining mixing, to maintain concentrations up to 2,000 ppm at the maximum flow rate of 250 cfm. Additionally, this facility will be able to experimentally validate the results from the airflow mixing computational fluid dynamics (CFD) simulations. Instrumentation was selected in accordance with associated standards, namely C2301-11, ANSI/AMCA 210-16, ASHRAE 51-16, and ASHRAE 41-1 2013. A schematic of the facility per CAN/CSA C439, which was utilized as the primary design reference, is shown in Figure 3 and a schematic of the modified experimental facility is shown in Figure 4.

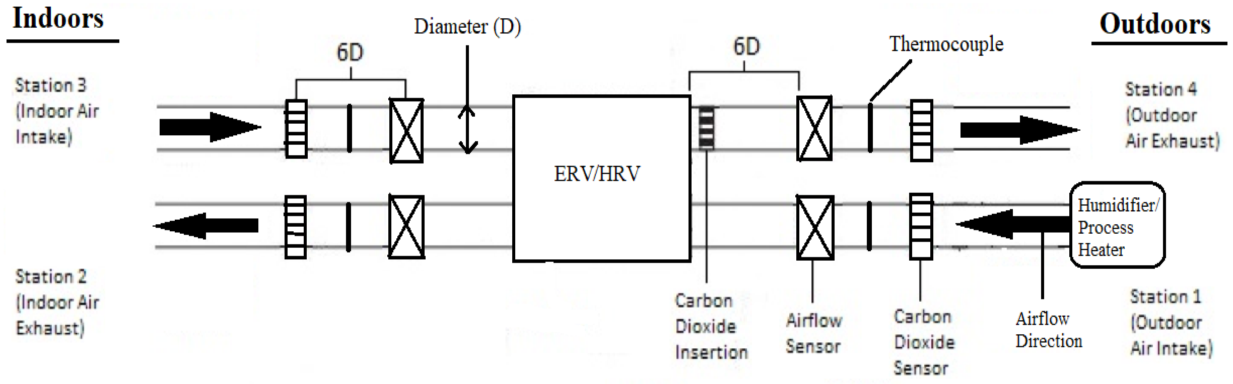

Figure 3: Schematic of Experimental Facility

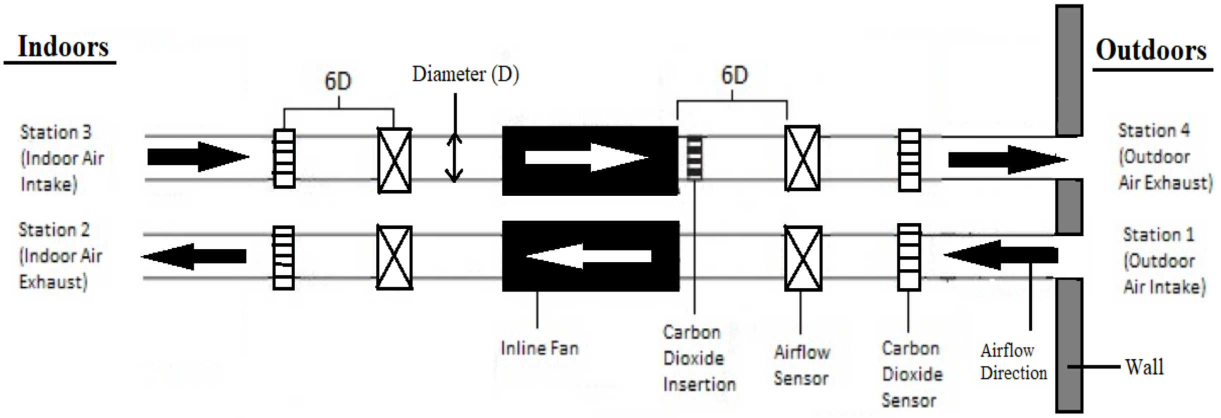

Figure 4: Schematic of Facility for Mixing Experiments

Stations 1-4 in Figure 3, as mentioned previously, correspond to the outdoor air intake (OA), supply air outlet (SA), return air inlet (RA), and return air exhaust (EA), respectively. A process heater/humidifier is installed at Station 1, with sensors for temperature, CO2/RH, and airflow velocity installed in the ducting of all 4 stations. Figure 4 simplifies this and represents the setup used for experiments in this research by substituting two inline fans to act as air-movers in lieu of an ERV, with only two sensors for measurements, namely the air velocity and CO_2

sensors. In addition, the process heater/humidifier and the thermocouples are removed as they are not necessary for this research.

The reasoning behind using inline fans to generate the airflow is they produce two independent, sealed airstreams as can be seen in Figure 4. Because of this, the measurements recorded only reflect mixing at the building interface as any possible effects between the two airstreams can be neglected, such as contaminant transfer across a membrane if an ERV was used.

Sensor Selection

A wide range of sensors were necessary to collect the requisite data to quantify the airflow mixing. In particular, hot wire anemometers were used for air velocity measurements and combination CO_2/RH sensors for determining CO_2 concentrations in the ducts. Thermocouples were installed; however, they were not used for any calculations in this research and are solely used to monitor laboratory air temperatures throughout a given test. Other pieces of equipment employed for the physical mixing experiments include the National Instruments data acquisition chassis, associated modules, and LabVIEW programming software.

Air Velocity Measurements

The air velocity measurements at all four stations were collected by using the E+E Elektronik™ EE650 Air Flow Sensor for HVAC with a selected measurement range of 0-10 m/s (0-2,000 ft/min) with a corresponding accuracy of +/- 0.2 m/s +3% of measured value. The required length of the calming section after a disturbance (otherwise known as the straightening section) for the EE650 is given as 6D (i.e, six diameters), or 36 inches for the 6-inch diameter ductwork used in this research. The Reynolds Number for flow in a pipe is given as Equation 5.

$$Re = \frac{\rho u D_H}{\mu} \tag{5}$$

where,

ρ = Density, (kg/m3)

u = Mean velocity of the fluid, (m/s)

D_H = Hydraulic diameter, (m)

μ = Dynamic Viscosity, (Pa·s)

The Reynolds numbers corresponding to the four tested flow velocities of 2.59, 3.88, 5.17, and 6.47 m/s, or volumetric flow rates of 100, 150, 200, and 250 cfm, respectively, are listed in Table 1.

Table 1: Effect of Temperature on Reynolds Numbers at Flow Rates of Interest

Temp (°F)	Density (lb/ft^3)	Dynamic Viscosity (lb/ft-s)	Reynolds Number			
			100 cfm	150 cfm	200 cfm	250 cfm
75	0.07301	1.23E-05	25,184	37,777	50,369	62,959
105	0.06883	1.28E-05	22,769	34,139	45,519	56,897

Reynolds numbers below 2,000 correspond to laminar flow, between 2,000 and 4,000 are deemed transitional flows, and above 4,000 the flow is expected to be turbulent. As all calculated Reynolds Numbers for this research are well above 4,000, the flow characteristic for all scenarios is turbulent.

The velocity profile of a turbulent fluid flow in a pipe differs from laminar flow, that is to say, the velocity distribution for a turbulent flow is more uniformly distributed when compared to laminar flows. This phenomenon is detailed visually in Figure 5 where "a", or the left diagram, and "b", or the right diagram, correspond to laminar and turbulent velocity profiles, respectively (E.M Khabakhpasheva).

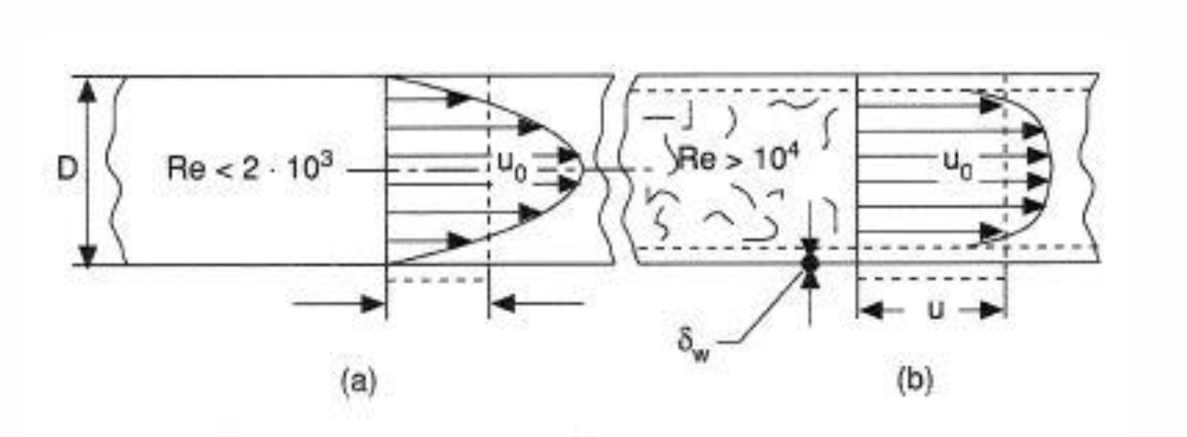

Figure 5: Velocity Profiles in a Duct

To verify the velocity throughout the duct was more-or-less uniform at a given cross-sectional area, a calibrated TSI Velocicalc 9565 was used to traverse the duct per ASHRAE Standard 111-2008 (RA 2017) using the log-Tchebycheff method. Because the duct is less than 10 inches in diameter, 6 measuring points per diameter, or 3 concentric circles were utilized.

Figure 6 highlights the method and specific distances as a function of the diameter of the duct (ASHRAE).

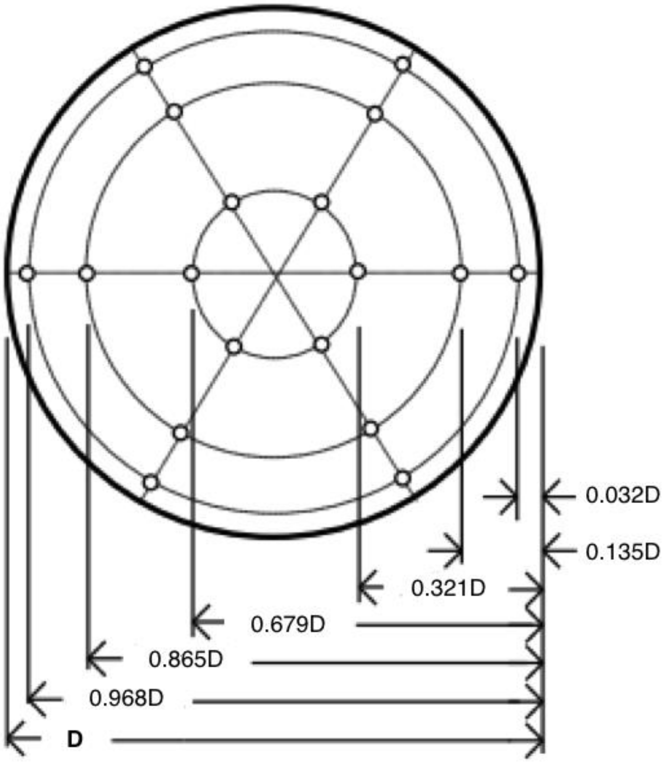

Figure 6: Log-Tchebycheff Duct Traverse Method

One reading per second for 20 seconds at each measurement point was taken, resulting in a total of 360 measurements. The accuracy for the TSI 9565 is +/-3% of measured value or 0.015 m/s, whichever is greater. Due to the flow rates measured it was determined that an insertion depth of 4”, or approximately 0.68 times the diameter resulted in stable air velocity measurements.

Carbon Dioxide Measurements

Carbon dioxide measurements were obtained for the experimental setup using the Dwyer CDTR (Carbon Dioxide, Temperature & Relative Humidity) class of sensors, with specific models used being three of the CDTR-2D4D4 and one of the CDTR-5D404. The 2D4D4 has a CO_2 measurement range of 0-2,000ppm, while the 5D404 has a measurement range of 0-5,000ppm. It should be noted that the relative humidity sensors on all models are equivalent with the only difference being the carbon dioxide sensor range.

The three 2D4D4's are installed at Stations 1, 2, and 3, corresponding to outdoor air (OA), supply air (SA), and return air (RA), respectively. The single 5D404 is installed at Station 4, corresponding to the exhaust air, as this duct contains the highest concentration of CO_2 due it to being the Station where the CO_2 is inserted. The working temperature range for the carbon dioxide sensors is listed as 32°F to 122°F (0°C to 50°C) while the accuracy is specified as +/-40 ppm +/-3% of the reading (Dwyer).

Relative Humidity Measurements

The sensor used for carbon dioxide measurements is a dual function sensor, which also allows simultaneous relative humidity measurements. Humidity limits are listed as 10 to 95% relative humidity, non-condensing, while the sensor accuracy is +/- 2% from 10 to 90% relative humidity. These measurements are valid for air velocities from 0-4,000 fpm (20.3 m/s). The relative humidity and temperature, obtained via thermocouples, of the laboratory air was monitored to ensure that thermal air properties were more-or-less similar prior to beginning testing.

Data Acquisition System

The backbone of the physical data acquisition system used in this research is the National Instruments (NI) CompactDAQ (cDAQ) 9174 which is a four-slot I/O module USB chassis capable of a timing resolution of 12.5*n*s and a timing accuracy of 50 ppm of the sample rate. Two I/O modules were used with the cDAQ-9174 for the airflow mixing experiments, namely the NI 9263and the 9205, with a third installed for thermocouple data acquisition, namely the NI 9213. The specifics of the 9213 module are presented in Appendix B as temperatures were not collected for data analysis for the mixing experiments and were solely used to monitor environmental conditions.

National Instruments 9205 Module

The carbon dioxide, relative humidity, and air velocity sensors described previously are all configured to output 0-10V DC. As a result, the NI 9205 I/O module was selected for the data acquisition of these sensors. The 9205 offers 16 differential or 32 single-ended +/-10 V inputs at a sample rate of up to 250 kS/s. Absolute accuracy for the 9205 is a combination of several factors as shown in Equation 6.

$$Absolute\ Acc. = Reading \cdot Gain\ Error + \ Offset\ Error\ + Noise\ Unertainty \qquad (6)$$

where,

<u>*Gain Error*</u> = Residual Gain Error + Gain Tempco · Temp Change from Last Internal Cal + Reference Tempco · Temp Change from Last External Cal

<u>Offset Error</u> = Residual Offset Error + Offset Tempco · Temp Change from Last Internal Cal + INL

<u>Error Noise Uncertainty</u> = (3 · Random Noise) / √100 for a coverage factor of 3 σ and averaging 100 points

Because 0-10V DC is considered full range for the 9205, the residual gain error is 115ppm, the gain temperature coefficient, or tempco, is 11 ppm/°C, residual offset error is 20ppm, offset tempco is 44ppm of range/°C, and the Integral Non-Linearity (INL) error is 76ppm. This results in a full-range absolute accuracy of 0.00623V, or 0.0623% at an input reading of 10V, which for the 0-2000ppm CO_2 sensors is a maximum of 1.25ppm. Because this is more-or-less negligible compared to the uncertainties in the sensors themselves, it is not added to the uncertainty calculations.

National Instruments 9263 Module

The final I/O module used in the cDaq-9174 is the NI-9263 analog output module. This module features a +/- 10V output signal with a sample rate of 100kS/s/channel. The sole purpose for this module is to act as a controller for the miniature proportional valve in order to regulate the flow of carbon dioxide into the exhaust duct in conjunction with the CO_2 regulator. The accuracy for this unit at 25°C, +/-5°C is 0.03%; however, because this module is solely used as a flow controller and not for data acquisition, it is not necessary to conduct any error or uncertainty analysis on this module or the connected component.

Equipment List

The major equipment used in conjunction with the experimental test facility in this research is summarized in Table 2. Equipment that directly applies to the physical airflow mixing tests is denoted in the following table by bold text, while an asterisk refers to items that were discussed in detail previously. Ductwork, insulation, and other miscellaneous items such as tape are not included in this equipment list.

Table 2: Experimental Facility Equipment List

Item	Description	Manufacturer	Model Number	Notes	Qty.
1	Humidifier	Aprilaire	801	10-95% RH	1
2*	**RH/CO_2 Sensor**	**Dwyer**	**CDTR-2D4D4**	**0-2,000ppm CO_2**	**4**
3	Duct Heater	Tempco	TDH01005	480V/6kW	1
4	Power Meter	Elekor	WattsOn-Mark II	-	1
5	Temperature Sensor	Omega	TT-T-24-SLE	SLE	4
6*	**I/O Chassis**	**National Instruments**	**cDAQ-9174**	**-**	**1**
7	Thermocouple I/O	National Instruments	NI 9213	-	1
8*	**Analog Input I/O**	**National Instruments**	**NI 9205**	**+/- 0-10V**	**1**
9*	**Analog Output I/O**	**National Instruments**	**NI 9263**	**+/- 0-10V**	**1**
10*	**Air Velocity Sensor**	**E+E Elektronik**	**EE650**	**0-20 m/s**	**4**
11	Temperature Controller	Watlow	SD4E-HCAF-AARG		1
12	**CO_2 Heater**	**ProFax**	**PXCO2**	**115V/60hz**	**1**
13	**CO_2 Regulator**	**Victor**	**ESS32-150-320**	**Single Stage**	**1**

Table 2: Experimental Facility Equipment List Continued

Item	Description	Manufacturer	Model Number	Notes	Qty.
14	Power Supply	Sola	SDP 4-24-110LT	98.8W, 3.8A Output	1
15	Power Controller	Watlow	DB20-60C0-0000	277-600VAC	1
16	Inline Ventilation Fans	Fantech	Prio Air 6 EC	445 CFM Max.	2
17	Control Valve	Kelly Pneumatics	KPI-VP-10-50-40-V	27 lpm CO_2	1

Inline Fan Airflow Verification

Two FanTech Prio Air 6 EC inline fans are used to generate the airflow required for the mixing experiments. They were selected due in part to the manufacturers stated ability to produce stable airflow volumes up to 425 cfm which covers the full airflow range for the scope of this research. In conjunction with the Prio Air 6 EC, the Zehnder DN 150 ventilation grill is used during the carbon dioxide mixing tests.

In order to verify that the two PrioAir 6 EC inline fans were capable of producing the required airflow, as well as the pressures produced at a given volumetric airflow rate, both units were tested via the Figure 12 setup from the ANSI/AMCA 210-2016 standard (ANSI). The two units were controlled via a 0-10V potentiometer and airflow performance tests were conducted at 5, 7.5, and 10V for both fans, designated Fan A and Fan B. Figure 7 gives a visual of the test setup for an inline fan, while Figure 8 shows the performance curves for both fans.

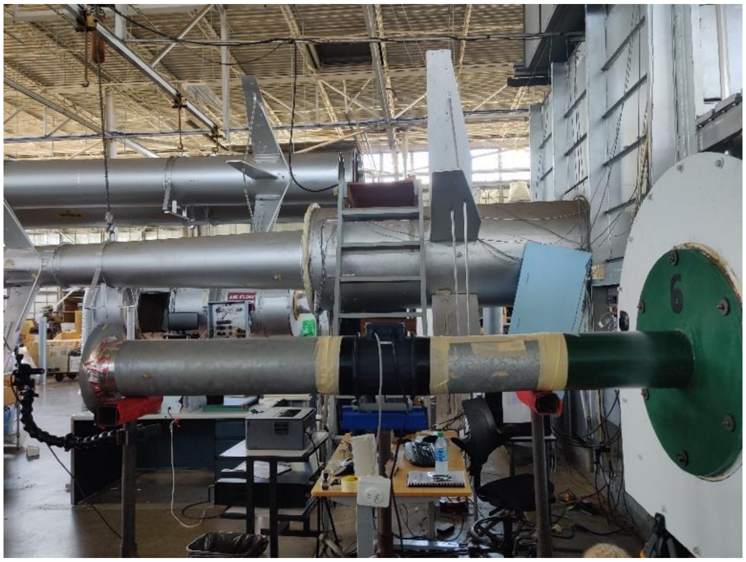

Figure 7: Inline Fan Performance Test Setup

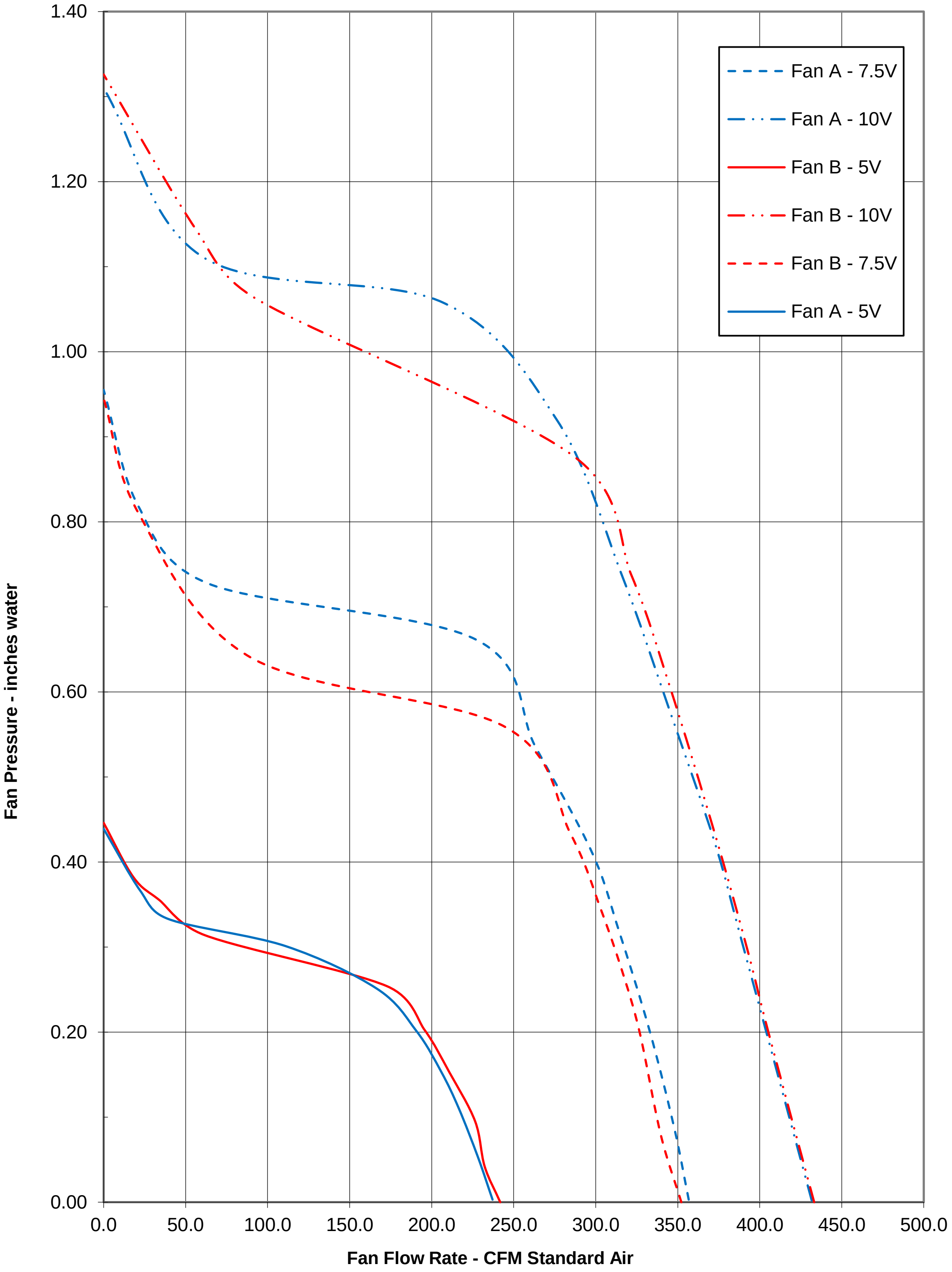

Figure 8: Inline Fan Performance Curves

Figure 8 highlights that the maximum output at any given input voltage from both inline fans is nearly identical, approximately 425 cfm with an input voltage of 10V. Additionally, it can be seen that at any input voltage, for a given flow rate the greatest difference in pressure between the two fans are 0.1” H_20 (inches of water). For example, 150 cfm at an input of 7.5V and approximately 200 cfm at an input of 10V. Flowrates of 100, 150, and 200 for the physical mixing experiments were obtained using approximately 7.5V of input, resulting in output pressures between 0.6 and 0.7 inches of water. The highest flow rate of 250 cfm required higher voltage inputs between 7.5 and 10V of input in order to overcome the pressure losses in the ductwork.

CHAPTER IV

EXPERIMENTAL INLET-OUTLET AIRFLOW MIXING INVESIGATIONS

The physical experiments to determine inlet-outlet crossover mixing are based off the facility design visualized in the previous chapter in Figure 5. Specifically, inline fans were used in conjunction with a 0-10V potentiometer to control the airflow rates in the independent inlet and exhaust ducts to remove any possibility of cross-contamination.

Experimental Setup

The experiments that form the base structure of the investigation consist of a total of three arrangements, namely vertical, inverse vertical, and horizontal, with three orientations per arrangement for a total of nine different physical setups. Each orientation is defined as a distance between the exhaust and intake, with these distances detailed in Table 3. In addition, four volumetric flow rates, varying from a low of 100 cfm to a high of 250 cfm, were tested at 8 of these 9 scenarios, as one scenario produced results below the accuracy limit of the CO_2 sensor employed. Approximately 10 tests per combination were conducted, with CO_2 concentrations between 1,000 to 2,000ppm inserted into the exhaust duct for a given test. The reasoning behind this wide range of CO_2 concentrations is that it allows for a clearer representation of exhaust-intake crossover across a wide range of CO_2 ranges and gives confidence in the results.

In general, each test was performed for 15 minutes with a minimum 30-minute cool-down period between tests to allow the ambient CO_2 levels in the vicinity of the experimental facility to stabilize to normal atmospheric levels.

Table 3: Exhaust and Intake Spacing (Orientation)

	Orientation 1 (O1)	Orientation 2 (O2)	Orientation 3 (O3)
Center-to-Center Distance	12”	24”	48”

As can be seen in Table 3, each orientation doubles the distance of the previous orientation such that the third orientation (O3) is equivalent to four times the distance of the first orientation (O1). This is shown visually in Figure 9; however, it should be noted this image is not to scale.

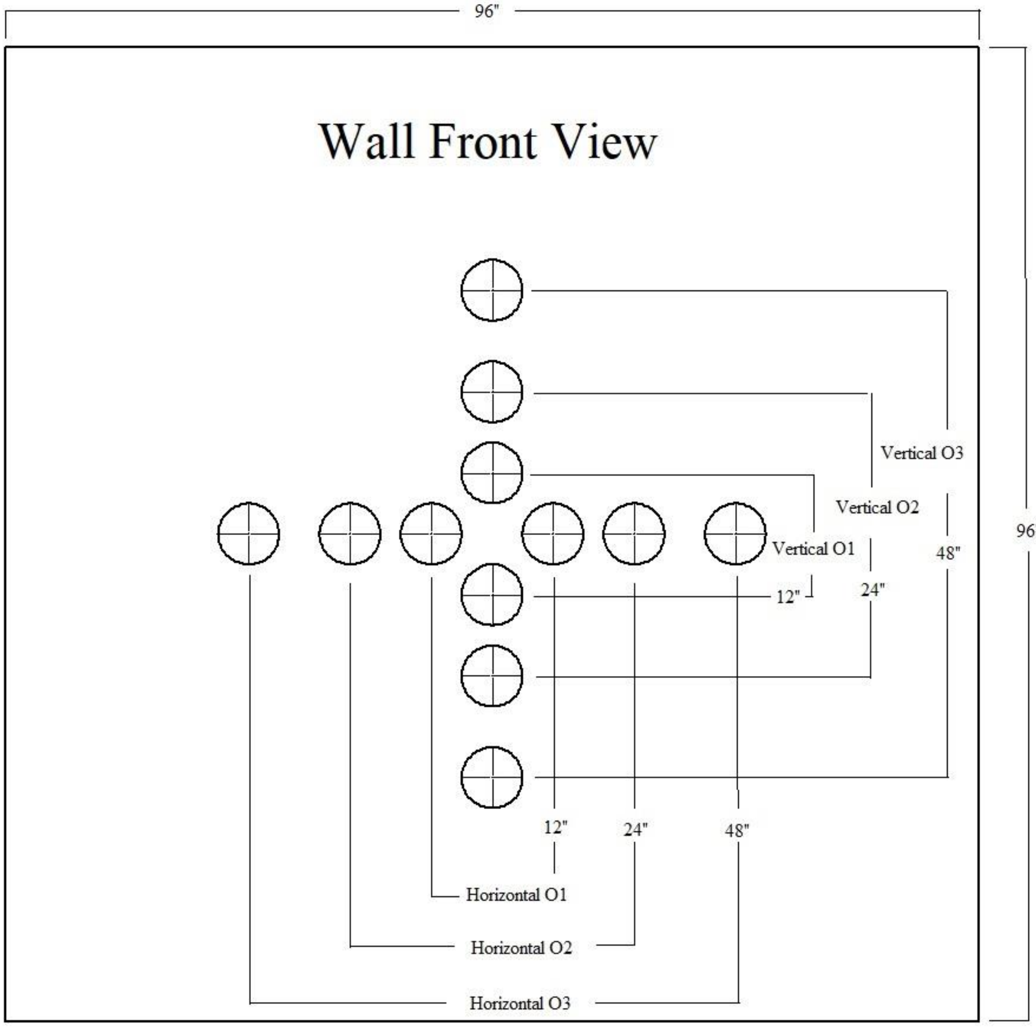

Figure 9: Experimental Wall Setup

The wall setup visualized above is used for all experiments in conjunction with the Zehnder ZN-150 ventilation grill, which is a common representation of grills used in residential installations and is shown visually in Figure 10. The wall is constructed of two 4’ x 8’ sheets of plywood to form an 8’ x 8’ surface. Six-inch holes are removed from the wall at the positions indicated in Figure 9 and the two grills are installed in the respective holes in the wall prior to each experiment and sealed with masking tape to ensure zero leakage.

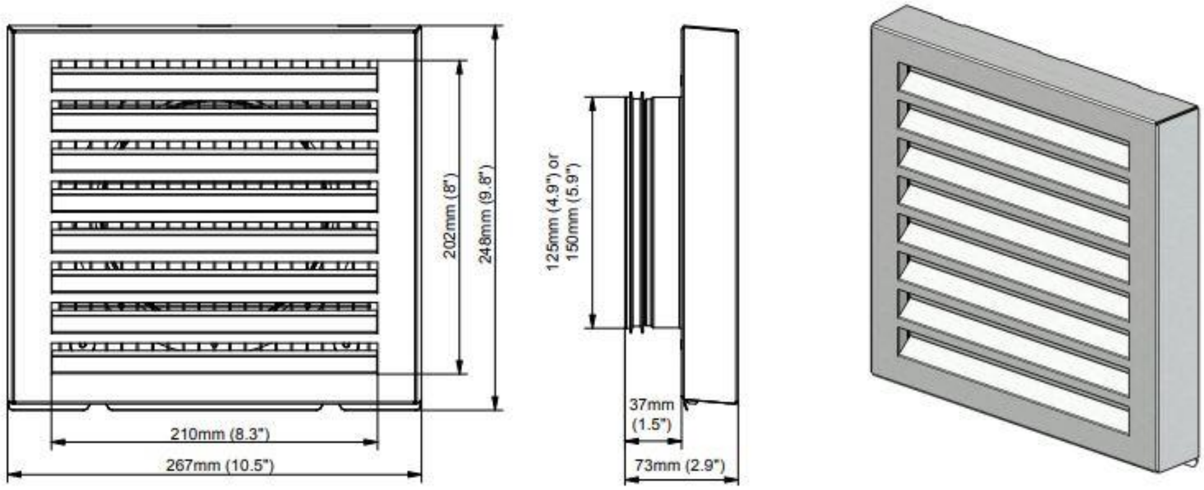

Figure 10: Diagram of Ventilation Grill (Zehnder)

As noted previously, all experimental setups have the ZN-150 grill installed with the directional vanes pointing downward as seen in Figure 10. The external dimensions of the grill are 10.5” wide by 9.8”tall, while the actual vent area is 8.3” wide by 8” tall and the grill extends 1.4” from the wall. In the case of the inverse vertical setup, the exhaust is positioned above the intake such that the exhaust air is directed downwards toward the intake.

Steady State

Steady state for each of the experiments was realized by ascertaining the time at which the measured value for the exhaust CO_2 sensor had more-or-less stabilized following the insertion of carbon dioxide in the airstream. It was determined that regardless of the air flow rate,

CO_2 injection rate, or orientation, steady state occurred after approximately 300 seconds, or 5 minutes. The parameters used to justify steady state for this research relate to the linear slope of the exhaust concentration obtained by Equation 6.

$$m = \frac{E_{300} - E_{Final}}{300 - t_{Final}} \tag{6}$$

where,

m = Slope of exhaust CO_2 concentration with respect to time

E_{300} = Exhaust CO_2 concentration at 300 seconds

E_{Final} = Exhaust CO_2 concentration at the final measurement

t_{Final} = Time at the final measurement

Exhaust concentrations with slopes (m) of approximately +/- 0.15 are considered steady state. This slope relates to an increase or decrease of 9 ppm of CO_2 per 1 minute of test time, which is equivalent to an increase or decrease of 90ppm for a 10-minute test after reaching steady state. This increase or decrease in CO_2 concentration is within the base sensor accuracy of +/- 40ppm plus +/- 3% of the reading. The working CO_2 range of 1,000 to 2,000 ppm correlates to a minimum of +/- 70ppm or a maximum of +/- 100ppm, respectively.

An additional verification of steady state is based on examining the percent change in the exhaust CO_2 concentration with respect to the previous reading as determined from Equation 7 below

$$d_r(\%) = \frac{E_{i+1} - E_i}{E_i} \tag{7}$$

where,

d_r = Relative difference between measurements (%)

E_i = Initial exhaust CO_2 concentration at any reading (ppm)

E_{i+1} = Successive CO_2 concentration reading (ppm)

Fluctuations in CO_2 for the exhaust airstream are to be expected; however, ideally the relative difference (d_r) should be no more than 0.5% between two readings back-to-back. This fluctuation percentage of 0.5% in the exhaust airstream is equivalent to minimum differences of 50ppm and a maximum difference of 100ppm as it relates to the exhaust CO_2 concentration limits of 1000 and 2000ppm, respectively. These differences of 50 and 100ppm are also within the accuracy limits of the sensor as outlined previously.

Figure 11 and Figure 12 show the exhaust and intake CO_2 concentration with respect to time for tests conducted at 150 and 250 cfm for different orientations and arrangements, while the steady state timeframe is highlighted by a black line beginning at 300 seconds with slopes of 0.14 and 0.11, respectively. These two figures represent tests for two different experimental setups and flow-rates, namely inverse vertical O3 150 cfm and horizontal O2 250 cfm with the test depicted in Figure 12 being twice as long as the test in Figure 11, 700 versus 1500 seconds, respectively. Even with these differences, the time to exhaust CO_2 concentration stabilization was nearly identical at 300 seconds. It is less apparent visually at first glance that the exhaust CO_2 stabilized at 300 seconds in Figure 12.

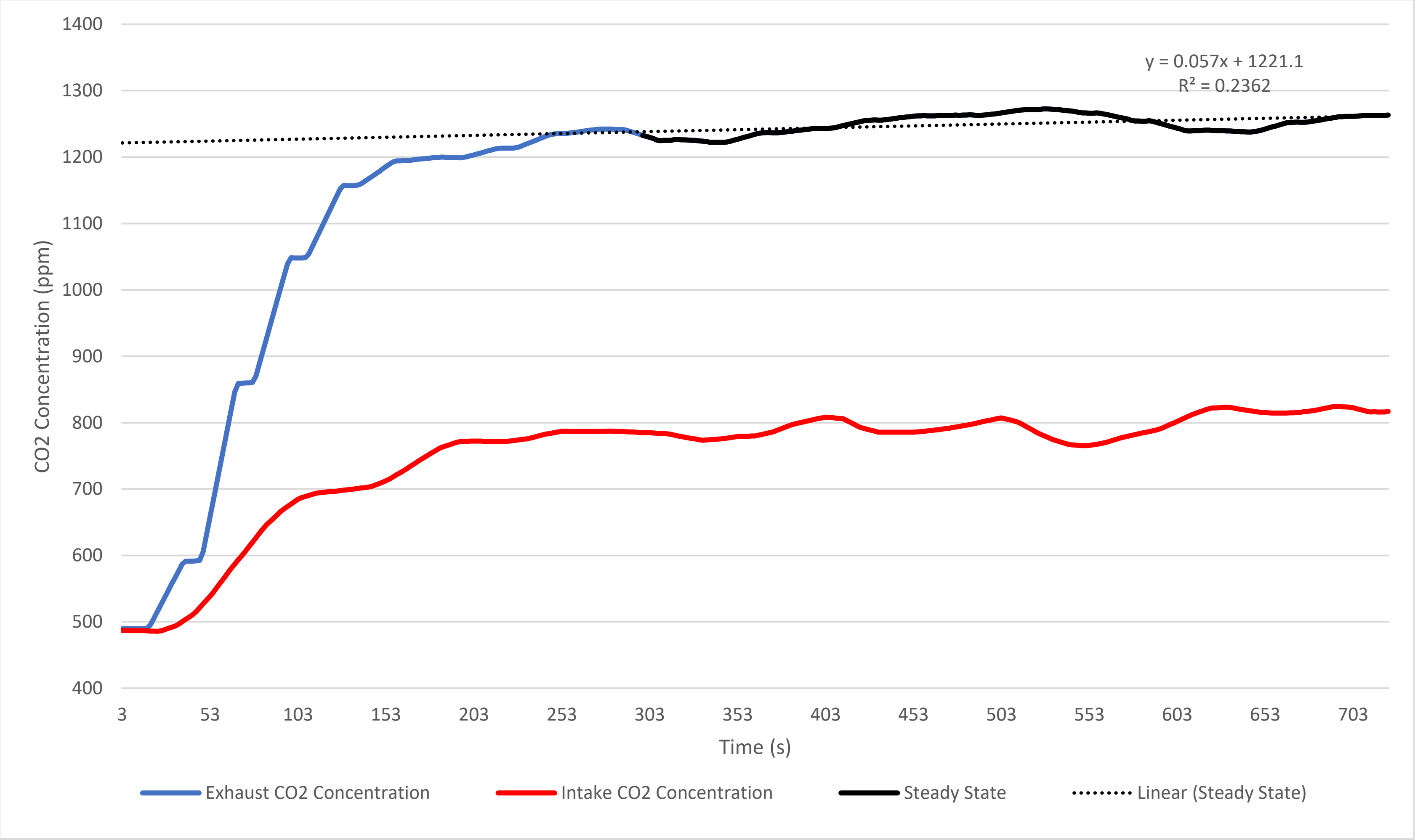

Figure 11: Inverse Vertical O3 150 CFM Exhaust/Intake CO_2 Concentrations vs. Time

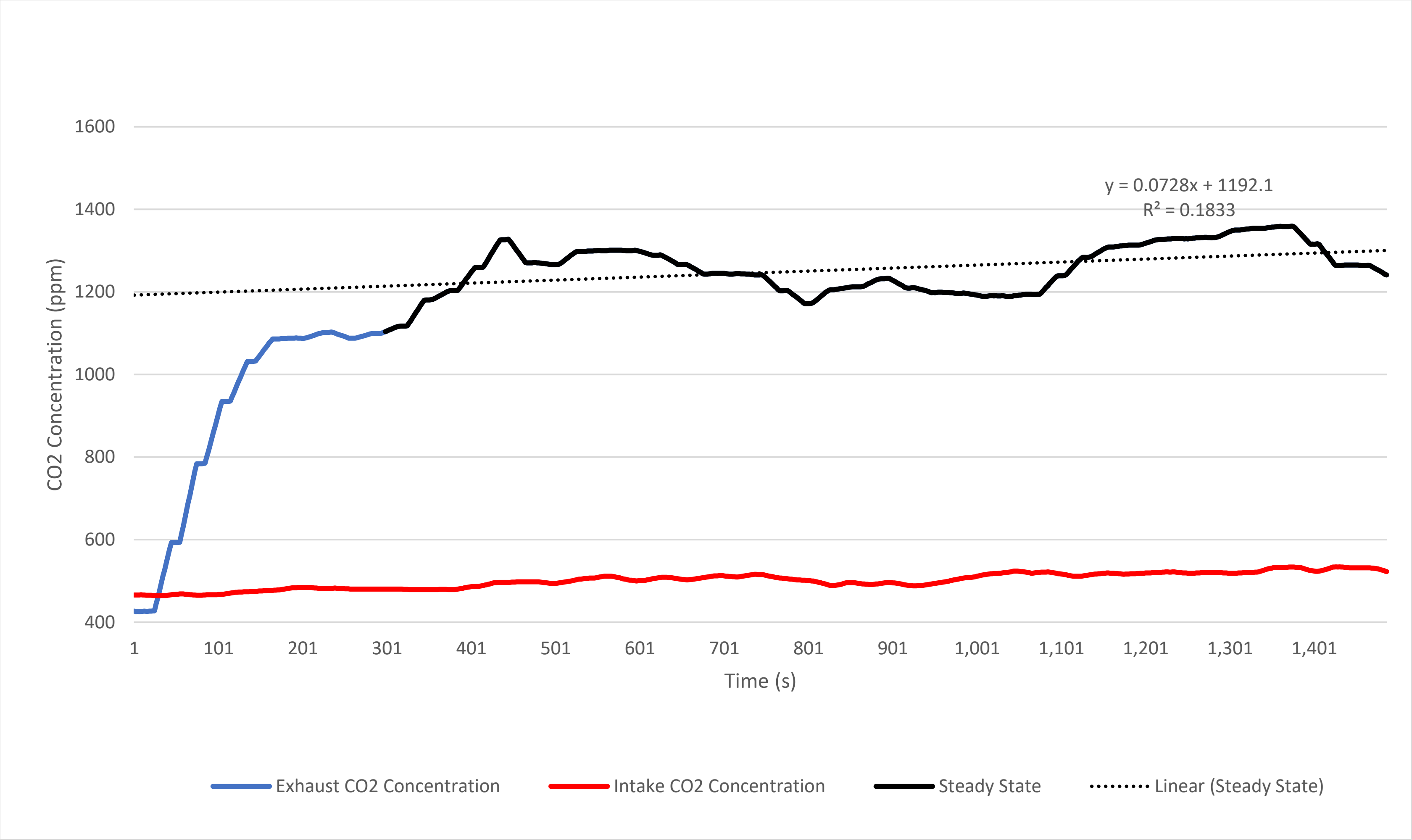

Figure 12: Horizontal O2 250 CFM Exhaust/Intake CO2 Concentrations vs. Time

Figure 13 and Figure 14 are introduced to show the percent change in exhaust and intake CO_2 with respect to the previous measurement for a test on a stacked bar graph. For both experiments, after 300 seconds the percent change with respect to the previous measurement as calculated was typically well below 0.5%. By maintaining a relative change of less than 0.5%, the difference between the CO_2 measurements during the steady state time for back-to-back measurements are less than the uncertainty values of the CO_2 sensors. That is to say, an increase or decrease of 50 or 100ppm between measurements for exhaust concentrations of 1,000 or 2,000ppm, respectively, are within the tolerances of the sensors for these concentrations, these being 70 and 100ppm, respectively. This supports the findings in Figure 11 and Figure 12 that the exhaust and intake CO_2 concentrations reached steady state after 5 minutes when viewed in Figure 13 and Figure 14.

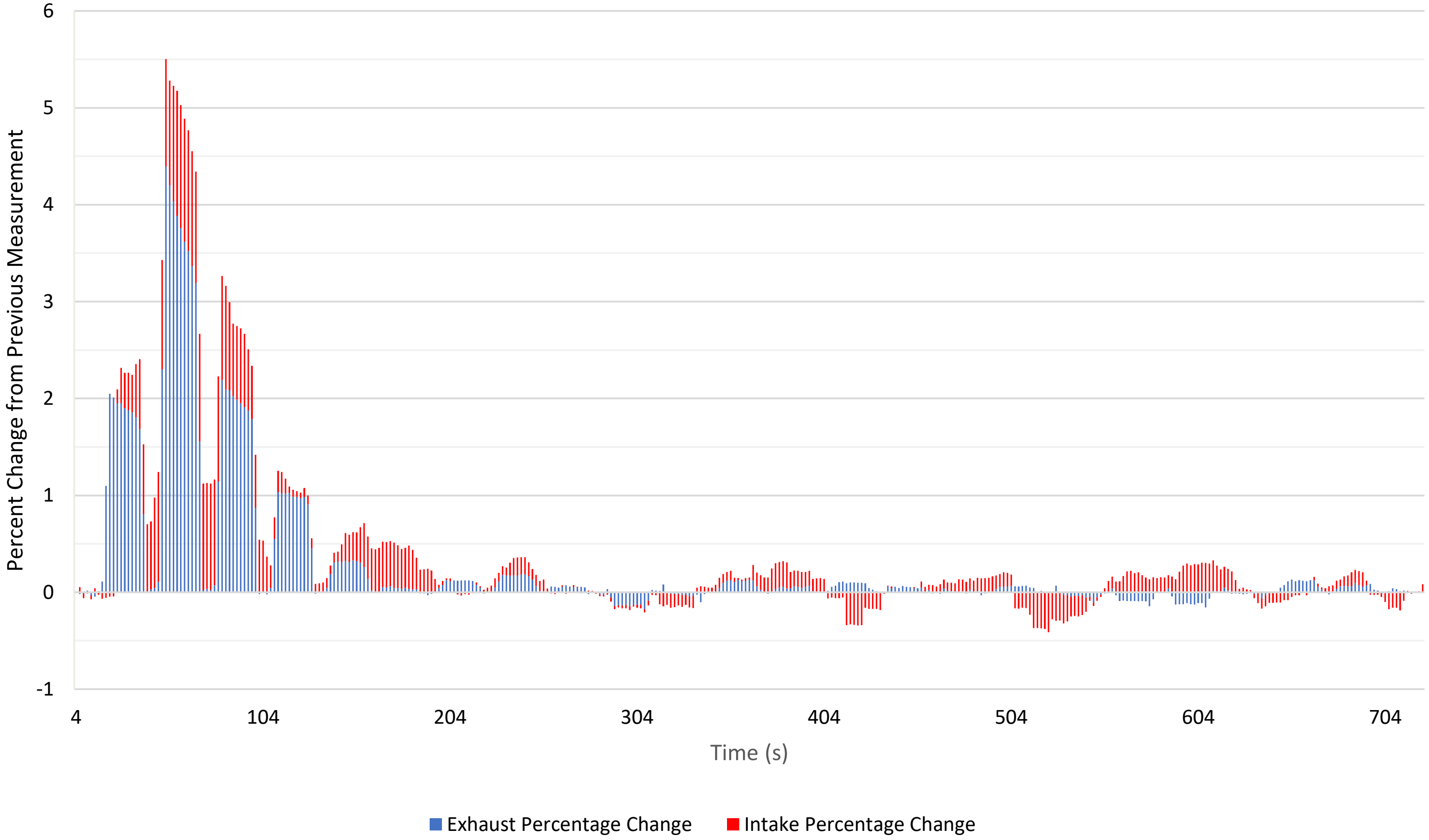

Figure 13: Inverse Vertical O3 150 CFM Percent Change from Previous Measurement

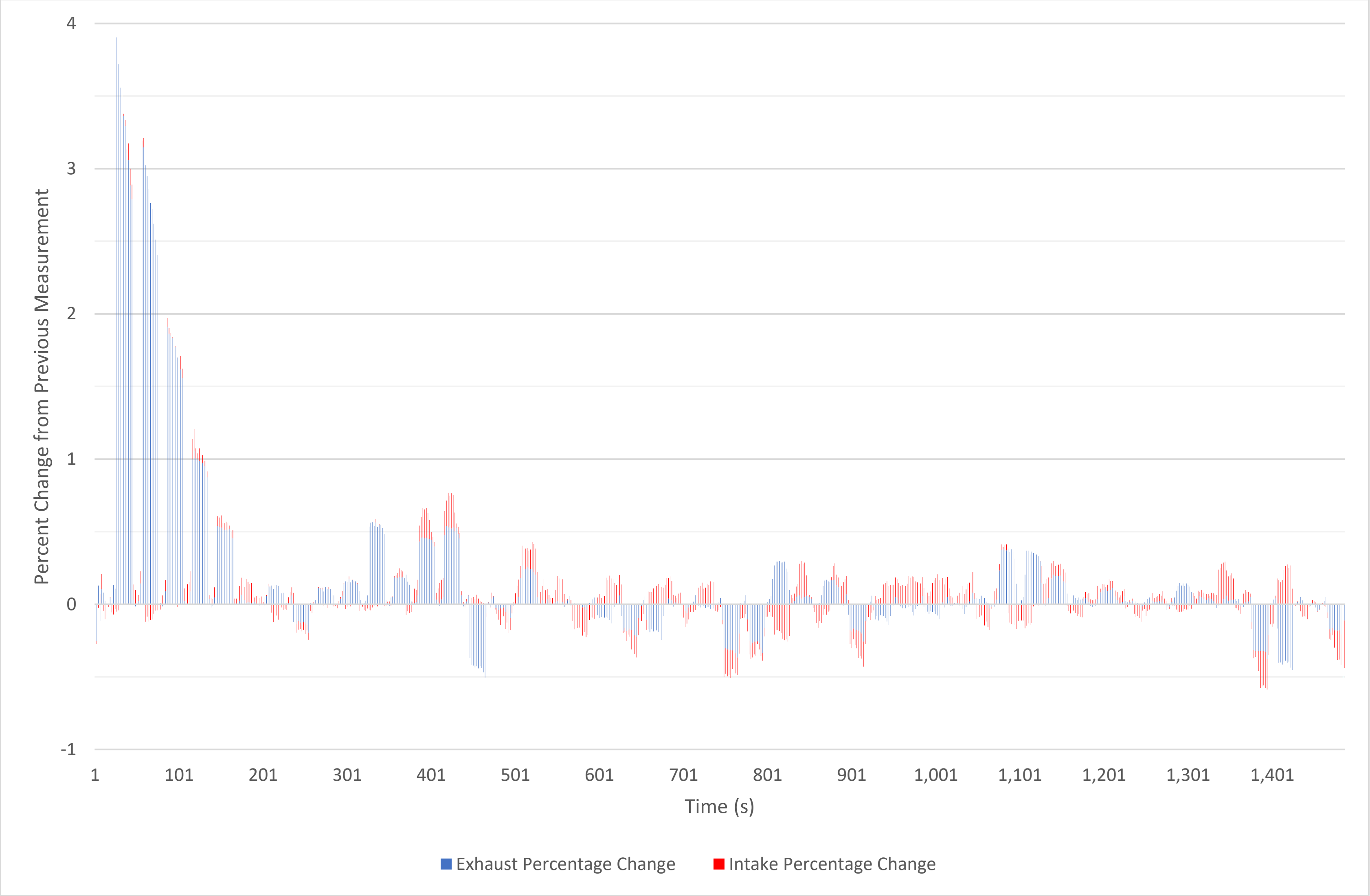

Figure 14: Horizontal O2 250 CFM Percent Change from Previous Measurement

Atmospheric Carbon Dioxide Correction

As part of the experimental data analysis, it is necessary to correct the exhaust and intake carbon dioxide values with respect to the atmospheric carbon dioxide present during a test. This correction is done for two reasons, firstly at lower exhaust carbon dioxide concentrations the perceived crossover at the mixing point is dominated by the atmospheric CO_2 concentration, making the CO_2 concentration appear significantly higher than it really is. As a result, this correction aids in stabilizing the results across specified exhaust concentration range of 1000 to 2000ppm.

Secondly, by performing this atmospheric CO_2 correction, experimental results presented herein are in-line with the results obtained from the CFD simulations making for a more accurate comparison. Due to fluctuations in atmospheric carbon dioxide levels after a test, a separate, remote CO_2 sensor was used to monitor the atmospheric CO_2 levels, which are the laboratory space levels, prior to or between tests in an effort to ensure stabilization of the ambient carbon dioxide levels. Again, as noted the atmospheric or ambient CO_2 levels are actually the lab space values, which is where the experimental facility is located.

The equations used to calculate the uncorrected crossover values (XO_{NA}) and the corrected crossover values (XO_A) are presented in Equation 8 and Equation 9, respectively. Furthermore, Equation 9 can be simplified and is presented in Equation 10.

$$XO_{NA}(\%) = \left(1 - \frac{E_{avg} - I_{avg}}{E_{avg}}\right) \cdot 100 \tag{8}$$

$$XO_{A}(\%) = \left(1 - \frac{\left(E_{avg} - 400\right) - \left(I_{avg} - 400\right)}{E_{avg} - 400}\right) \cdot 100 \tag{9}$$

$$XO_A(\%) = \left(\frac{I_{avg} - 400}{E_{avg} - 400}\right) \cdot 100 \qquad (10)$$

where,

E_{avg}, = Averaged CO_2 concentration values for the exhaust (ppm)

I_{avg} = Averaged CO_2 concentration values for the intake (ppm)

The constant of 400ppm shown in Equation 10 represents the atmospheric carbon dioxide concentration value. In an effort to clarify further, a sample calculation is provided for XO_{NA} and XO_A, with E_{avg} and I_{avg} equal to 1500 and 1000ppm, respectively.

$$XO_{NA} = \left(1 - \frac{1500ppm - 1000ppm}{1500ppm}\right) \cdot 100 = 66.6\%$$

$$XO_A = \left(\frac{1000ppm - 400ppm}{1500ppm - 400ppm}\right) \cdot 100 = 54.5\%$$

$$XO_A = \left(\frac{600ppm}{1100ppm}\right) \cdot 100 = 54.5\%$$

Because the atmospheric CO_2 concentration is not relevant in determining mixing, it is removed from the calculations and what remains is only the amount of carbon dioxide added to the ambient levels, or for this example 1100 and 600ppm for the exhaust and intake, respectively, calculated as follows with the prime symbol representing the corrected values.

$$E'_{avg} = E_{avg} - 400ppm = 1100ppm$$

$$I'_{avg} = I_{avg} - 400ppm = 600ppm$$

Uncertainty Analysis

The uncertainty analysis focuses on both measurements and calculations. For example, due to the nature of mechanical sensors, there are inherent uncertainties in the measured values, and in the case of the carbon dioxide sensors used in this study, these uncertainties have a base of +/- 40ppm with an additional +/-3% of the measured value. In terms of uncertainties associated with calculations, the Kline-McClintock method is used to determine uncertainties for the Equation 10 calculation. A typical calculation procedure for the Kline-McClintock uncertainty analysis calculation is performed using Equations 11 and 12 where w_A, w_B, w_C, and w_D are the errors in variables A, B, C, and D, respectively.

$$A = B \cdot C \cdot D \tag{11}$$

$$w_A = \sqrt{\left(\frac{\partial A}{\partial B}\right)^2 (w_B)^2 + \left(\frac{\partial A}{\partial C}\right)^2 (w_C)^2 + \left(\frac{\partial A}{\partial D}\right)^2 (w_D)^2} \tag{12}$$

Continuing the example presented earlier, Equation 11 can be related to Equation 13 where XO_A, I_{avg}, and E_{avg}, are substituted with A, B, and C, respectively. Taking the derivatives of A with respect to the variables B and C result in the expressions shown in Equations 14 and 15, respectively.

$$A = \frac{B - 400}{C - 400} \tag{13}$$

$$\frac{\partial A}{\partial B} = \frac{1}{C - 400} \tag{14}$$

$$\frac{\partial A}{\partial C} = \frac{400 - B}{(C - 400)^2} \tag{15}$$

The next step is to replace the variables B and C in Equations 13 through 15 with actual values of 1000 +/- 70ppm and 1500 +/- 85ppm, respectively, resulting in an uncertainty of +/- 7.63% as follows.

$$w_A = \sqrt{\frac{1}{1500 - 400} \cdot 70^2 + \frac{400 - 1000}{(1500 - 400)^2} \cdot 85^2}$$

$$w_A = \pm 0.0763 = \pm 7.63\%$$

Thus, the results for the example presented earlier for XO_A becomes

$$XO_A = 54.5\% \pm 7.63\%$$

It is important to note that this uncertainty of +/- 7.63% is not a static number that can be applied to all tests; rather, it must be calculated for each individual test due to the variation in the measured carbon dioxide values. The uncertainty for the $XO_{NA,}$ (i.e., the uncorrected crossover value), in this example is slightly lower at +/- 6.0%. For both examples, the calculated uncertainty is most heavily influenced by the accuracy of the intake sensor because the intake sensor reads lower CO_2 values than the exhaust sensor. As a result of the accuracy of the sensor, there is greater uncertainty at lower CO_2 readings than higher CO_2 readings. It should be noted that the uncertainties are averaged for all tests at a given flow-rate and presented in the comparison bar graphs in Chapter V for clarity.

Standard Deviation and Standard Error

The standard deviation parameter is important to calculate as provides understanding of the spread of the calculated crossover (XO_A) for the range of exhaust carbon dioxide concentrations, especially since there are approximately 10 tests per orientation. Standard deviation is calculated based on Equation 16 (Bland & Altman).

$$\sigma = \sqrt{\frac{\Sigma(x_i - \mu)^2}{N}} \tag{16}$$

where

$\sigma = population\ standard\ deviation$

$N = size\ of\ the\ population$

$x_i = each\ value\ from\ the\ population$

$\mu = the\ population\ mean$

The value for the standard error of the mean (SEM) decreases with increasing sample size and shows the variability of the estimator. In other words, it quantifies how precisely the average of a given sample size is known, in this instance the sample size being the number of tests. The closer the SEM is to zero, the more accurate the calculated average is and because the SEM is near zero for the experimental results, the calculated averages for each of the four flowrates are presented with confidence. The standard error of the mean is calculated based on Equation 17 (Everitt, B.S).

$$\sigma_x = \frac{\sigma}{\sqrt{n}} \tag{17}$$

where,

$\sigma_x = the\ standard\ error\ of\ the\ mean\ (SEM)$

$n = the\ number\ of\ observations\ of\ the\ sample$

$\sigma = population\ standard\ deviation$

To recap, the benefit of the three statistical parameters introduced, namely the uncertainty, standard deviation, and standard error of the mean, is that they allow insight into the calculated crossover percentages beyond the raw numerical averages. The uncertainty reveals the total range of the averaged crossover values as a byproduct of the inaccuracies of the mechanical sensors. The standard deviation assists in determining how far apart the individual measurements are, with one standard deviation containing approximately 68% of all measurements, and 2 standard deviations containing approximately 95% of all measurements. The standard error of the mean is another method to assist in showing how close the measurements are together, with values closer to zero representing closer grouping of measurements. All three parameters will allow future follow-up studies to accurately determine how close their results align with this research.

CHAPTER V

INVERSE VERTICAL ARRANGEMENT EXPERIMENTS

An investigation into the CO_2 mixing for vertically oriented ventilation grills with an inverted (i.e., the exhaust is installed above the intake), intake and exhaust was conducted first. For this scenario, the exhaust vent is positioned above the intake vent and three center-to-center spacing's were tested, namely 12" separation, or Orientation 1 (O1), a 24" separation, or Orientation 2 (O2), and finally a 48" separation, or Orientation 3 (O3). Visuals of these setups are provided in Figure 15 through Figure 17, for O1, O2, and O3, respectively.

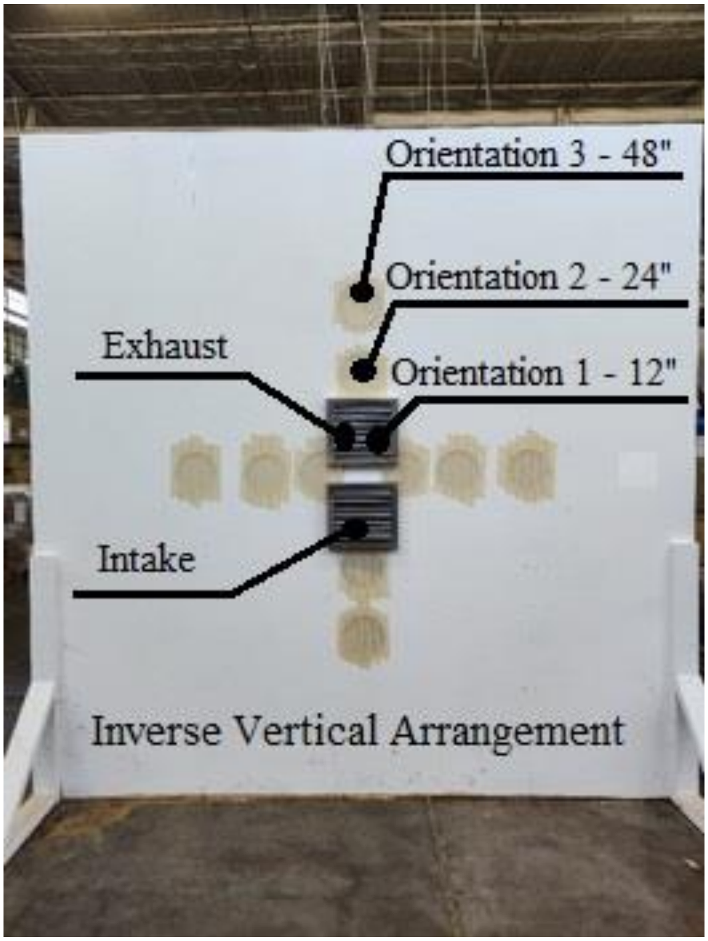

Figure 15: Vertical and Inverse Vertical Orientation 1 (O1)

Figure 16: Vertical and Inverse Vertical Orientation 2 (O2)

Figure 17: Vertical and Inverse Vertical Orientation 3 (O3)

The ventilation grills are attached to 6-inch diameter ductings, which are not shown in the above figures as they are located on the other side of the white mounting board. The level of the ducting and grill is verified via a digital level with an accuracy of +/- 0.1°. All connections, including the unused holes in the wall, as seen in the previous figures, are sealed with masking tape to ensure zero leakage occurs during a test. It should be noted that all tests were performed in an uncontrolled environment in an effort to replicate real-world conditions.

Inverse Vertical Orientation 1 (O1)

The O1 inverse vertical orientation, with the vents being the closest at 12” apart center-to-center, showed the highest crossover percentage among all setups, reaching a maximum atmospheric corrected crossover (XO_A) of 76.9% at volumetric flowrates of 200 cfm. In other words, this means nearly 80% of the contaminants exhausted from a building would be pulled into the intake duct and returned to the interior of the building. Figure 18 through Figure 21, representing flow rates of 100, 150, 200, and 250 cfm respectively, show the crossover percentage for exhaust CO_2 concentrations ranging from 1000 to 1900 parts-per-million (ppm). As a reminder, data labeled “XO_A” indicates it has been normalized with respect to ambient CO_2 concentrations, while data labeled “XO_{NA}” indicates it has not been normalized with respect to ambient CO_2 concentrations.

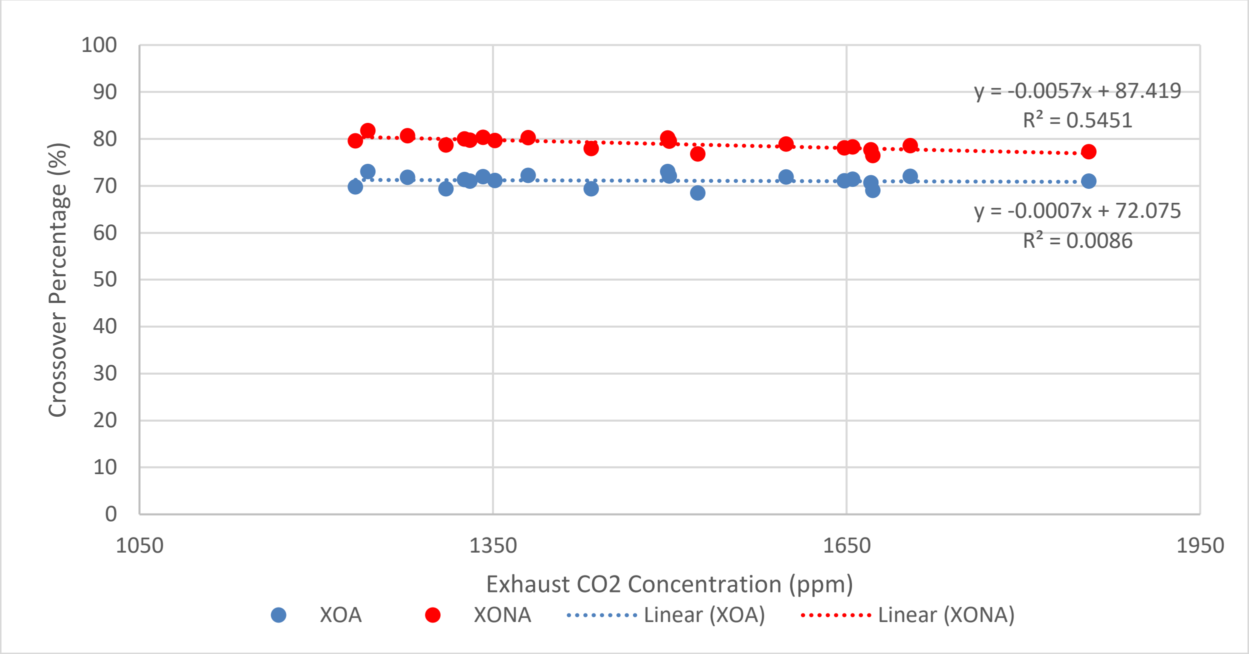

Figure 18: 100 CFM Inverse Vertical O1

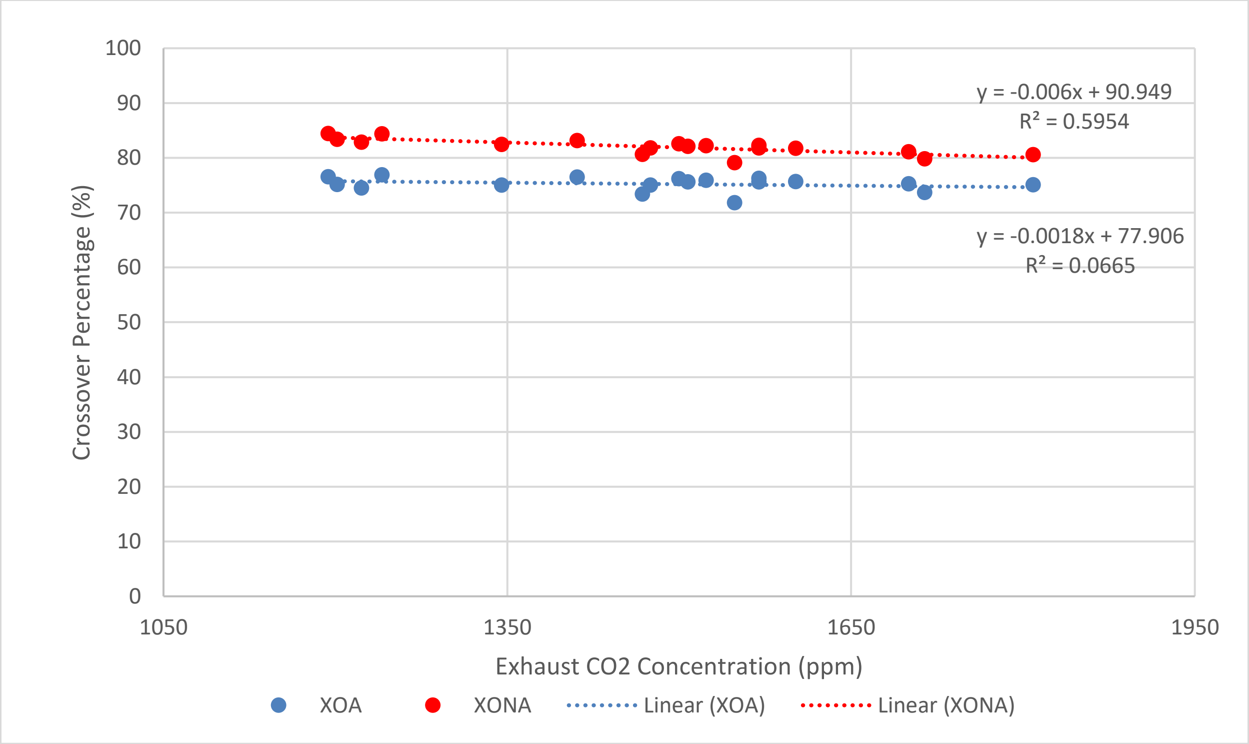

Figure 19: 150 CFM Inverse Vertical O1

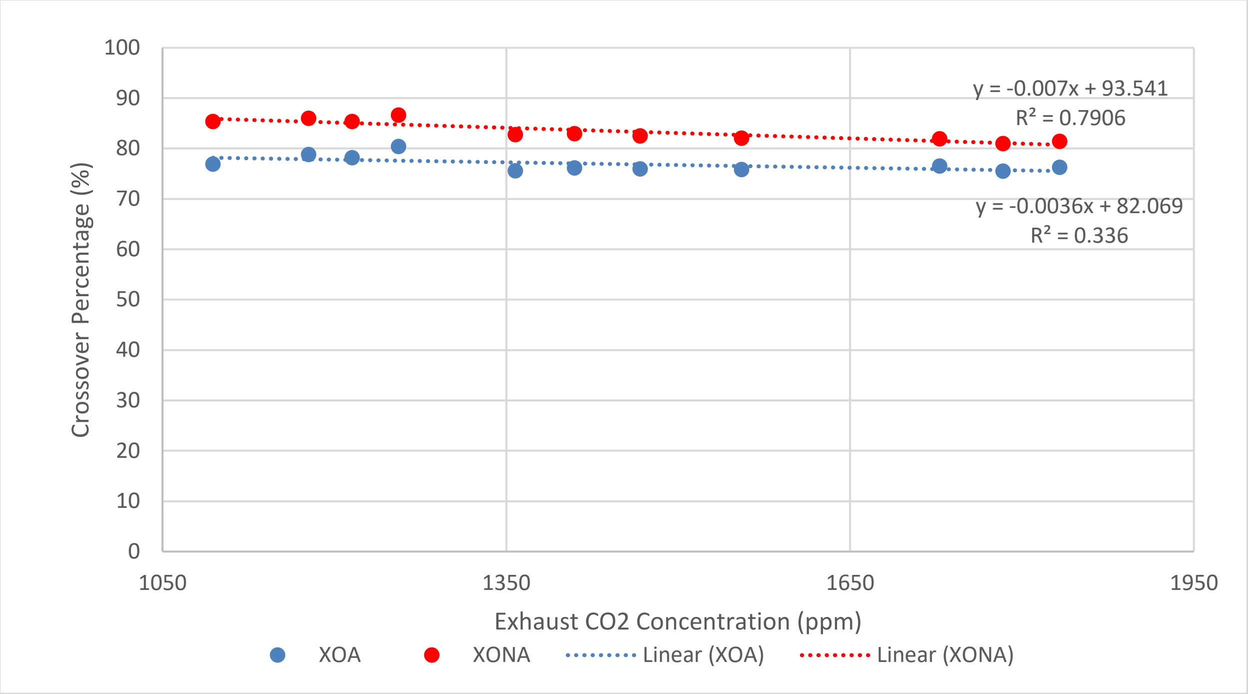

Figure 20: 200 CFM Inverse Vertical O1

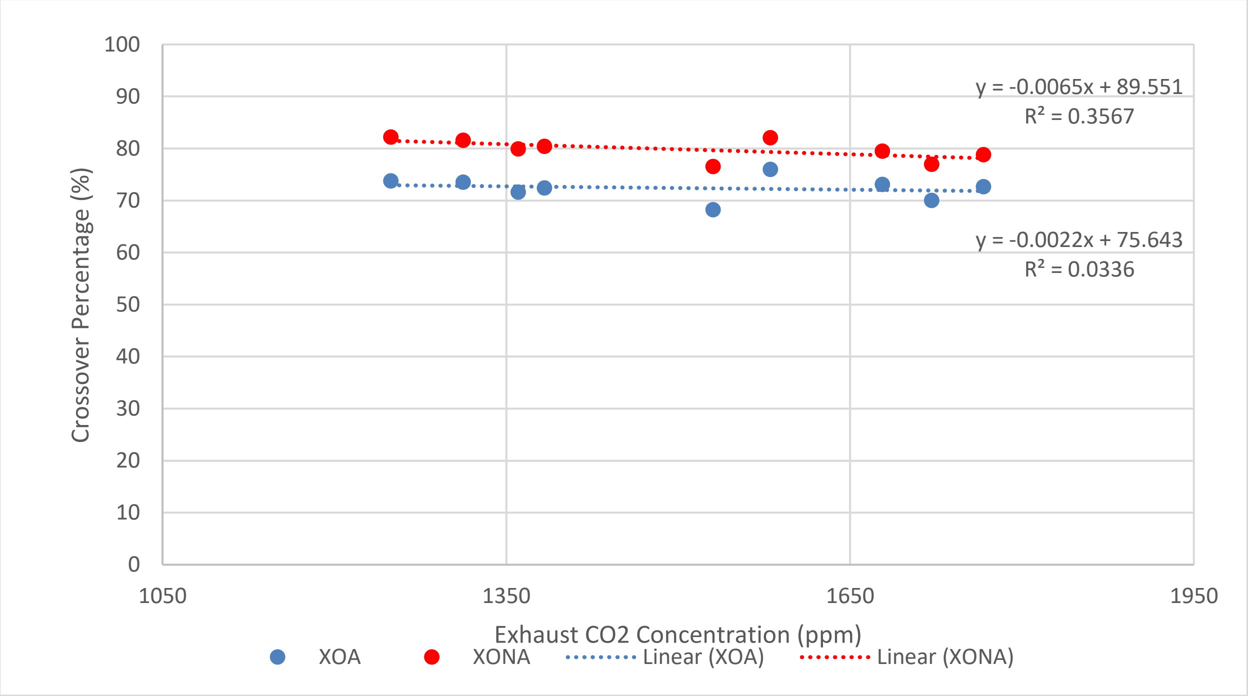

Figure 21: 250 CFM Inverse Vertical O1

The crossover percentage for all flowrates is noticeably higher when the values are not adjusted for the ambient CO_2 concentrations. For the first orientation (O1), there is approximately a 10% difference between XO_A and XO_{NA} regardless of flow rate. Additionally, as the exhaust CO_2 increases the perceived crossover decreases for the XO_{NA} case, while it remains fairly constant for the XO_A case across all exhaust concentrations. Because of this finding, further detailed comparisons between orientations, flow rates, and other variables will be confined to values normalized to atmospheric CO_2 readings; however, both XO_A and XO_{NA} results will be presented to show how the data of these two approaches differs for all setups.

Based on observations and comparisons of Figure 18 through Figure 21, the crossover percentage (mixing) increases by approximately 3-4% for each 50 cfm increase in airflow rate. The one exception is when the flow rate is increased from 200 to 250 cfm, then the crossover percentage decreases. The difference between the uncorrected (XO_{NA}) and atmospherically corrected crossover (XO_A) for this setup is fairly uniform across the exhaust CO_2 concentration range, which is to say the difference between these two values is more-or-less the same at extreme exhaust concentrations of 1200ppm and 1800ppm for the four flowrates tested. This is because there is a much higher concentration of carbon dioxide in the intake duct (due to mixing) and as a result, the ambient carbon dioxide levels in the atmosphere impact the calculation less severely at lower concentrations.

A direct comparison of the normalized crossover (XO_A) for the four flowrates is shown in Figure 22 below. With the increase in flow rate from 200 to 250 cfm, the overall crossover percentage for 250 cfm decreases to 72.5% for O1 which exhibits crossover results between 100 and 150 cfm. In addition to the calculated average crossover values for the four flowrates, Table 5 also presents their corresponding standard deviation, standard error, and uncertainties. As evidenced in Table 5, the calculated crossover continued to increase up to 200 cfm from 70% to 77% while maintaining an approximate uncertainty of 9%. The standard deviation of the calculated crossover percentage across all tests at a given flow rate showed a minimum and maximum of 0.7% and 2.1% at 150 and 250 cfm, respectively.

Table 4: Inverse Vertical O1 Statistical Results

Flowrate (cfm)	**100**	**150**	**200**	**250**
Average XO_A (%)	70.1	75.7	76.9	72.5
Std. Dev. (%)	1.17	0.73	1.57	2.13
Std. Error (%)	0.26	0.17	0.47	0.67
Uncertainty (%)	9.07	9.38	9.61	8.99

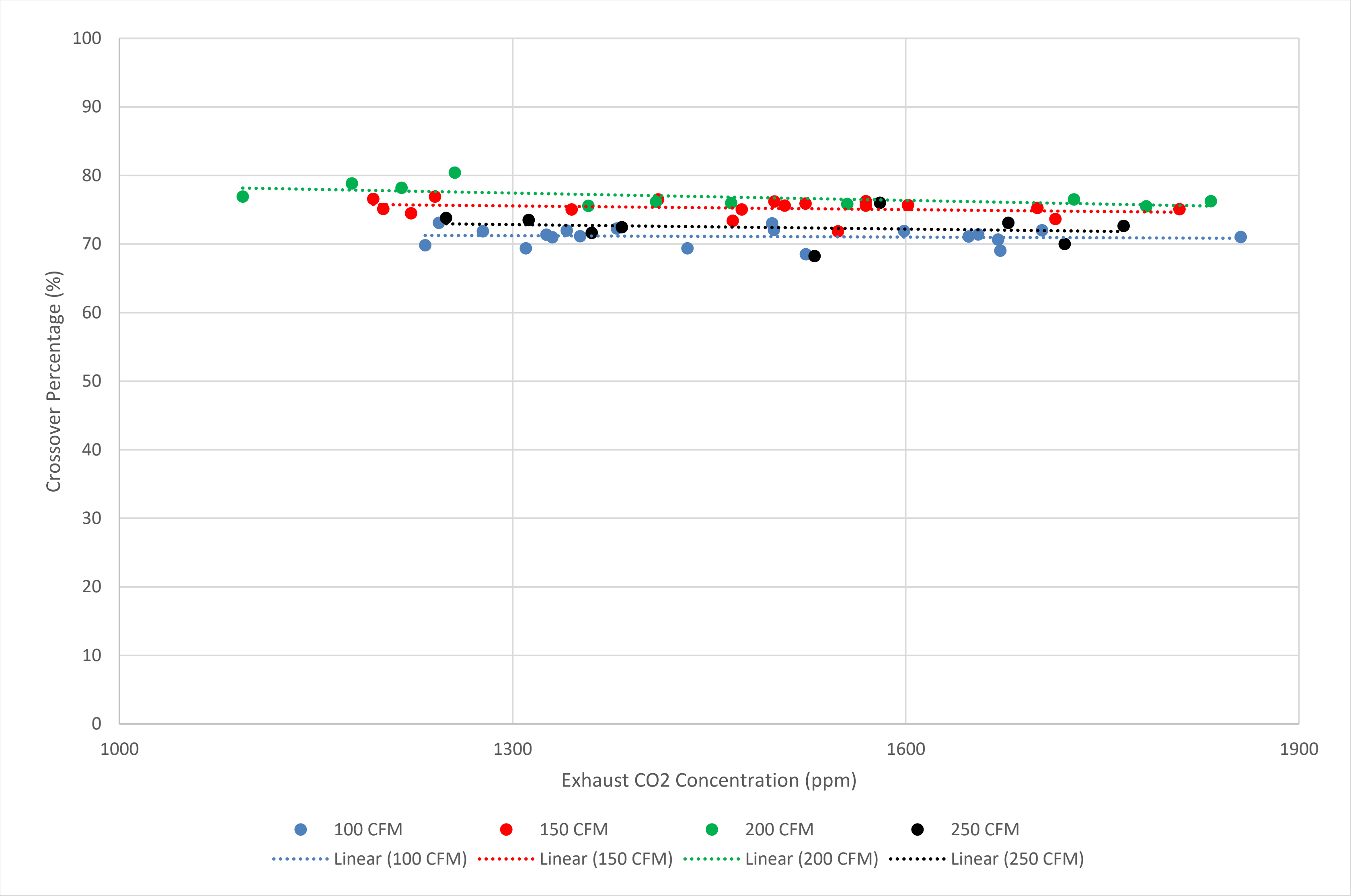

Figure 22: Flow-Rate Comparison: Inverse Vertical O1 – Normalized (XO$_A$

Inverse Vertical Orientation 2 (O2)

Similar to the Inverse Vertical Orientation 1, the second inverse vertical orientation follows the trend of increasing crossover percentage as the flowrate increases. However, because the distance between the intake and exhaust is doubled from 12” to 24”, the crossover percentage is reduced. Specifically, as will be shown later there is approximately a 15 to 20% decrease in CO_2 crossover by increasing the spacing between the intake and exhaust from 12” to 24”. This crossover decrease is to be expected as there is more air volume between the intake and exhaust, which allows the carbon dioxide to dissipate, especially in an environment where external air currents are not controlled, which is more representative of a real-world installation.

Figure 23 through Figure 26 show the crossover percentage for 24” spacing, or Orientation 2 (O2), at 100, 150, 200, and 250 cfm, respectively. Similar to Orientation 1 (O1), a drop in crossover can be seen between 200 and 250 cfm. As can be seen from the four figures, from 100 to 200 cfm the crossover increases as the flowrate increases, and decreases from 200 to 250 cfm which is in-line with the results obtained from the first orientation.

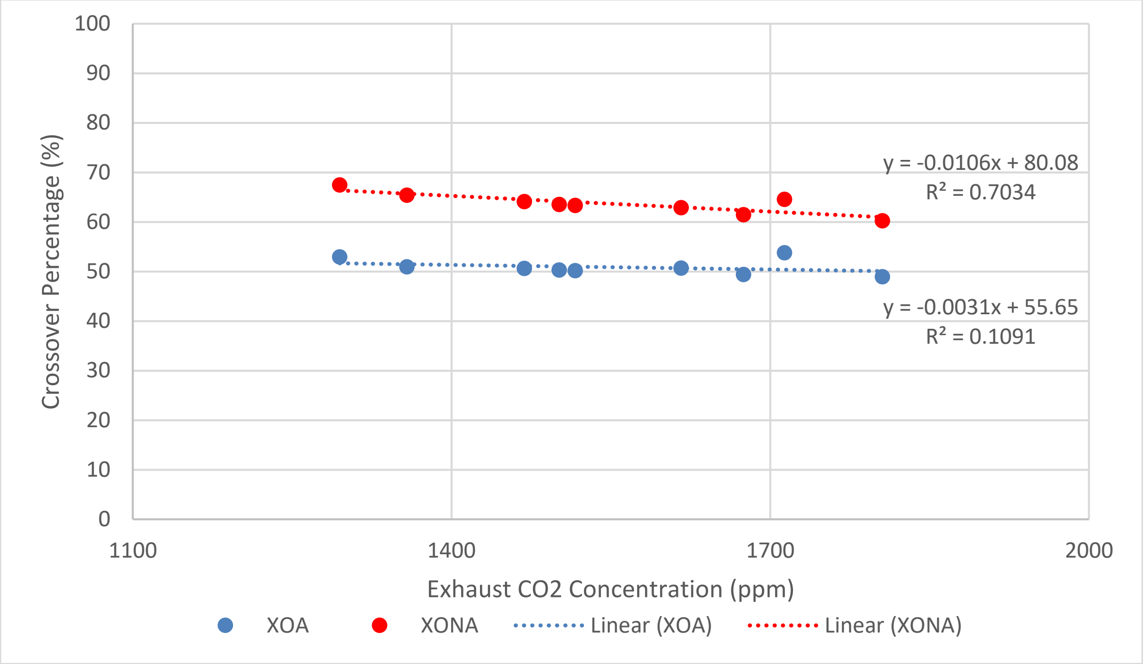

Figure 23: 100 CFM Inverse Vertical O2

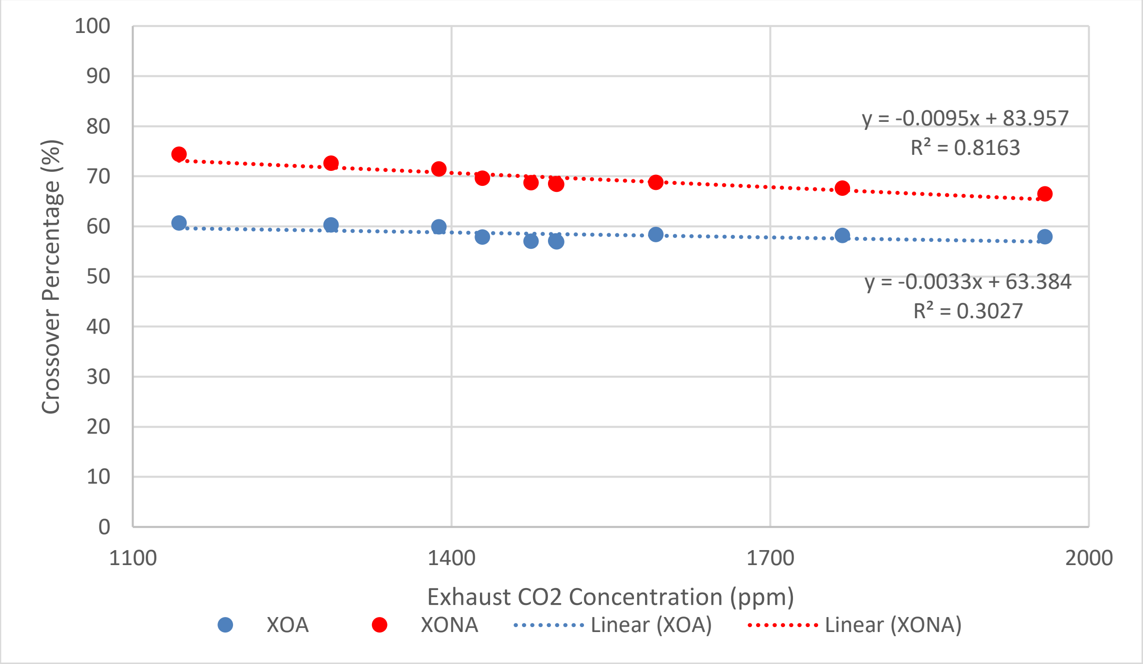

Figure 24: 150 CFM Inverse Vertical O2

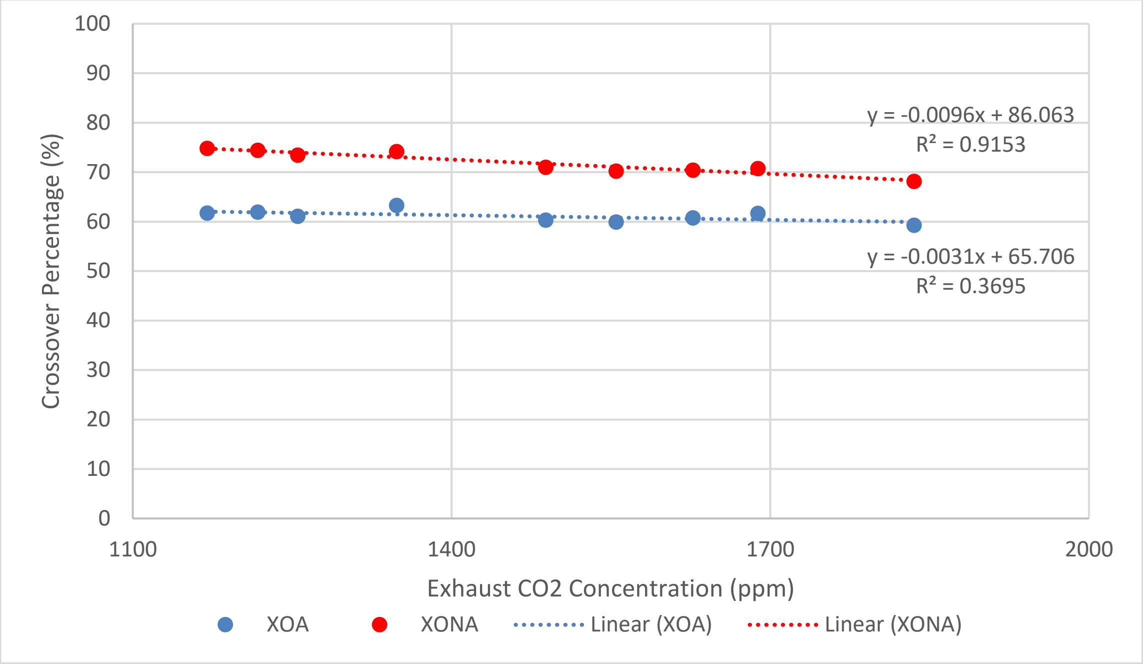

Figure 25: 200 CFM Inverse Vertical O2

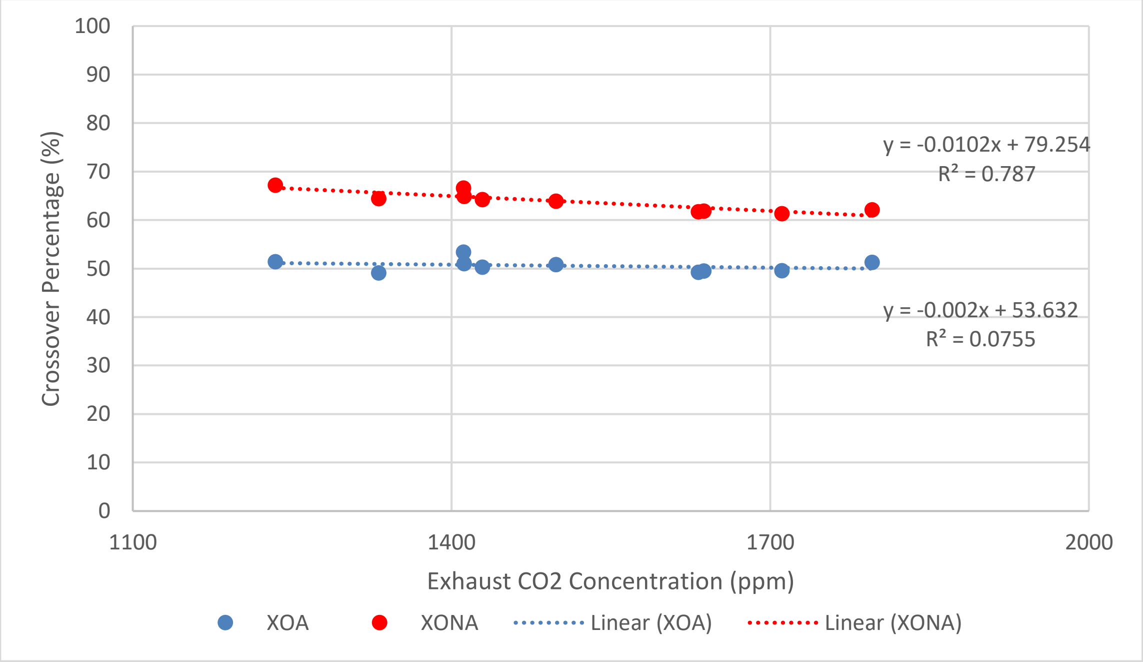

Figure 26: 250 CFM Inverse Vertical O2

A consolidated graph of the corrected crossover (XO_A) versus exhaust CO2 concentration for the four flow rates is displayed in Figure 27. As can be seen from this graph the crossover percentage for 100 and 250 cfm is more-or-less equivalent showing that as flow rate, or air velocity in a given duct size, is increased, it does not always correlate to an increased mixing between the inlets and outlets at a building's interface. Referencing Figure 27, it is easily visible that at 24" spacing the mixing for all four flowrates is contained between 50 and 60%. Similar to Orientation 1, it can be inferred that increased distance between the intake and exhaust plays a significant factor in the reduction of carbon dioxide crossover. Additionally, the data trends of the second orientation being in-line with the first orientation's findings (increasing crossover to 200 cfm) encourage confidence in the data.

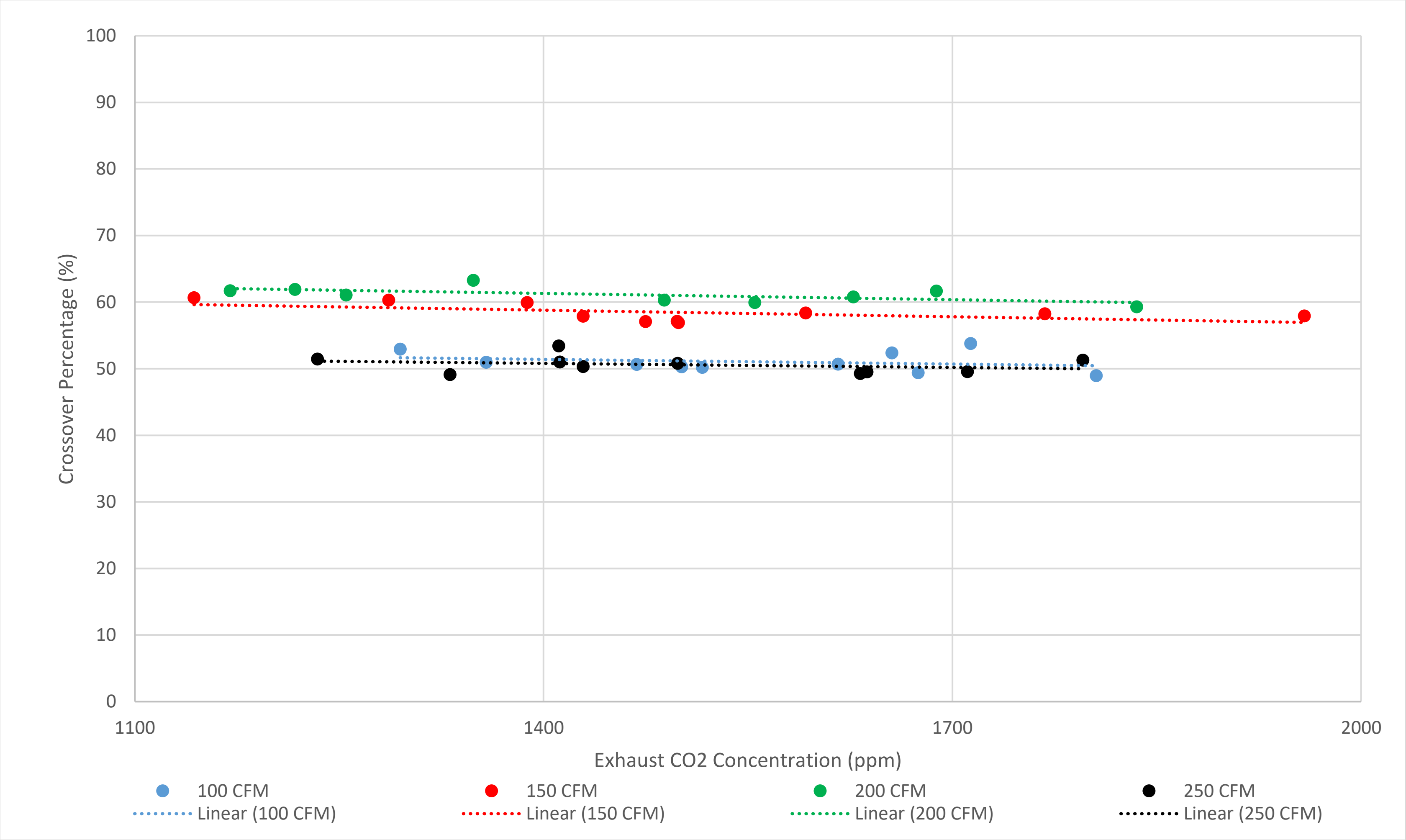

Figure 27: Flow-Rate Comparison: Inverse Vertical O2 – Normalized (XO_A)

The averaged corrected crossover (XO_A), as well as the corresponding standard deviation, standard error, and uncertainties for the second orientation is presented below in Table 5. The standard deviation and standard error of the data for the second orientation (O2) is fairly consistent across all four flowrates, with the standard deviations ranging from 1.32% to 1.56% and the standard error staying under 0.5%. The uncertainties range from 7.2 to 8.5% which is less than the first orientation by about 1%, although the crossover for the second orientation ranges from approximately 51% to 61% for 100 cfm through 200 cfm, respectively.

Table 5: Inverse Vertical O2 Statistical Results

Flowrate (cfm)	**100**	**150**	**200**	**250**
Average XO_A (%)	50.9	58.4	61.1	50.6
Std. Dev. (%)	1.56	1.38	1.28	1.32
Std. Error (%)	0.49	0.44	0.43	0.42
Uncertainty (%)	7.21	8.10	8.51	7.45

Inverse Vertical Orientation 3 (O3)

Continuing the analysis performed on the first (O1) and second (O2) orientations, the third (O3) inverse vertical orientation for the inverse vertical arrangement, reveals similar trends. Specifically, it can be observed that an overall decrease in intake/exhaust mixing occurs due to the increase in distance between the inlet and outlet. In this instance, the spacing is increased by 24” total, or 12” per ventilation grill, starting from a 12” spacing, from the centralized reference point. It is important to note that while the spacing between both the O1/O2 and O2/O3 orientations effectively doubled, 12” to 24” and 24” to 48”, respectively, the increase in distance from O2/O3 is twice the linear distance when compared to the O1/O2 increase (12” vs. 24”). This change in distance also holds true for all of the standard vertical and horizontal arrangements studied in this paper.

Although the distance is doubled for the third orientation, the total crossover does not decrease as significantly from O2 to O3 as it did from O1 to O2; however, the correlation between increasing crossover and increasing flowrate until 200 cfm remains valid. Figure 28 through Figure 31 show the crossover for the four flow-rates and the exhaust CO_2 concentrations were varied from approximately 1000-2000ppm. It can be seen that the crossover increased from 40% at 100 cfm to 45.7%, and 48.3% at 150 and 200 cfm, respectively, and then decreased by 1.7% to 46.6% at 250 cfm.

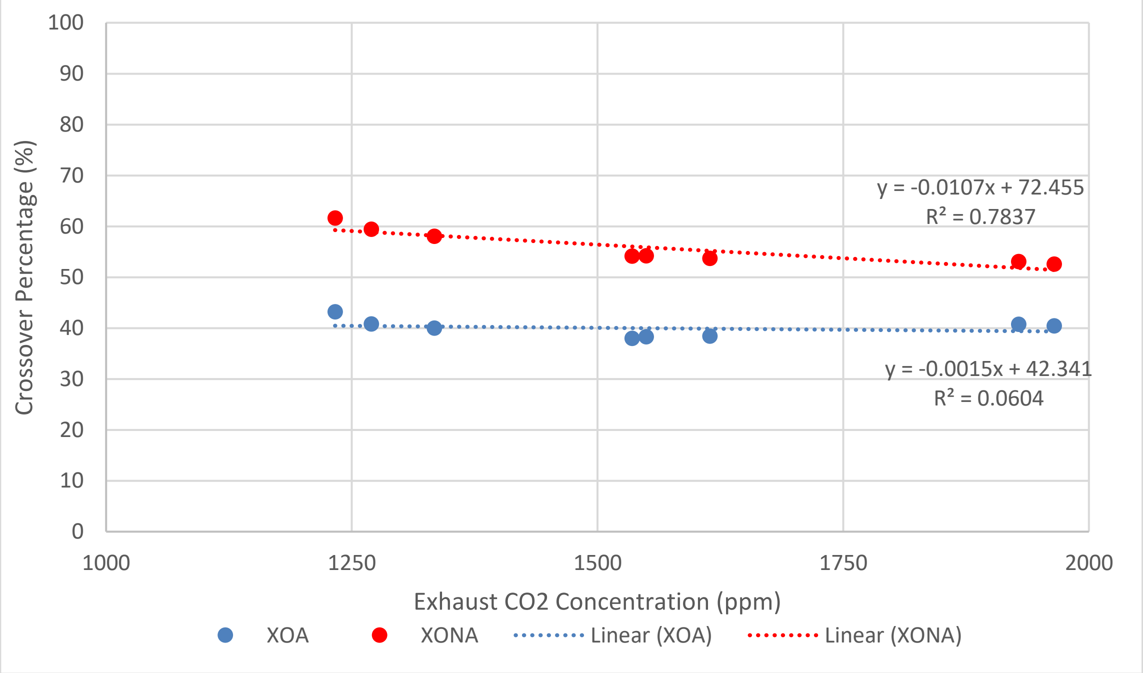

Figure 28: 100 CFM Inverse Vertical O3

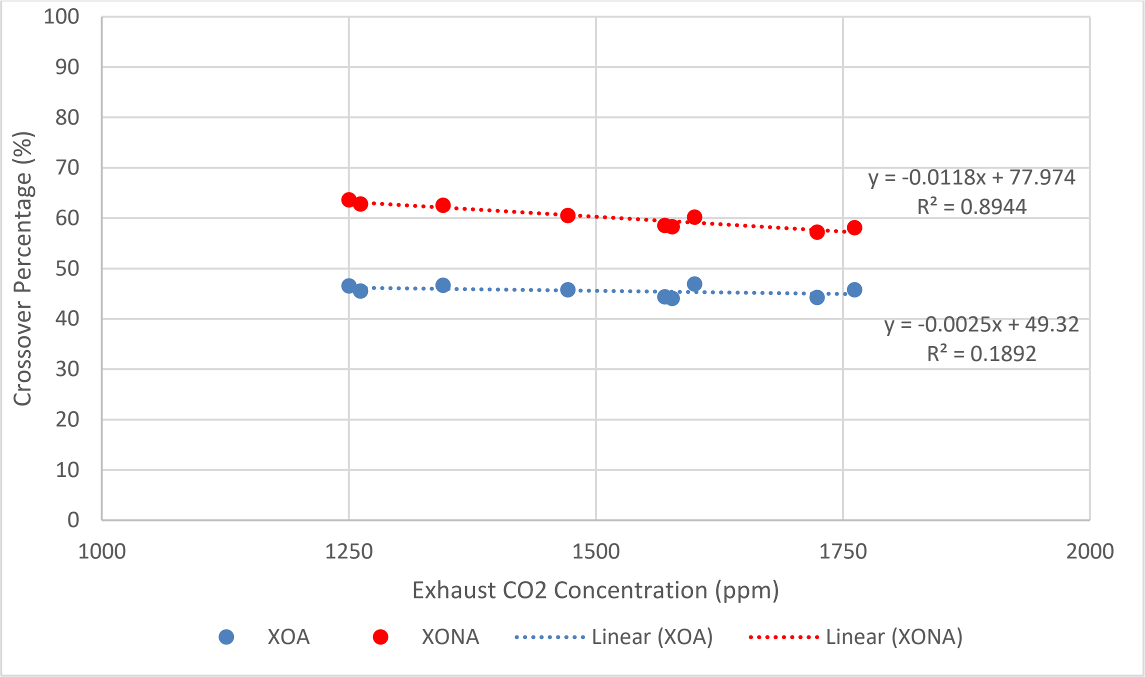

Figure 29: 150 CFM Inverse Vertical O3

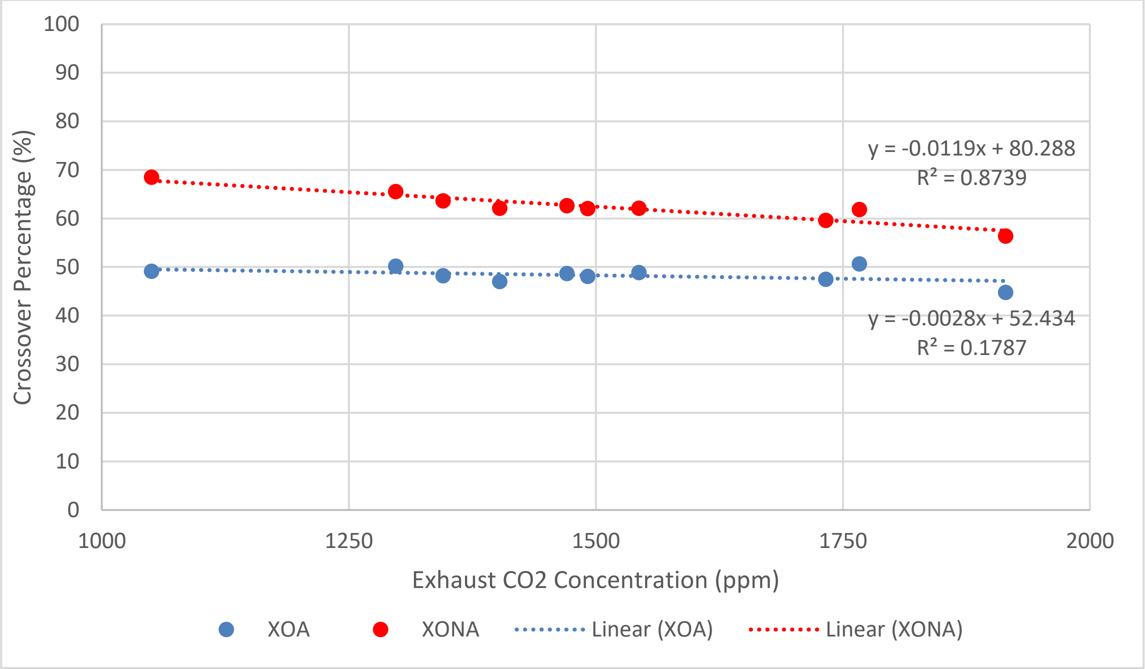

Figure 30: 200 CFM Inverse Vertical O3

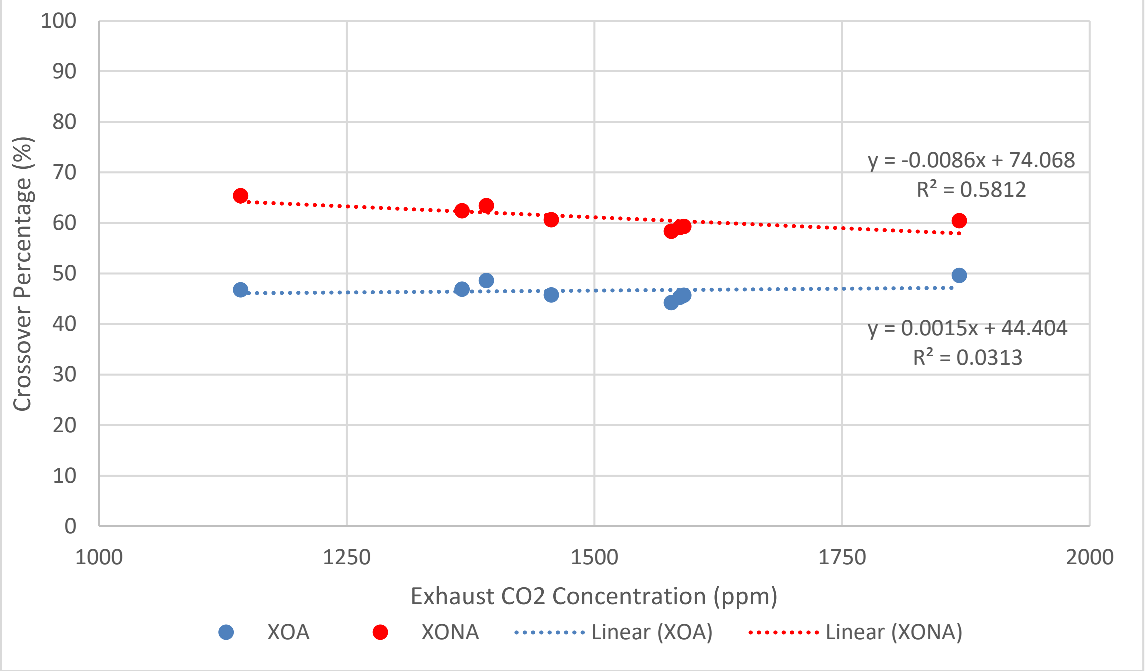

Figure 31: 250 CFM Inverse Vertical O3

As can be seen from the figures, all flow-rates had larger negative slopes for uncorrected crossover rates and smaller negative slopes for the corrected values, on the order of 1/4th to 1/5th that of the uncorrected values. For instance, Figure 31 revealed slopes for XO_{NA} of -0.0086 while slopes of XO_A were -0.0015, revealing less variation in crossover percentage across the exhaust concentration range of 1000 to 2000ppm. Due to difficulty in controlling CO_2 exhaust pressure at the various flow rates, there are instances where multiple tests were performed at similar exhaust concentrations. The benefit to this is it reveals fairly strong repeatability for this experimentation setup by achieving similar results during distinct tests.

Similar to the first and second orientation analysis, the four flow rate experiments are compiled in Figure 32 in order to give an overall view of how the results of each experiment compare to each other on a master scale. There are two conclusions to draw from Figure 32. Firstly, there is a much larger increase in crossover from 100 to 150 cfm than any other two flow-rates, and secondly 250cfm has a lower crossover than 250 cfm. Additionally, the spread between the four flow-rates is fairly consistent with the results from O1 and O2, with O3 revealing a total XO_A spread of 8.3% while O2 and O1 possessed spreads of 10.5% and 6.8%, respectively.

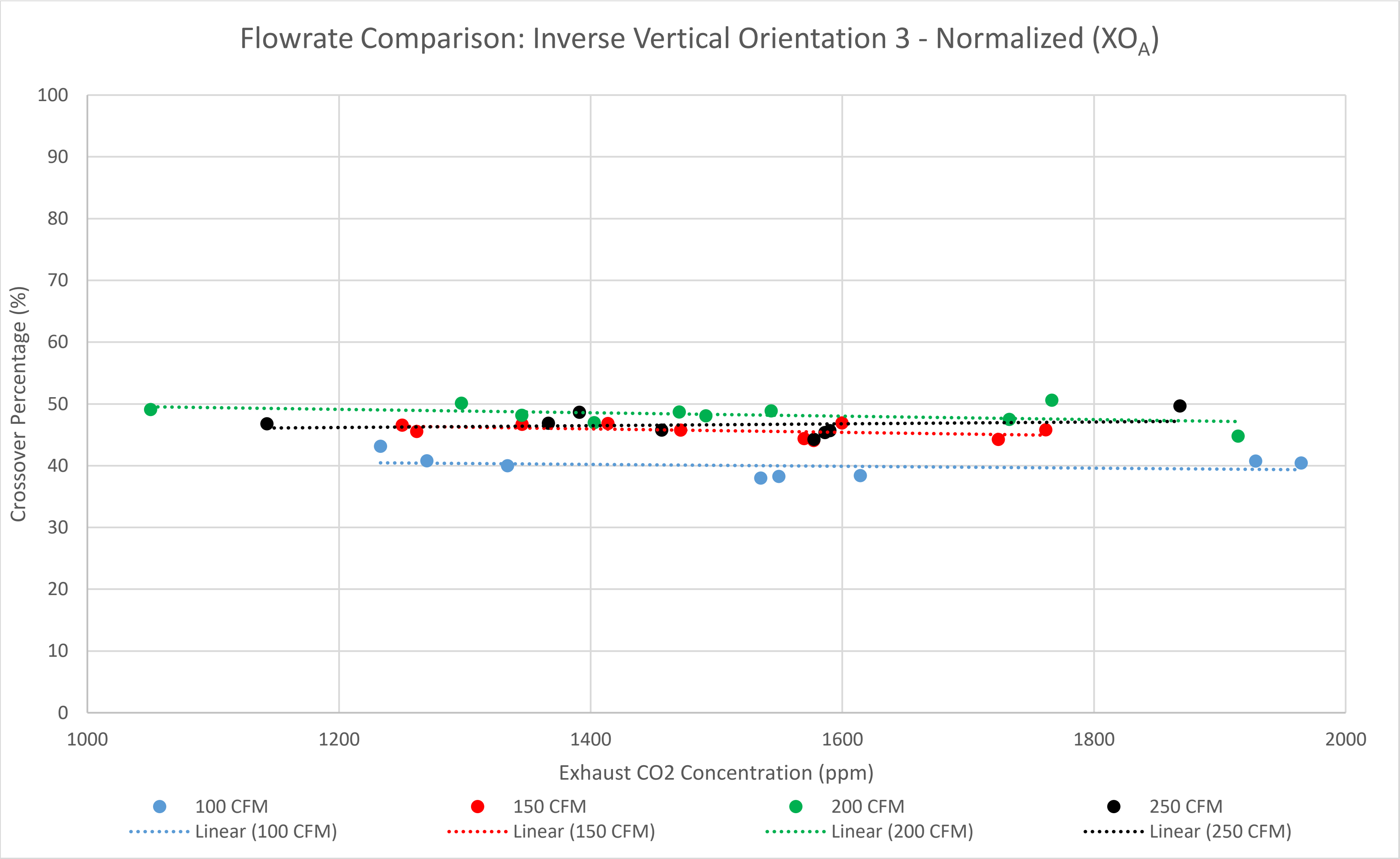

Figure 32: Flowrate Comparison: Inverse Vertical O3 – Normalized (XO_A)

A breakdown of the results of the third orientation are presented in Table 6.As can be seen from Table 6, the standard deviation and standard error for the third orientation are similar to the first and second orientations, in that the standard deviation is between 1 and 2% while the standard error is below 1%. The uncertainties in the calculated crossover (XO_A) are most similar to the second orientation with minimums of 7.2% versus 7.3% and maximums of 8.5% versus 7.9% for O2 and O3, respectively.

Table 6: Inverse Vertical O3 Statistical Results

Flowrate (cfm)	**100**	**150**	**200**	**250**
Average XO_A (%)	39.97	45.68	48.29	46.62
Std. Dev. (%)	1.73	1.1	1.65	1.78
Std. Error (%)	0.61	0.35	0.52	0.63
Uncertainty (%)	7.27	7.65	7.92	7.76

Inverse Vertical Comparisons and Conclusions

Three distinct experimental setups (O1, O2, and O3) with four flow-rates per setup (100, 150, 200, and 250cfm) were performed for the inverse vertical arrangement resulting in 12 total configurations. When comparing the three orientations in Table 7, there are several points to address. Firstly, the raw crossover percentages (XO_A as calculated previously) for the third orientation (O3) when compared to the second orientation (O2) dropped approximately 10.9, 12.7, 12.8, and 4.0 percent for 100, 150, 200, and 250 cfm respectively. This is in contrast to the larger decreases of approximately 19.3, 17.3, 15.8, and 21.8 percent from O1 to O2, which reveals a greater decrease in crossover between O1 and O2 for all flowrates tested than compared to O2 to O3. This being said, when taking into account the relative change, or the difference relative to the previous measurement, the decrease for these two scenarios is quite similar with respect to the previous measurements as presented in Table 7.

Table 7: Inverse Vertical XO_A Change Between Orientations

Raw Change (%)

Flowrate (cfm)	**100**	**150**	**200**	**250**
O1 to O2	-19.3	-17.3	-15.8	-21.8
O2 to O3	-10.9	-12.7	-12.8	-4.0

Relative Change (%)

Flowrate (cfm)	**100**	**150**	**200**	**250**
O1 to O2	-27.5	-22.8	-20.6	-30.2
O2 to O3	-21.4	-21.8	-21.0	-7.8

Table 7, with the exception of 250 cfm, reveals the relative change between the orientations was fairly similar, even though the distance increase from O2 to O3 is double that of O1 to O2. This is indicative that there is a distance where crossover begins to level off for this orientation, but may require several increases in intake and exhaust spacing to take place before that occurs.

The numerical results for each of the twelve experimental setups, which were presented in figures and tables previously, were compiled on a bar graph to allow for a visual representation of the progression of CO_2 crossover mixing is shown below in Figure 33 for various orientations (spacing's) and flow rates. Figure 33 reveals two points of interest for all three orientations. Firstly, the crossover increased until 200 cfm and then decreased from 200 to

250 cfm, this holds true for all orientations, and secondly, the crossover decreased at each flow-rate as the distance increased, i.e O1 to O2. Additionally, the uncertainties are included for each setup which highlights the fact that as intake and exhaust spacing is increased, there is a greater commonality between O2 and O3 than O1 and O2. While a constant decrease between each orientation for a given flow-rate is not observed, Figure 33 highlights the fact that increasing the intake and exhaust spacing is the primary driving factor behind reducing unwanted crossover.

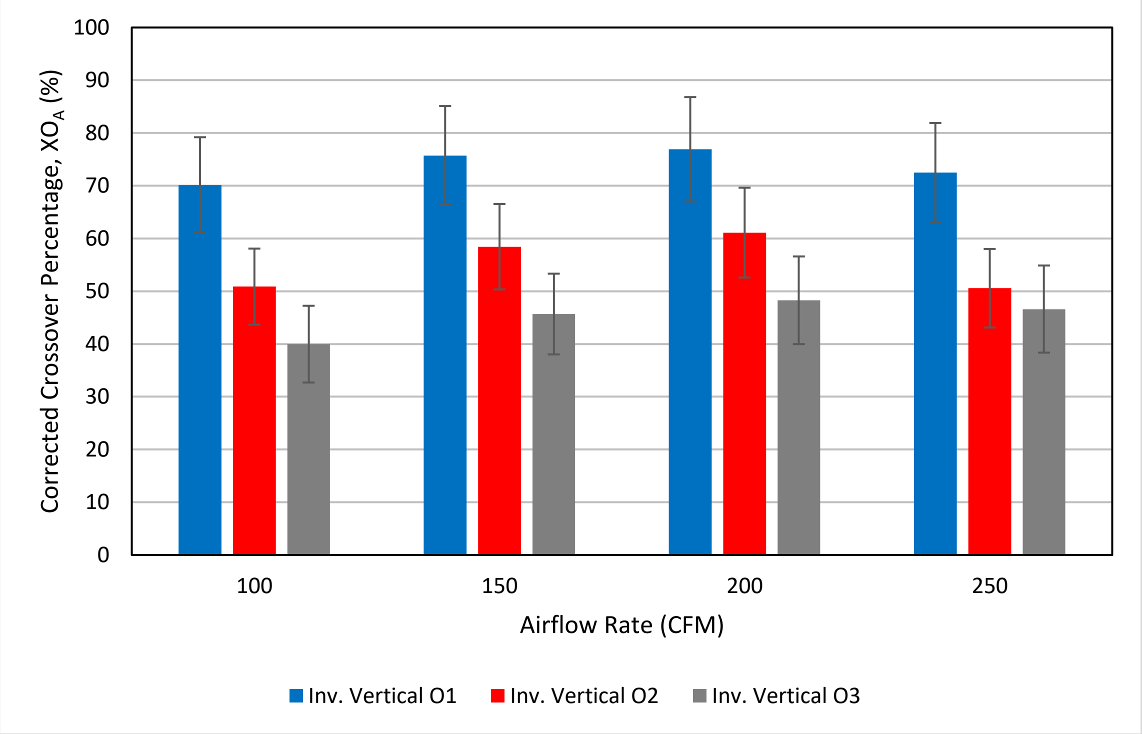

Figure 33: Inverse Vertical CO_2 Crossover Percentage (XO_A) vs. Flow-Rate

Additional insights into unwanted crossover mixing is presented in Figure 34 . Specifically, Figure 34 shows the relationship between the corrected crossover (XO_A) with respect to increasing the intake and exhaust distance at a given flow rate. The plotted data and a second order polynomial shows crossover missing decreasing for all flow rate increases, with a leveling of this effect decreasing as spacing increases to 48”.

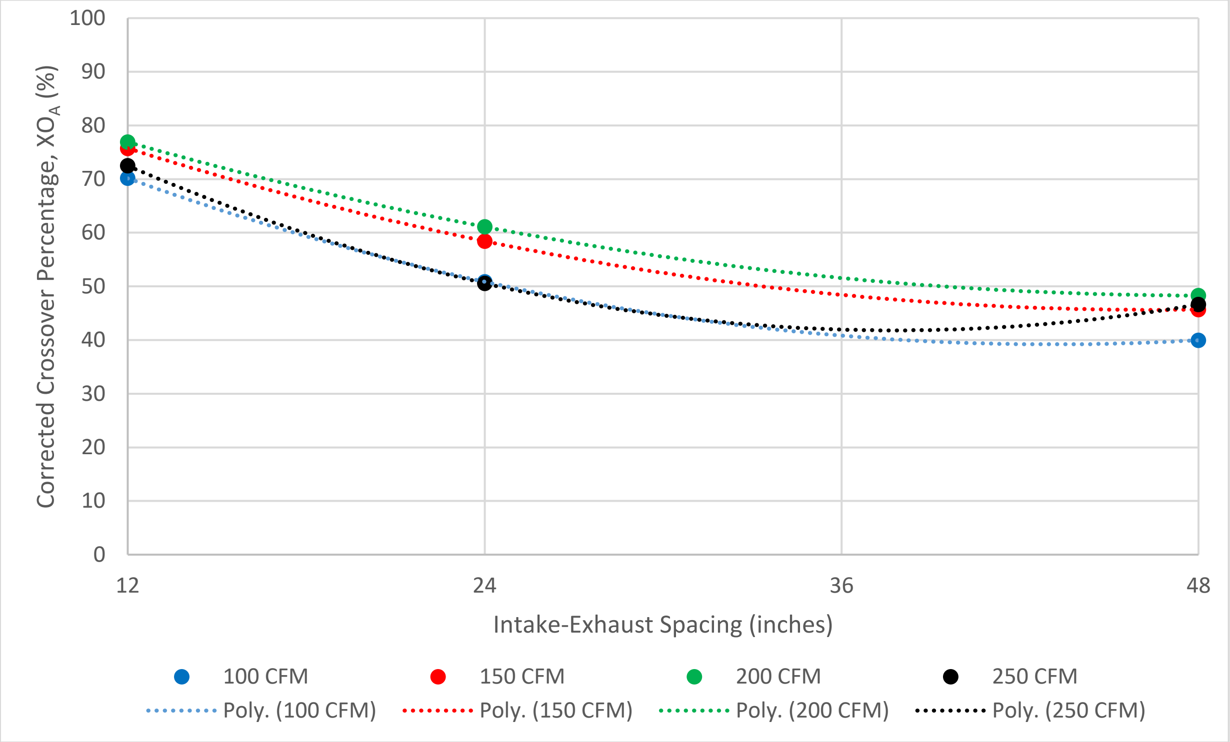

Figure 34: Inverse Vertical Corrected Crossover (XO$_A$) vs. Intake-Exhaust Spacing

To wrap-up the inverse vertical experiments, the importance of the results obtained highlight that residential installations should avoid positioning the exhaust above the intake. The rationale behind this statement is that the lowest crossover measured is 40% at 48” separation and 100 cfm. It naturally follows that in order to bring this value to an acceptable level, significant separation is required due to the crossover leveling effect as witnessed in Figure 34. Referencing the ASHRAE Classes of Air presented in Chapter II, because the crossover is greater than 10%, air exhausted from a Class 2 location, such as a cafeteria, cannot be recirculated. Similarly, because the crossover is greater than 5%, air exhausted from a Class 3 location, such as a restroom, cannot be recirculated. The inability to recirculate air from these locations limits intake and exhaust port locations for HVAC system and component and should be considered by designers for future constructions.

CHAPTER VI

VERTICAL ARRANGEMENT EXPERIMENTS

Similar to the inverse vertical arrangement presented in Chapter V, the vertical arrangement utilizes the same hole locations for duct connections and the same distances for the three orientations; however, the one major change, is that the location of the exhaust and intake ventilation grills are reversed, meaning the top ventilation grill becomes the intake while the bottom ventilation grill becomes the exhaust. Additionally, only the first and second orientations (O1 and O2) are tested and evaluated in this paper as experiments for the third orientation (O3) yielded results that were below an acceptable level of uncertainty for the CO_2 sensors used in this research. As noted previously, this particular experimental setup and test conditions mimic the majority of residential and light commercial installations.

Vertical Orientation 1 (O1)

Due to the placement of the intake and exhaust for the vertical setup being the reverse of the previous setup, the crossover percentage is reduced for all instances with respect to the inverse vertical setup. Figure 35 through Figure 38 presents the results for the test flow rates of 100 cfm through 250 cfm, respectively. Similar to the inverse vertical arrangement for Orientation 1 (O1), 100 cfm maintained the lowest crossover percentage, and as the flow rate was increased, the atmospherically corrected crossover (XO_A) increased. In other words, contrary to the previous inverse vertical setup and test results, the CO_2 mixing phenomena as measured by the atmospherically corrected crossover did not decrease for any flow rate increase, and instead, continued to increase up to the highest volumetric flow rate of 250 cfm.

The benefit of the atmospheric correction (XO_A) is visible in Figure 35 through Figure 38, in that although after the atmospheric correction the linear line of best fit for XO_A possess negative slopes, they are more-or-less constant across the selected exhaust concentration range with slopes an order of magnitude less than the uncorrected crossover (XO_{NA}), or -0.016 versus -0.0014 using Figure 36 as an example. This phenomenon is further explained in the paragraph that follows.

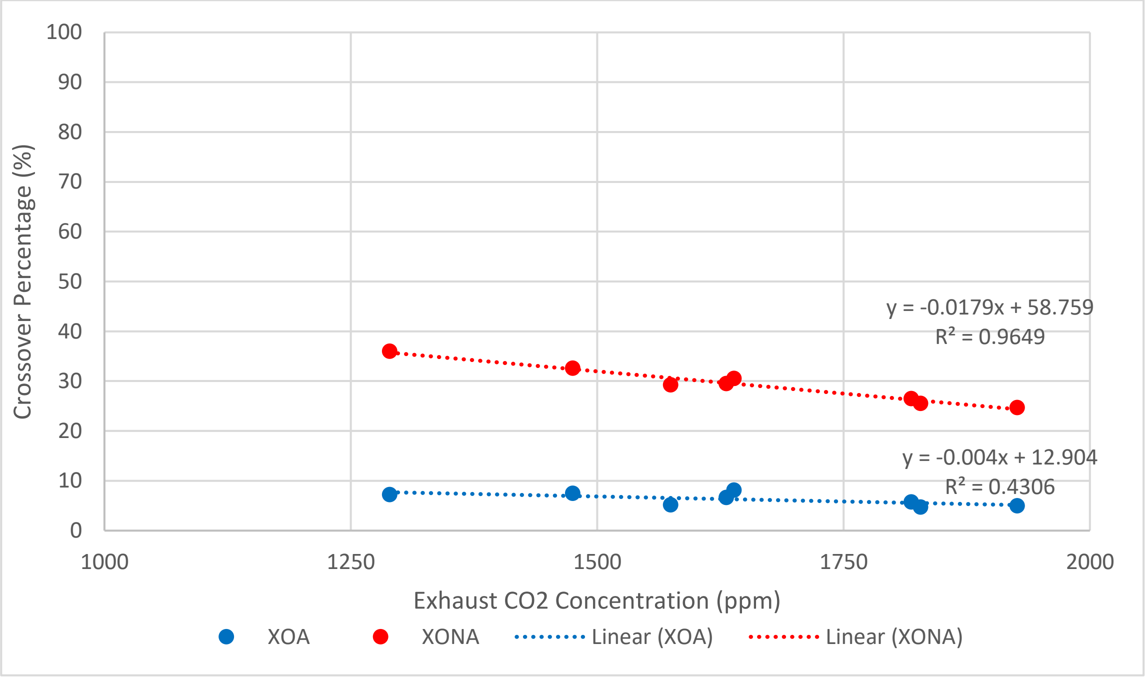

Figure 35: 100 CFM Vertical O1

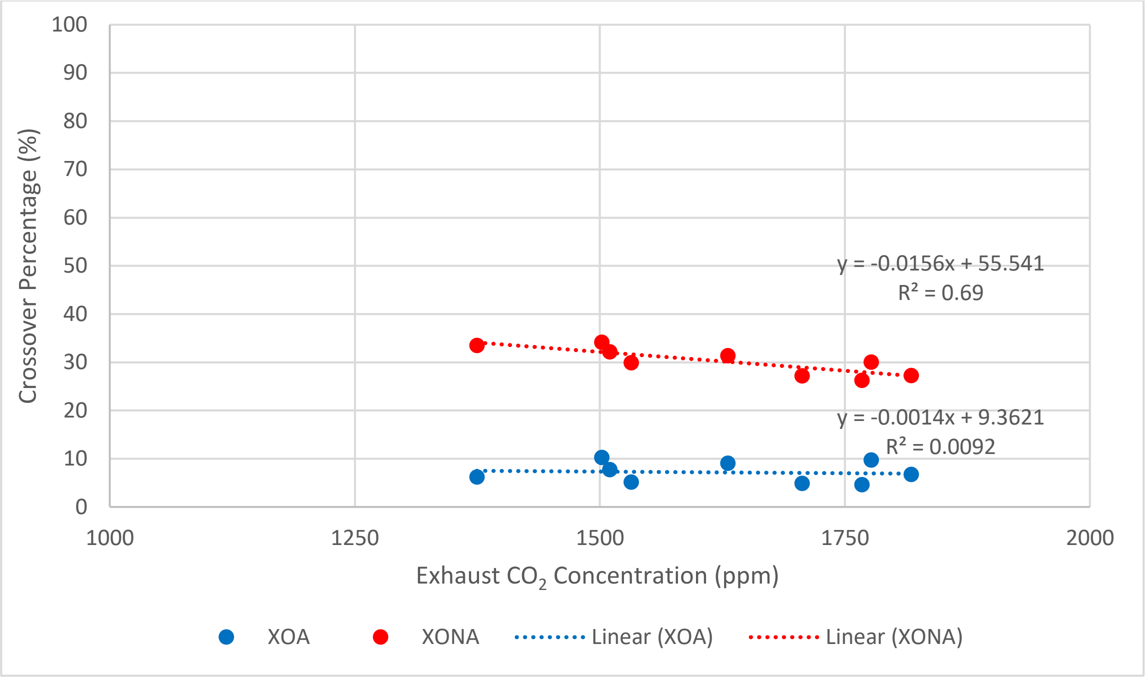

Figure 36: 150 CFM Vertical O1

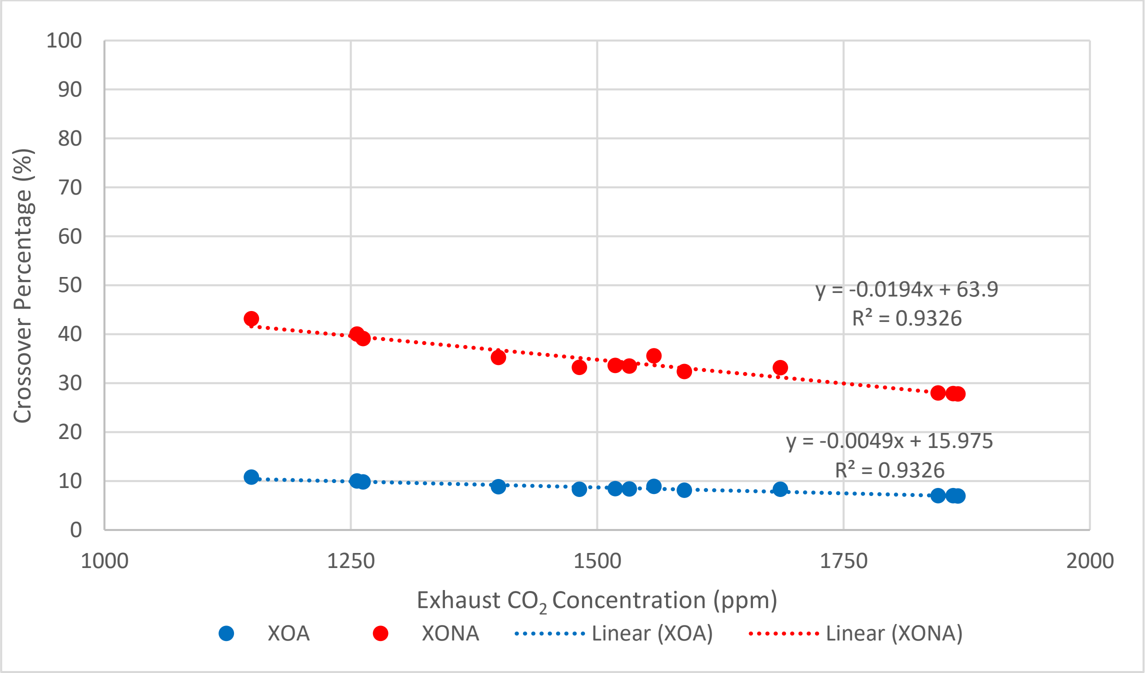

Figure 37: 200 CFM Vertical O1

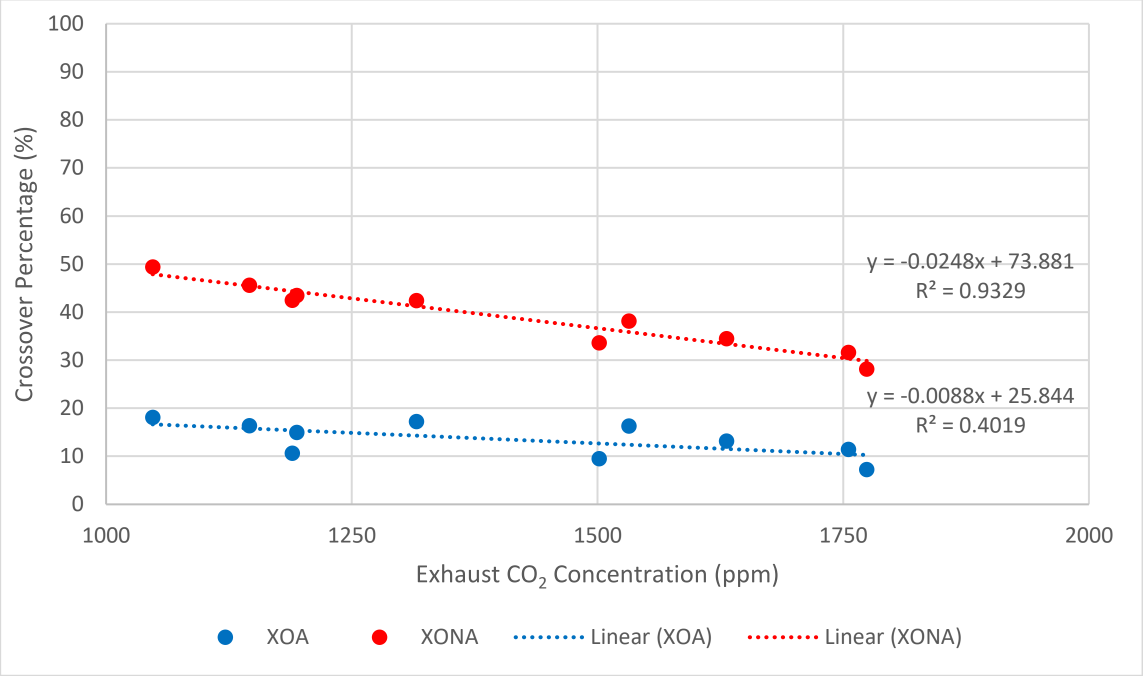

Figure 38: 250 CFM Vertical O1

Figure 39 combines all four flowrates into one plot for comparison purposes. It can be observed that there are minor differences in the corrected crossover percentages (XO_A) for the flow rates of 100, 150, and 200 cfm with an approximate 1% difference between each, while 200 to 250 cfm revealed a larger jump of 5%. It can be speculated that the reason for crossover percentage similarities in the 100 to 200 cfm range is due to a combination of the lower volumetric flow rates and the generally higher exhaust CO_2 concentrations for these tests, with both being significant factors in determining intake-to-exhaust mixing. Specifically, at low flowrates if the intake is unable to pull in an amount of CO_2 proportional to the increase in exhaust CO_2 concentration, then the perceived total crossover percentage will decrease with increasing exhaust CO_2 values.

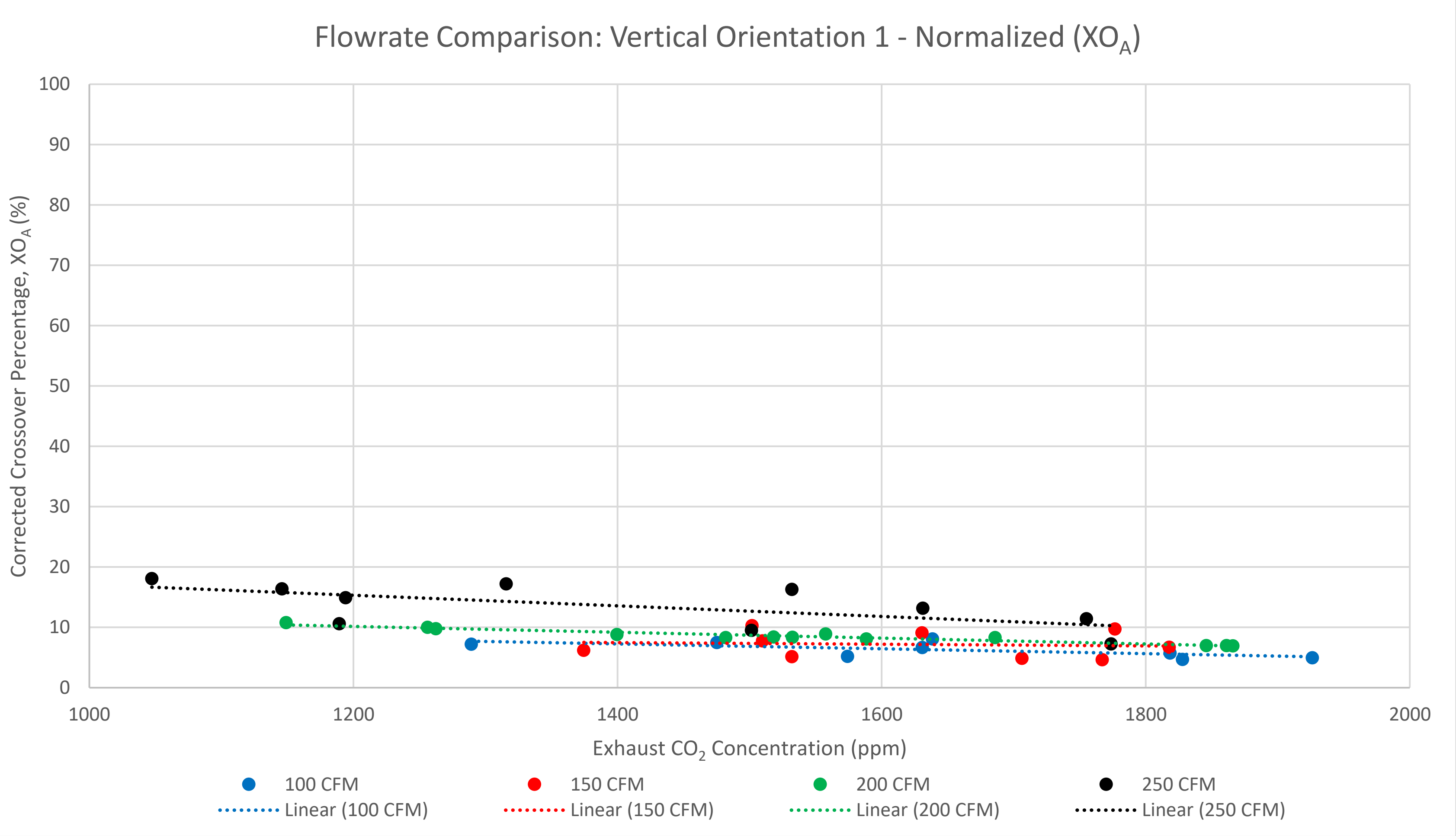

Figure 39: Flowrate Comparison Vertical O1 - Normalized (XO_A)

The calculated crossover averages for the adjusted results, as well as the standard deviation, standard error, and uncertainty are tabulated in Table 8 below. Although the averaged corrected crossover (XO_A) increases as flow-rate is increased, so does the uncertainty of the measurements. It is important to note that XO_A doubled from 100 to 250 cfm (6.25% to 13.5%) while the measurement uncertainty only slightly rose from 4.5% to 6%; however, the standard deviation tripled from 1.28% to 3.66% revealing a larger scattering at the higher flow rates across the exhaust CO_2 concentration range of 1000 to 2000ppm.

Eight unique tests were performed at the lowest flow-rate of 100 cfm, with a minimum and maximum calculated crossover values of 4.7% and 8.1%, respectively, while the ten tests performed at the highest flowrate of 250cfm showed minimum and maximum values of 7.23% and 18.1%, respectively, which accounts for the greater standard deviation encountered at 250 cfm. It can be speculated that the crossover increases above 200 cfm are related to a build-up of CO_2 at the interface of the wall due to the absence of fresh air movement in this vicinity during the experiments.

Table 8: Vertical O1 Statistical Results

Flowrate (cfm)	**100**	**150**	**200**	**250**
Average (%)	6.3	7.3	8.5	13.5
Std. Dev. (%)	1.28	2.16	1.18	3.66
Std. Error (%)	0.45	0.72	0.33	1.16
Uncertainty (%)	4.49	4.56	5.13	6.03

Vertical Orientation 2 (O2)

The second vertical orientation, with 24 inches of separation, is the final vertical arrangement conducted and presented for this research as the results obtained for the third orientation (O3) are exceed the uncertainty limit of the CO_2 sensors utilized in this study.

The results for the vertical O2 setup, reveal a decreased crossover percentage when compared with O1, and are presented below in Figure 40 through Figure 43. A close linear curve fit is observed for the uncorrected crossover percentages (XO_{NA}), with slightly more deviance per test for higher flow-rates. Only seven data points were taken for 250 cfm, which is significantly less data compared to that taken at the three lower flowrates. The reason for less data is due to difficulties in maintaining a static environment during the tests which in turn caused data discontinuities or outliers as a result of the high flow-rate in conjunction with the larger intake and exhaust spacing of 24 inches. The most stable flow-rate was 150 cfm as seen in Figure 41 due to it possessing the lowest standard deviation associated with the corrected crossover percentage, which will be shown later.

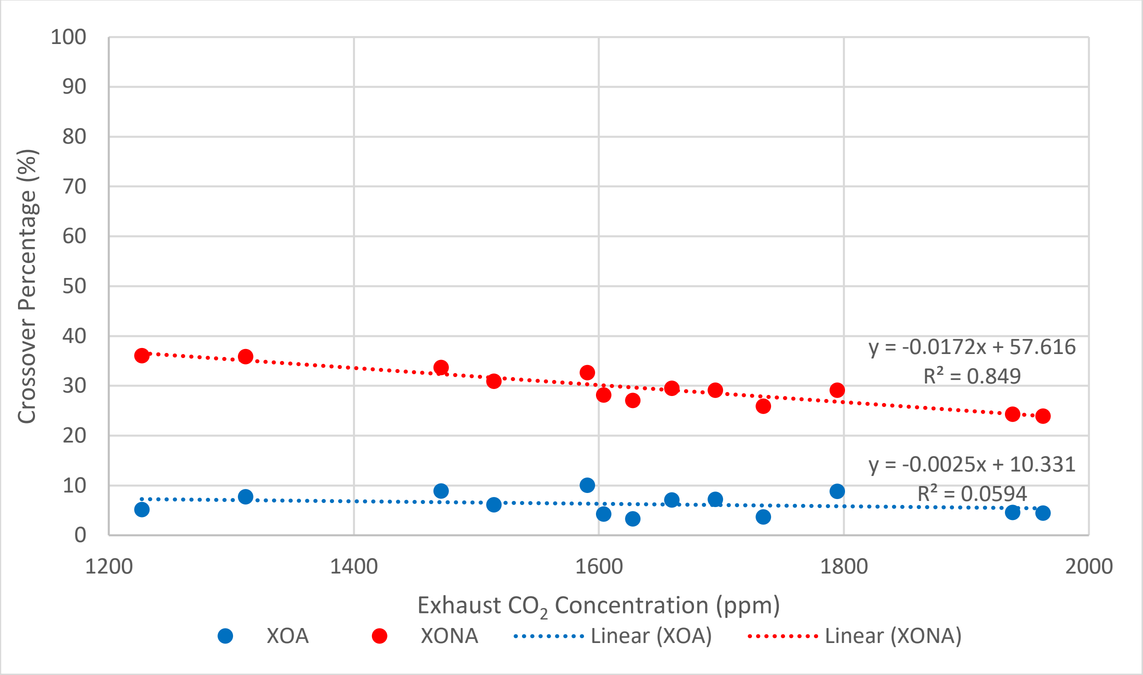

Figure 40: 100 CFM Vertical O2

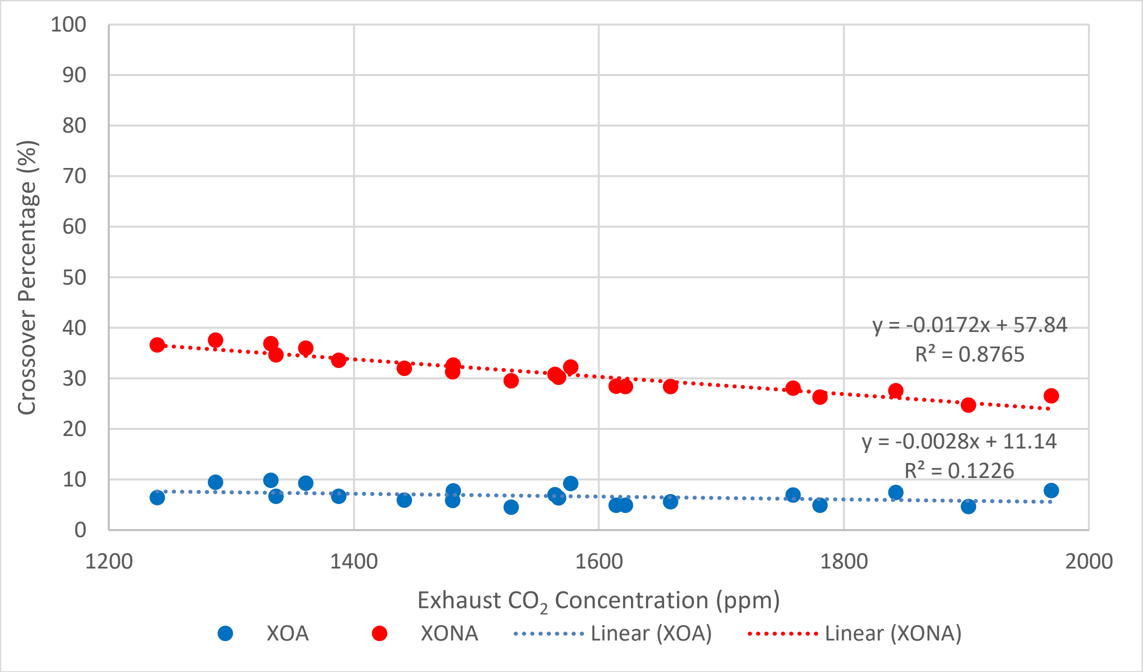

Figure 41: 150 CFM Vertical O2

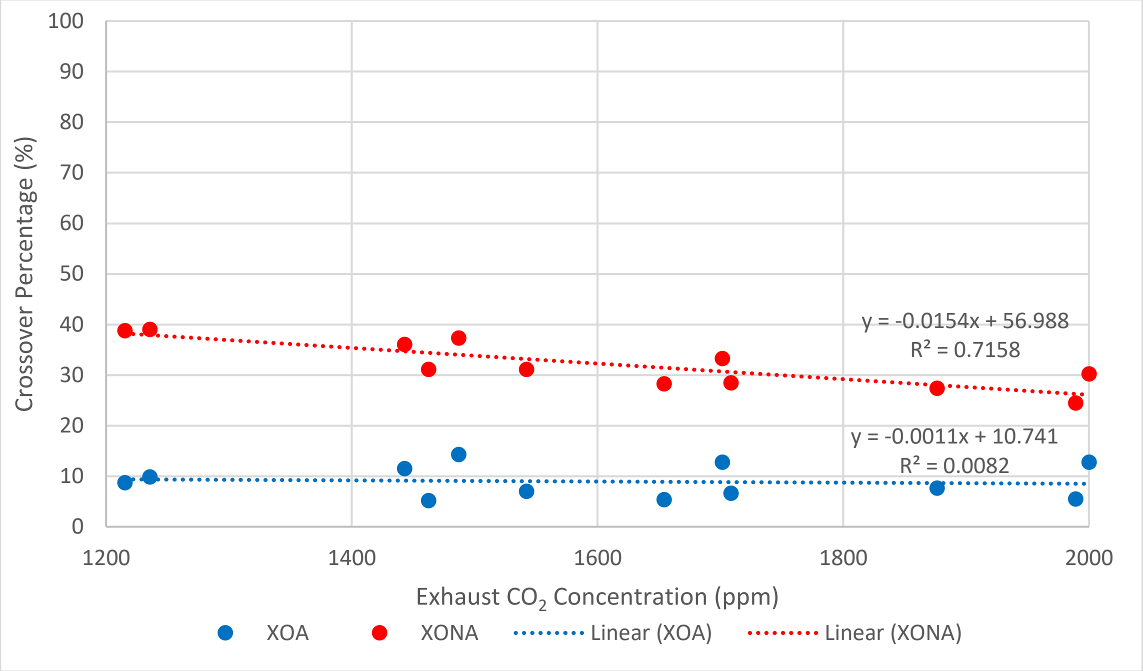

Figure 42: 200 CFM Vertical O2

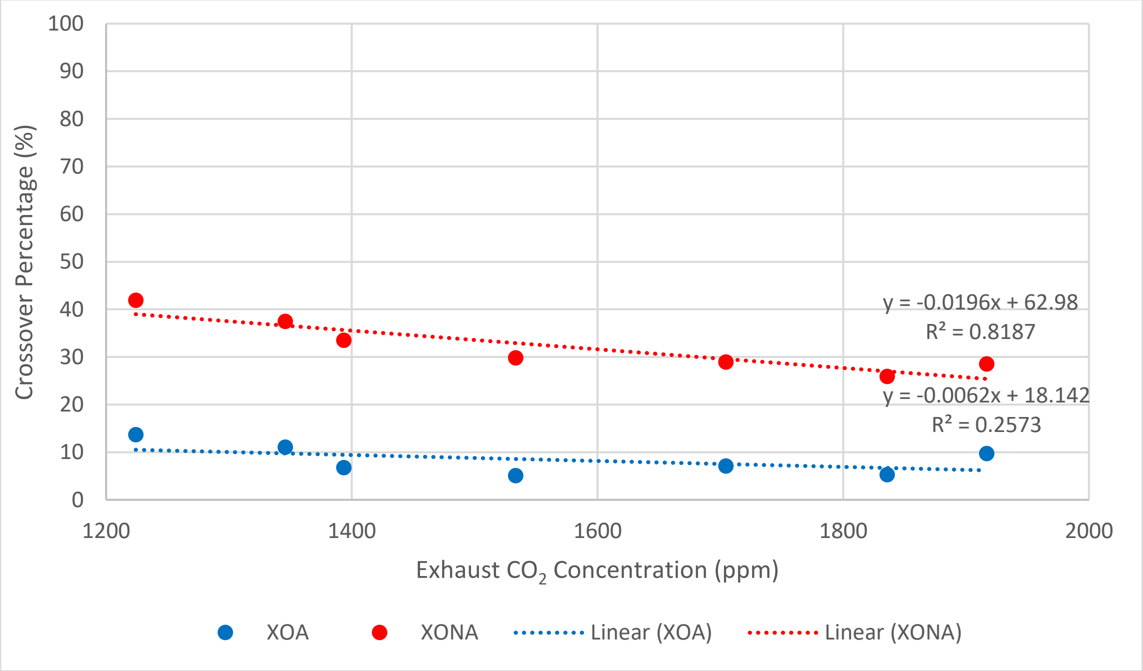

Figure 43: 250 CFM Vertical O2

Figure 44 combines the atmospherically corrected values presented in the prior four figures, for the four flowrates. It can be seen that the crossover percentage increases with respect to increasing flow-rate for this second vertical orientation (O2). The important point to be taken away from Figure 44 is that although the individual data points for a given flow-rate may be above or below the next higher or lower flow, the average as a result of many tests reveal that by increasing the flow-rate, the crossover percentage is increased as well, which is in-line with the results obtained from the first vertical orientation.

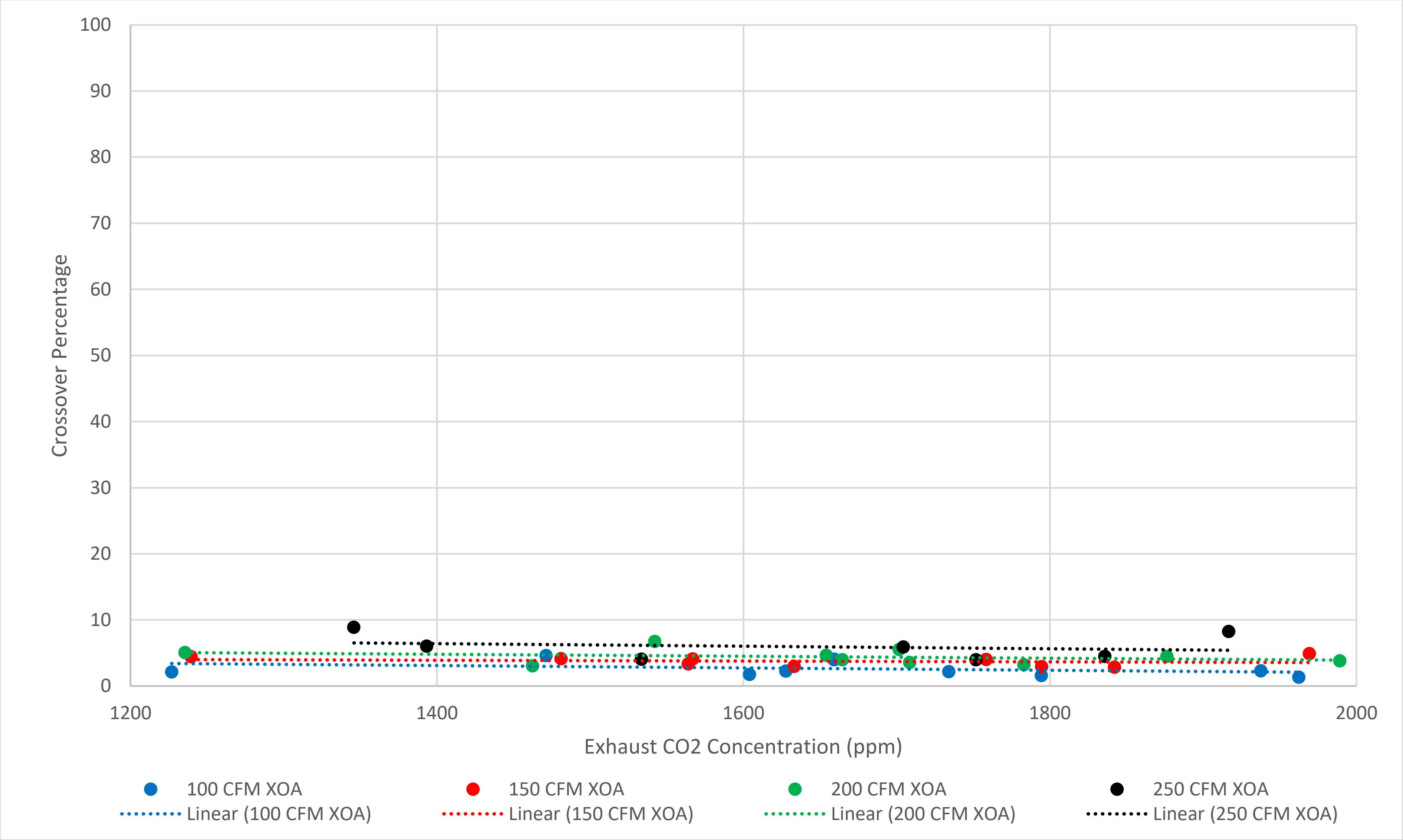

Figure 44: Flowrate Comparison: Vertical O2 – Normalized (XO$_A$)

When the four flow-rates are compared side-by side in Figure 44 the decreasing linear trend is more apparent, in other words as the exhaust CO2 concentration was increased the crossover was decreased relative to the tests performed at a lower exhaust concentration, which is similar to the 100 and 150 cfm results for the first orientation.

The statistical results for the second vertical orientation are presented in Table 9. While the second orientation did not present constant values between each flowrate, the differences are smaller to the point of being insignificant. It can be observed that between 100 and 150 cfm the average corrected crossover is between 6% and 7%, while from 200 to 250 cfm the average corrected crossover percentage lies between 8% and 9%. The largest standard deviation and standard error corresponds to the highest flow-rates of 200 and 250 cfm. It is important to note that the uncertainties for all of the volumetric flow rates are essentially equivalent with only a 0.4% difference between the smallest (4.6%) and the largest (5%) uncertainty. It is possible that this trend could continue for further increases in flow-rate above 250 cfm due to the turbulent, random effects of the exhaust air at the interface of the wall.

Table 9: Vertical O2 Statistical Results

Flowrate (cfm)	**100**	**150**	**200**	**250**
Average XO_A (%)	6.26	6.75	8.92	8.38
Std. Dev. (%)	2.21	1.65	3.21	3.22
Std. Error (%)	0.61	0.37	0.93	1.22
Uncertainty (%)	4.59	4.85	4.64	4.97

Vertical Comparisons and Conclusions

Because only two orientations were examined for the vertical arrangement, the relative change between the orientations is more difficult to analyze and to draw conclusions from; however; in general, negligible changes were observed from 100 through 200 cfm were documented, even when the spacing between the intake and exhaust is increased from 12” (O1) to 24” (O2). Decreases of approximately 0%, 0.5%, and 5% for 100, 150, and 250 cfm, respectively, were observed with increase in spacing from O1 to O2, along with a marginal increase of 0.4% for 200 cfm.

The side-by-side comparison for these two orientations, along with the error bars representing the uncertainty, are depicted in Figure 45. Figure 45 shows that the mixing phenomena for the vertical arrangement is fairly equal up to 200 cfm, with the only significant decline being about 5%, and occurring at 250 cfm, which was noted previously. Because of the uncertainties in the physical measurements, it is important to note that the results presented for the vertical arrangement have a large amount of uncertainty relative to the calculated corrected crossover percentage (XO_A); however, as the calculated crossover increases, the results become more robust as the lower limit of the uncertainty bars do not dip near zero.

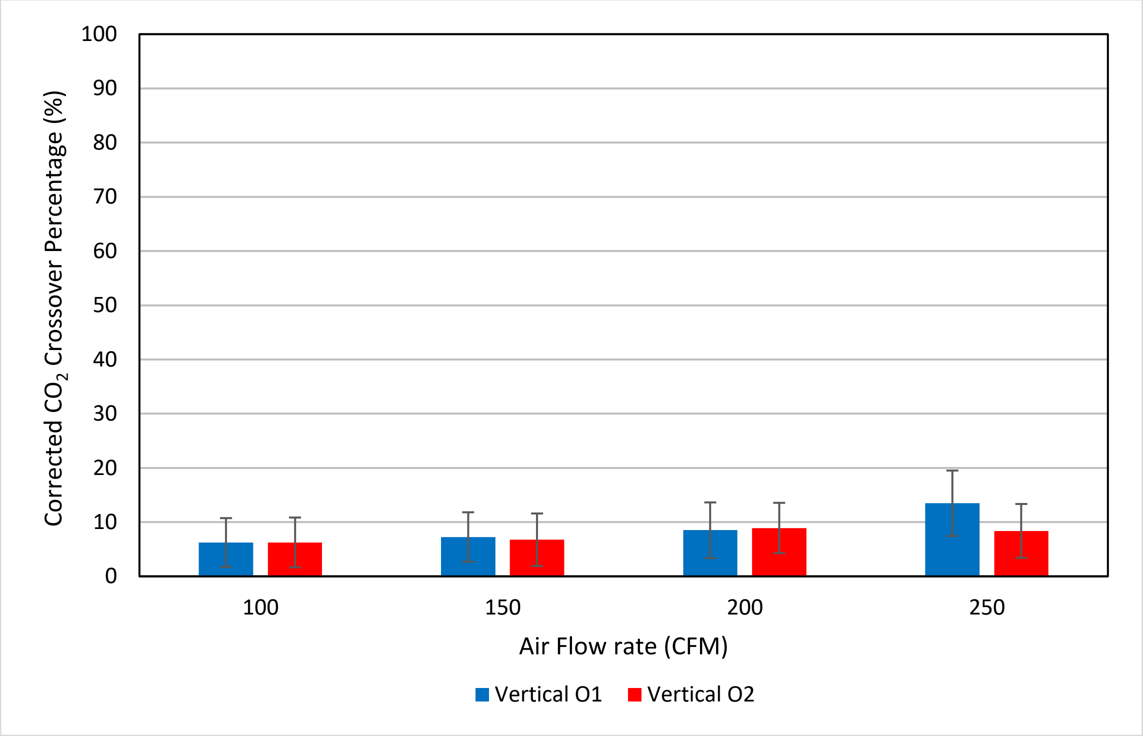

Figure 45: Vertical CO2 Crossover Percentage vs. Flow Rate

CHAPTER VII

HORIZONTAL ARRANGEMENT EXPERIMENTS

The third and final experimental arrangement is the horizontal arrangement, where the exhaust and intake ventilation grills are repositioned horizontally and in-line with each other, in lieu of the vertical in-line arrangements as presented earlier in Chapters VI and VII. This new adjustment allows the intake and exhaust to have the same vertical height for the three different intake and exhaust spacing's while maintaining the same distances and nomenclature as the previous two arrangements, namely vertical and inverse vertical. In other words, the horizontal spacing's for the first orientation (O1) is 12 inches, 24 inches for the second (O2), and 48 inches for the third and final horizontal orientation (O3). Visuals of these three horizontal experimental setups showing the different spacing's are shown in Figure 46 through Figure 48 for O1, O2, and O3, respectively. Similar to the vertical arrangement, the ventilation grills can be adjusted to the appropriate distance for each experimental setup with the unused holes being sealed with masking tape as shown in the previous figures.

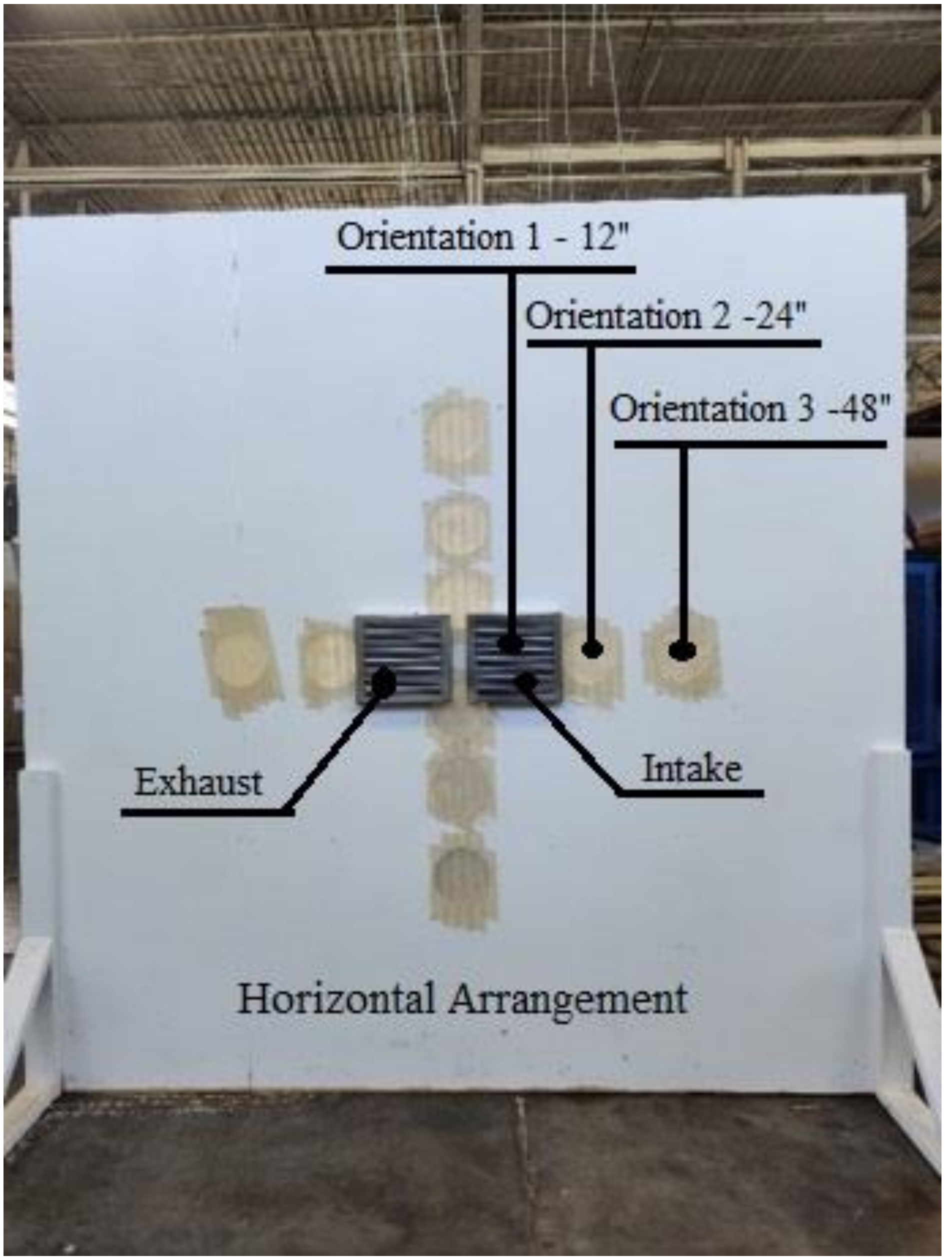

Figure 46: Horizontal Orientation 1 (O1)

Figure 47: Horizontal Orientation 2 (O2)

Figure 48: Horizontal Orientation 3 (O3)

Horizontal Orientation 1 (O1)

The first horizontal arrangement to be tested and evaluated utilizes the same procedure that was used for the previous O1vertical setups, namely by placing the ventilation grills so that they are 12” apart (6” center to center). A total of nine tests were performed for each flow-rate resulting in 36 unique tests. The results of these tests can be seen below in Figure 49 through Figure 52. It should be noted that Figure 49 and Figure 52 are all scaled to a maximum of 100 percent on the y-axis to maintain uniformity with the previous arrangements and orientations. Additionally, it can be observed that the two lowest flow-rates of 100 and 150 cfm have a reduced exhaust CO_2 concentration range of 1200 to 2000 pm in lieu of the typical 1000 to 2000ppm, as the fine control required to encompass exhaust concentrations down to 1000 ppm was difficult to achieve for the lower flow rates. With the two higher flow rates less fine control was required and thus a more robust range is observed. In addition, 13 tests were conducted at 200 cfm instead of the standard 9 for the other three flow rates, as the additional 4 tests were required to fully define the curve.

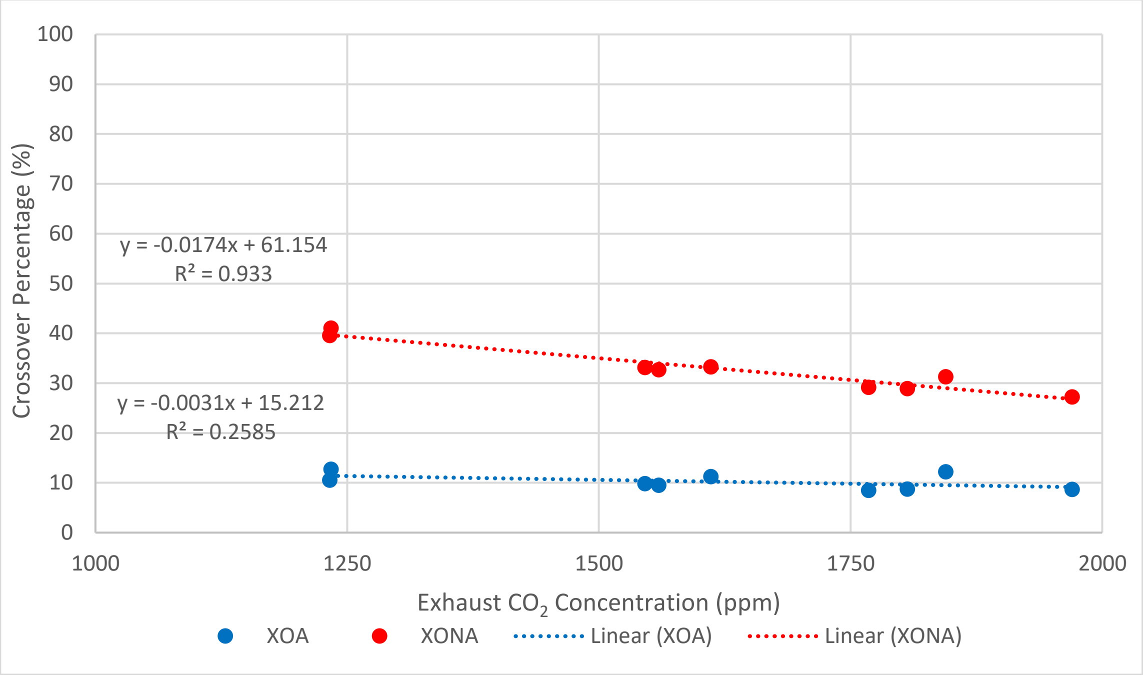

Figure 49: 100 CFM Horizontal O1

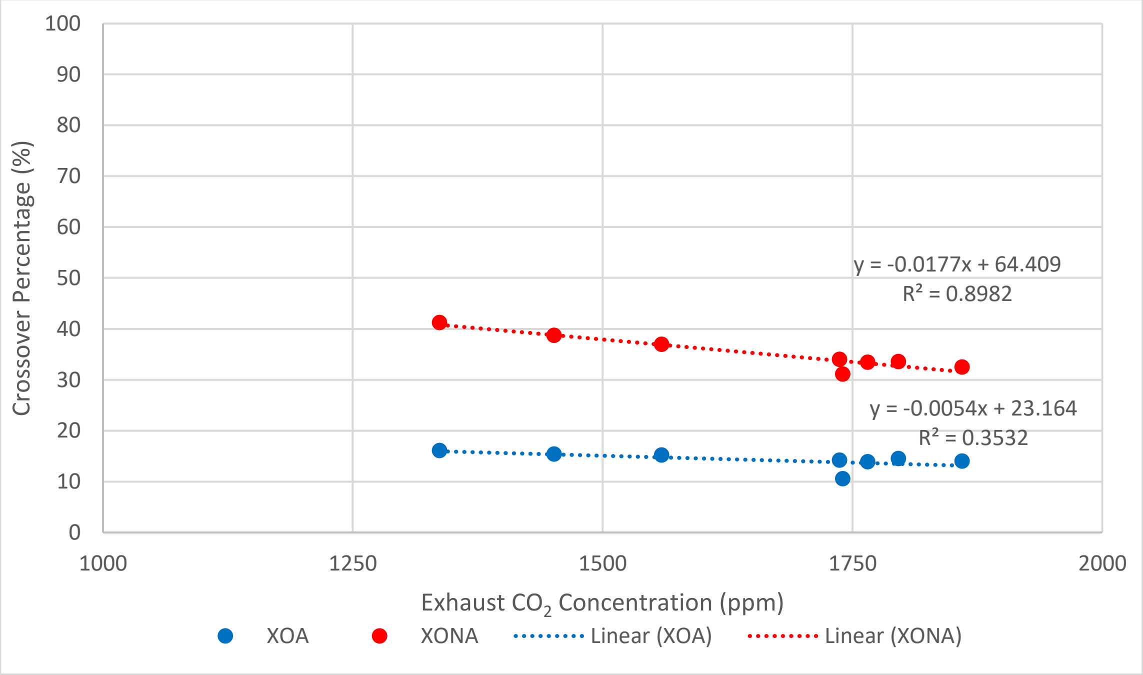

Figure 50: 150 CFM Horizontal O1

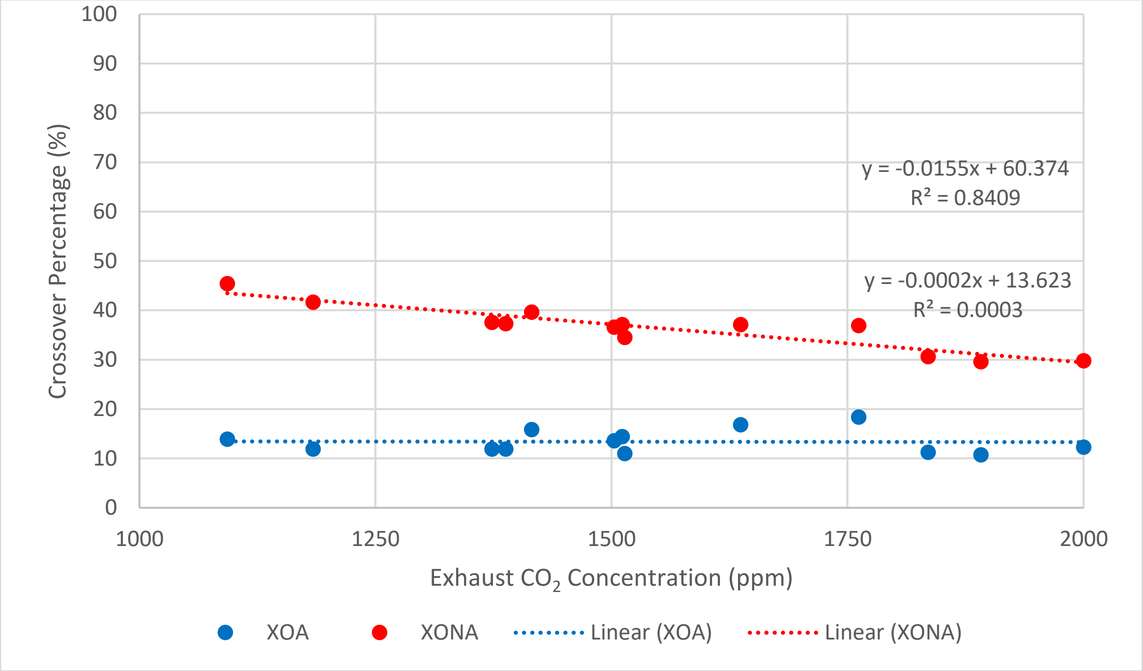

Figure 51: 200 CFM Horizontal O1

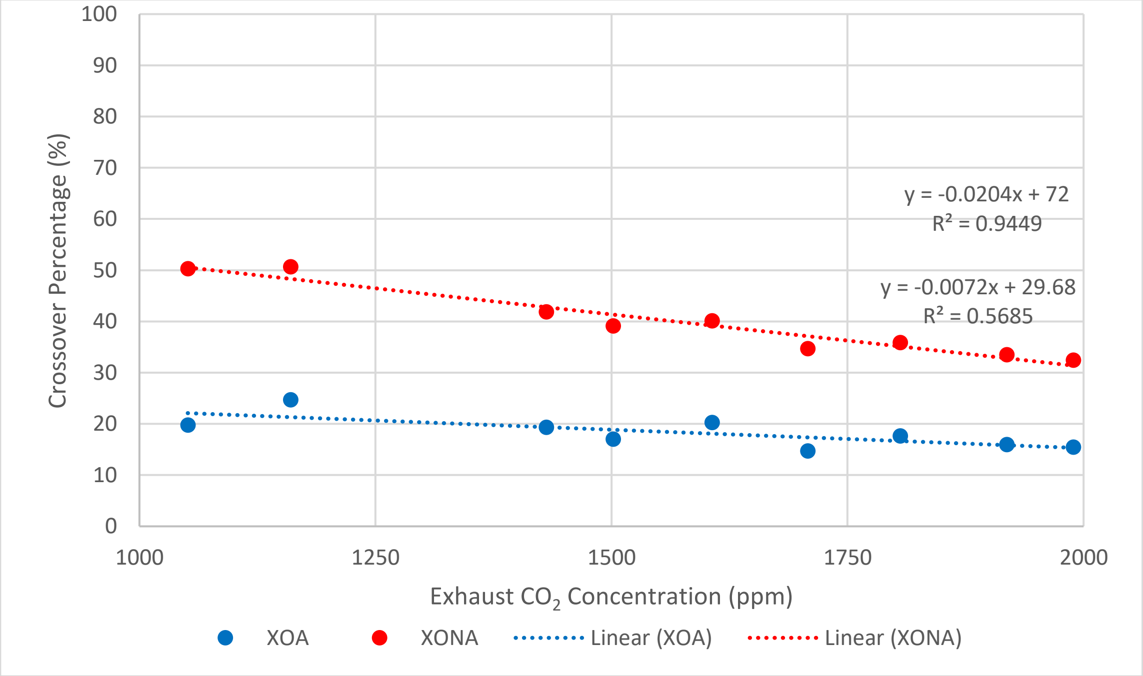

Figure 52: 250 CFM Horizontal O1

The horizontal O1 experiments resulted in steady mixing increases as the flow-rate was increased, with a difference of 8% corrected crossover (XO_A) from 100 to 250 cfm. Uncorrected crossover values (XO_{NA}) once again show a strong downward linear trend for all cases, with linear slopes of up to -0.02 and a respective R-squared value of 0.95 for 250 cfm. In general, the corrected crossover values (XO_A) have linear slopes approximately an order of magnitude less, from -0.007 to -0.0002 as seen in Figure 52, which while still resulting in a slight downward linear trend, eliminates the majority of atmospheric CO_2 related impacts on the crossover percentage at lower exhaust concentrations for the uncorrected values.

The atmospherically corrected crossover percentages for the prior four figures were plotted together and the y-axis adjusted to provide greater clarity as seen in Figure 53. Figure 53 shows a combined scatter plot of the corrected crossover (XO_A) versus exhaust CO_2 concentration for 100 to 250 cfm in an effort to allow greater insight into the trends at each flow-rate. By conducting experiments across a wide range of exhaust CO2 concentrations, the exhaust-to-intake mixing is characterized more thoroughly than multiple experiments at a single static exhaust concentration.

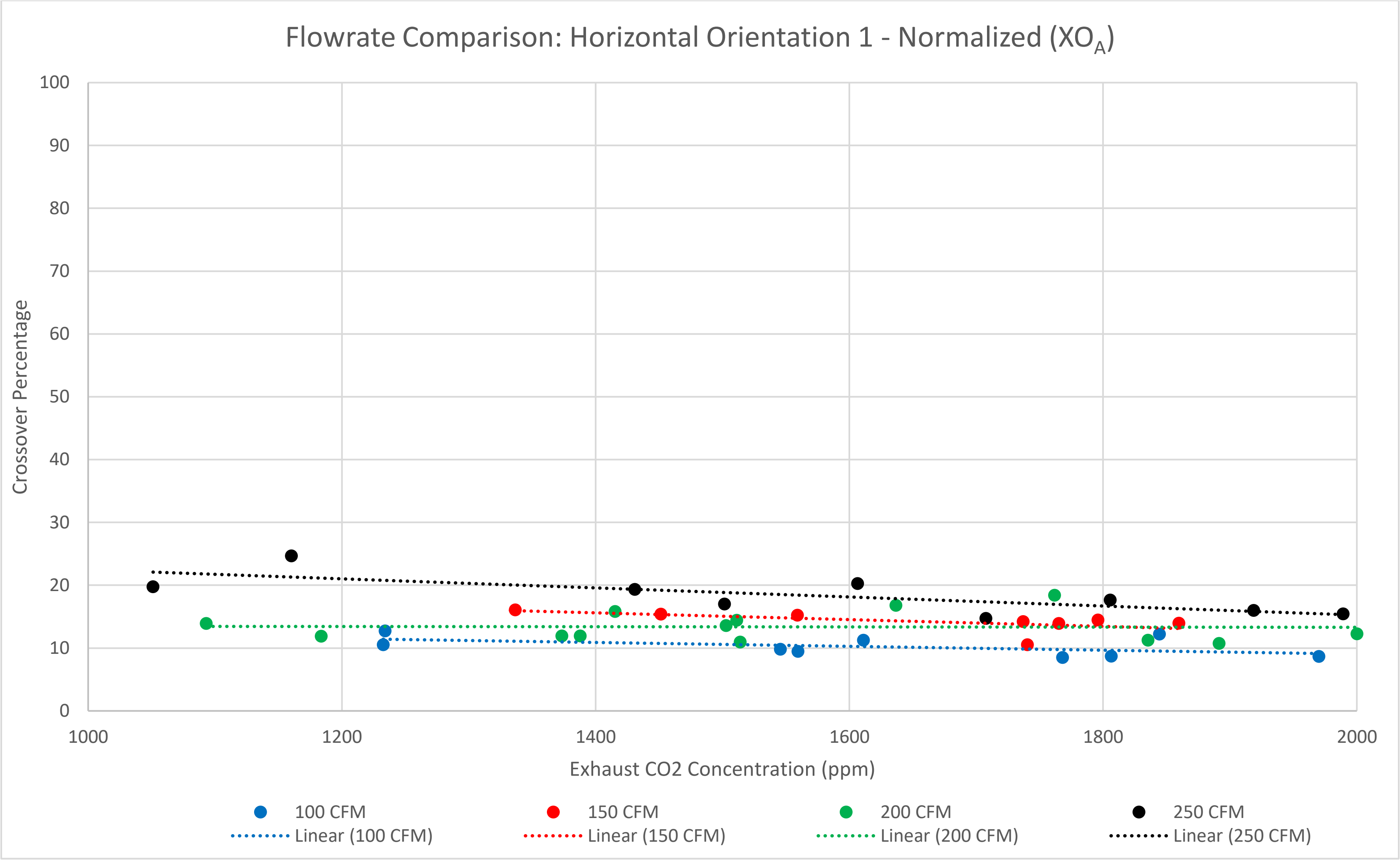

Figure 53: Horizontal O1 Flowrate Comparison

The statistical evaluation for the horizontal O1 setup and test data are tabulated in Table 10. Table 11 highlights that 150 and 200 cfm have approximately the same crossover percentages (less than 1% difference), with the main increases occurring from 100 to 150 cfm and 150 or 200 to 250 cfm representing an approximate increase of 4% each. Standard deviation, standard error, and the uncertainty all trend upwards as the flow rate is increased, with the standard deviation of 250 cfm being twice that of 100 cfm; however, only a marginal uptick in uncertainty from 4.8% to 5.6% is witnessed.

Table 10: Horizontal O1 Statistical Results

Flowrate (cfm)	**100**	**150**	**200**	**250**
Average XO_A (%)	10.22	14.23	13.38	18.32
Std. Dev. (%)	1.57	1.68	2.4	3.09
Std. Error (%)	0.52	0.59	0.67	1.03
Uncertainty (%)	4.84	4.94	5.30	5.56

Horizontal Orientation 2 (O2)

The second horizontal orientation increases the center-to-center distance of the intake and exhaust by 12 inches, for a total of 24 inches of separation. This effectively doubles the intake and exhaust spacing from the first orientation, however; contrary to the vertical orientations there are not substantial decreases noted, nor large deviances between the flow-rates. Rather, the corrected crossover percentage (XO_A) for the second horizontal orientation is fairly constant regardless of the volume of air exhausted. Figure 54 through Figure 57 detail the experiments conducted for 100 through 250 cfm, respectively.

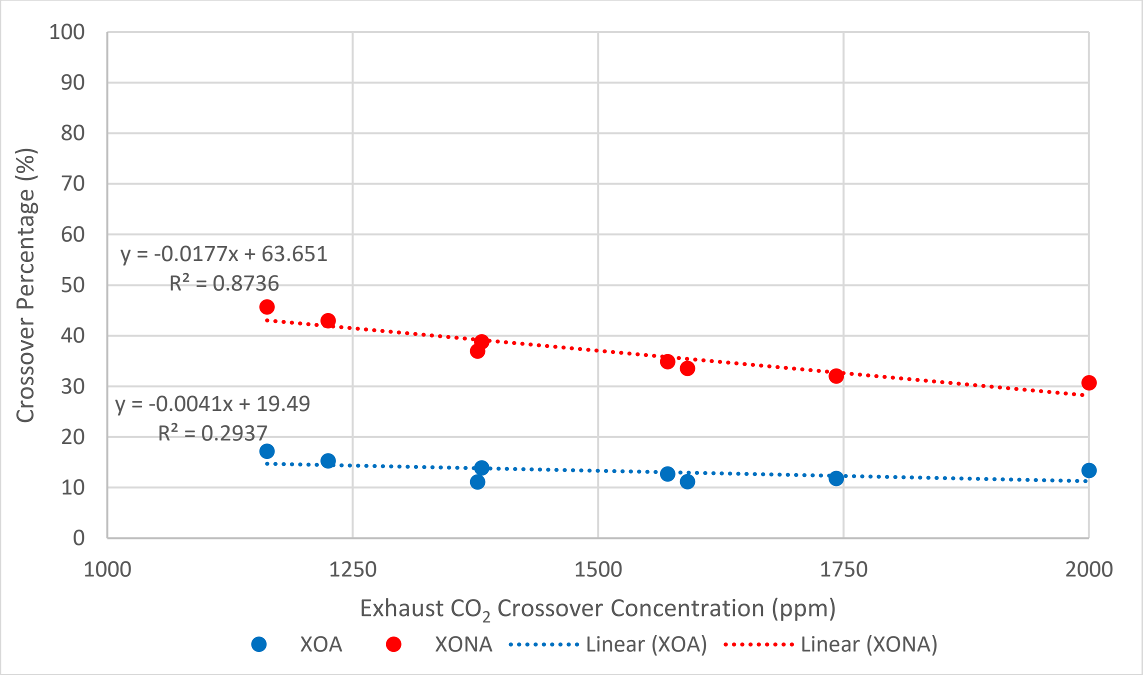

Figure 54: 100 CFM Horizontal O2

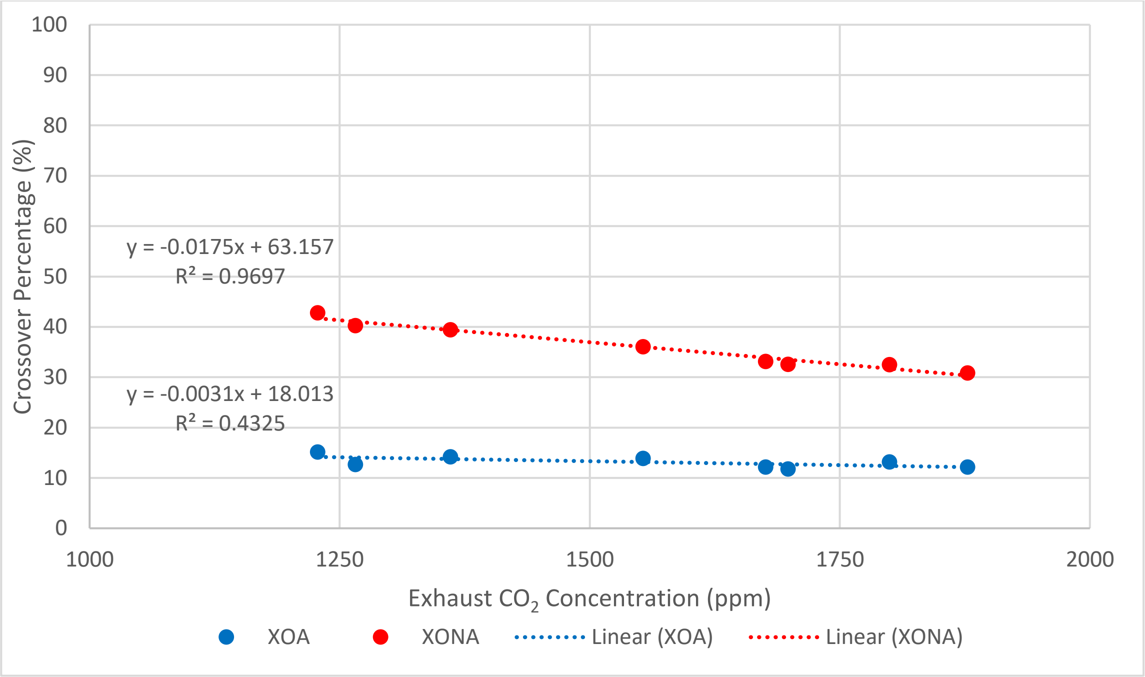

Figure 55: 150 CFM Horizontal O2

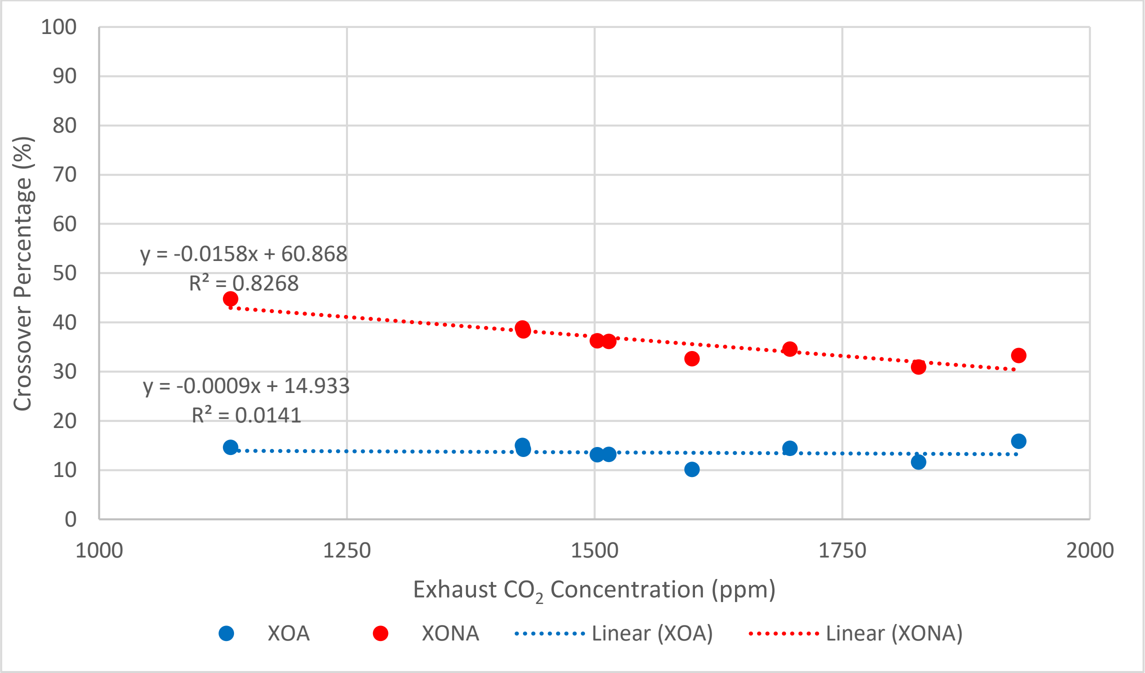

Figure 56: 200 CFM Horizontal O2

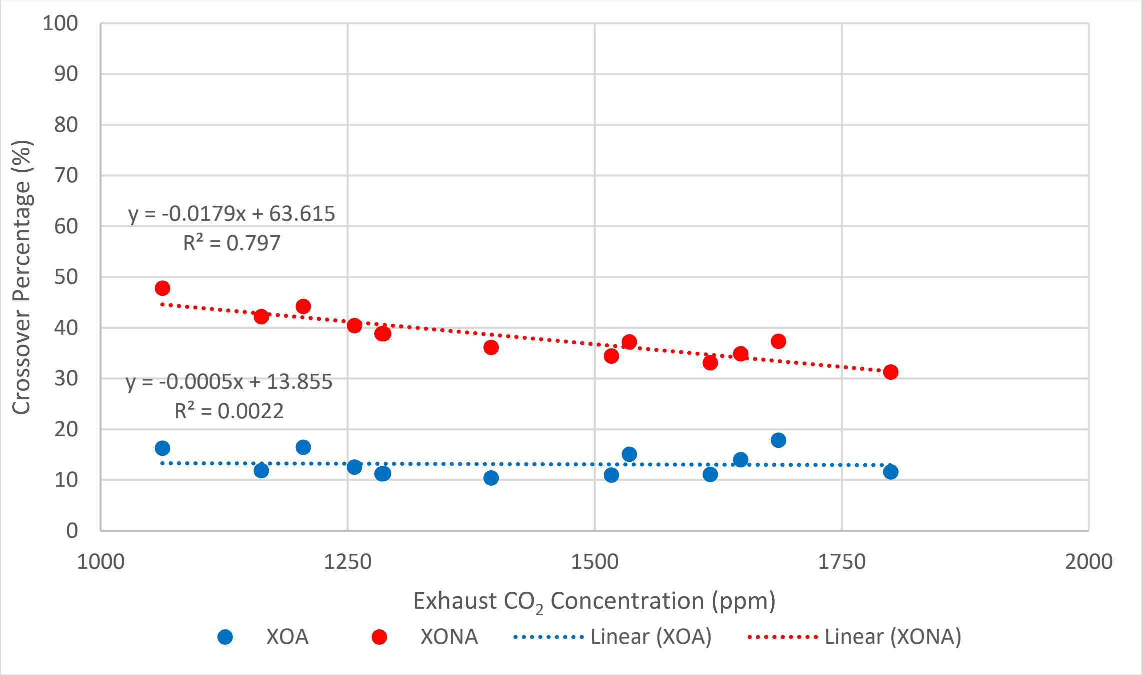

Figure 57: 250 CFM Horizontal O2

The four previous figures possess the same scaling on both the x and y-axis, from 1000 to 2000ppm. Because of this, the subtle increases between each flow-rate can be identified as well as the overall flat linear trend across the exhaust CO_2 concentration range of 1000 to 2000ppm. The lower two flow rates have similar slopes (-0.0041 and -0.0031) while the higher two flow rates also share similar slopes (-0.0009 and -0.0005) which corresponds to deviance in the corrected crossover percentage of 0.9 and 0.5 percent across the exhaust CO_2 range. Once again uncorrected values (XO_{NA}) revealed stronger downward linear trends than corrected values, which has been consistent throughout all experimental setups, orientations, and flow-rates. The atmospherically CO_2 corrected crossover results for the second horizontal orientation are combined in Figure 58.

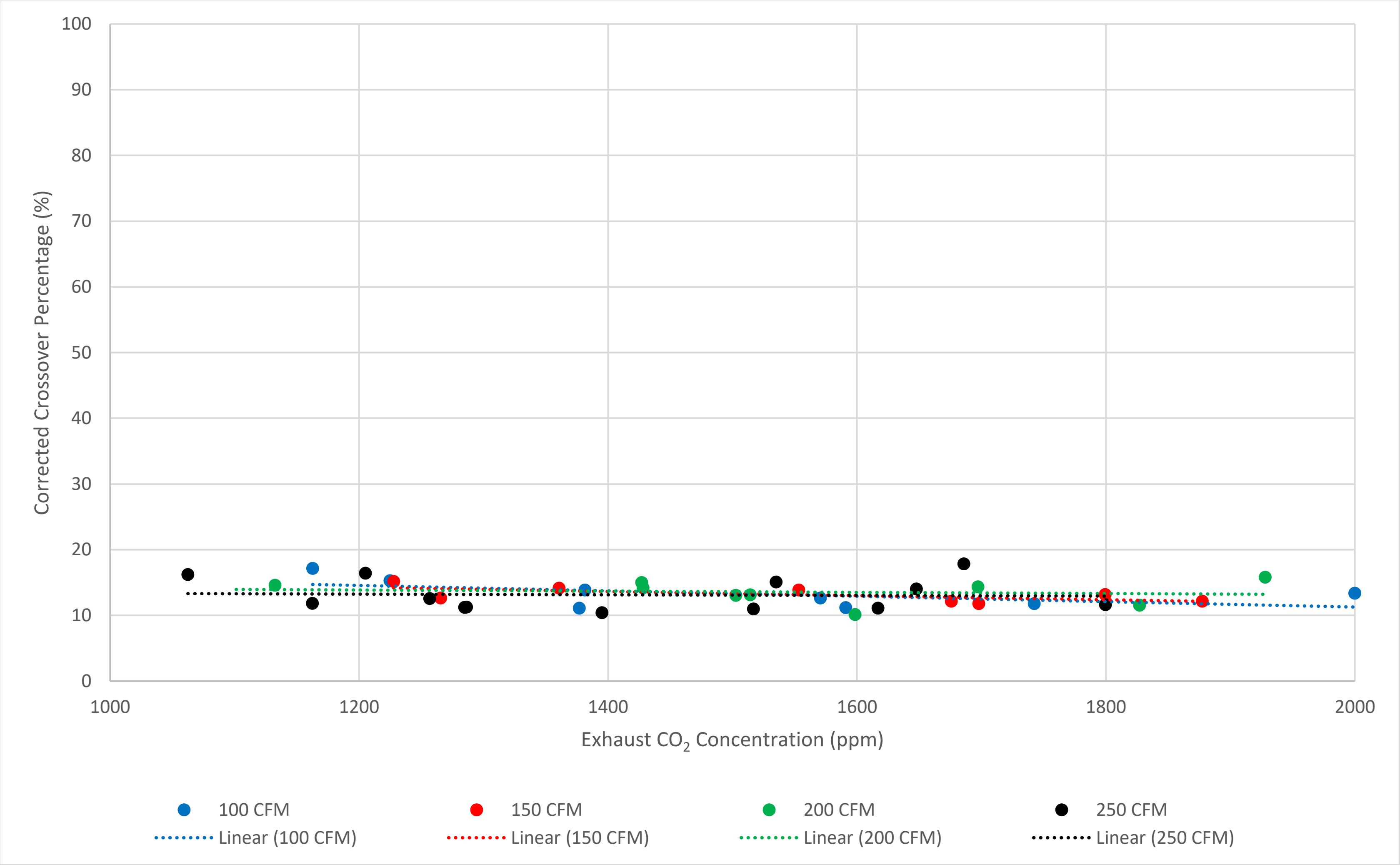

Figure 58: Horizontal O2 Flowrate Comparison – Normalized (XO_A)

Figure 58 highlights the corrected exhaust-to-intake CO_2 crossover is fairly constant regardless of the volumetric flow rate with no appreciable differences readily apparent for the horizontal O2 arrangement. The flow rate of 100 cfm reported the largest gap between the highest and lowest calculated crossover of 17.2 and 11.1 percent, respectively for total gap of 6.1 percent while the other three flow-rates had maximum and minimums approximately 4 percent apart. Table 11 expounds on this with the statistical analysis of the results.

Table 11: Horizontal O2 Statistical Results

Flowrate (cfm)	**100**	**150**	**200**	**250**
Average XO_A (%)	13.3	13.14	13.54	13.13
Std. Dev. (%)	2.1	1.17	1.78	2.49
Std. Error (%)	0.74	0.42	0.59	0.69
Uncertainty (%)	5.46	5.19	5.18	5.85

Table 11 further solidifies that there is a negligible increase or decrease in corrected CO_2 crossover (XO_A) when the volumetric flow rate is more than doubled, and it can be concluded that for a 24” intake and exhaust spacing in the horizontal configuration marginal increases in exhaust mixing can be expected up to 250 cfm. It should also be noted that the standard deviation, as well as the uncertainties for the second horizontal orientation are similar to the first, in that the standard deviation increases from 2.1% to 2.5%, while the uncertainties only slightly rise from 5.5% to 5.9% for the range of 100 to 250 cfm, respectively. It is expected for the standard deviation to rise as the volumetric flow rate is increased due to the greater amount of air exhausted and the unpredictable effects of the turbulent exhaust air interacting with the ambient environment.

Horizontal Orientation 3 (O3)

The final arrangement and orientation studied during the course of this research for exhaust and intake carbon dioxide crossover is the third horizontal orientation. This orientation has a horizontal center-to-center distance of 48 inches, or double the distance of the second orientation and four times the distance of the first orientation. A visual of this setup can be referenced in Figure 48, which was presented previously. A total of 8 tests were conducted per flow-rate resulting in 32 unique data points. Similar to the first two horizontal orientations, the widest spacing of 48” revealed more-or-less constant mixing. The results of the experiments for the third orientation can be seen in Figure 59 through Figure 62.

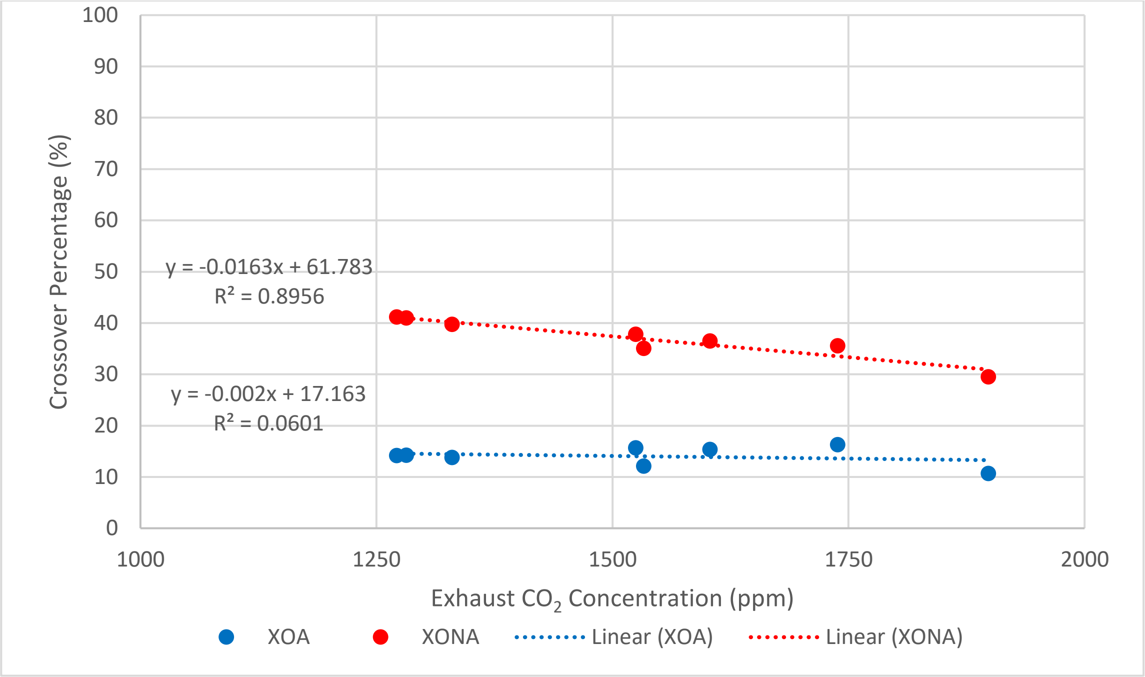

Figure 59: 100 CFM Horizontal O3

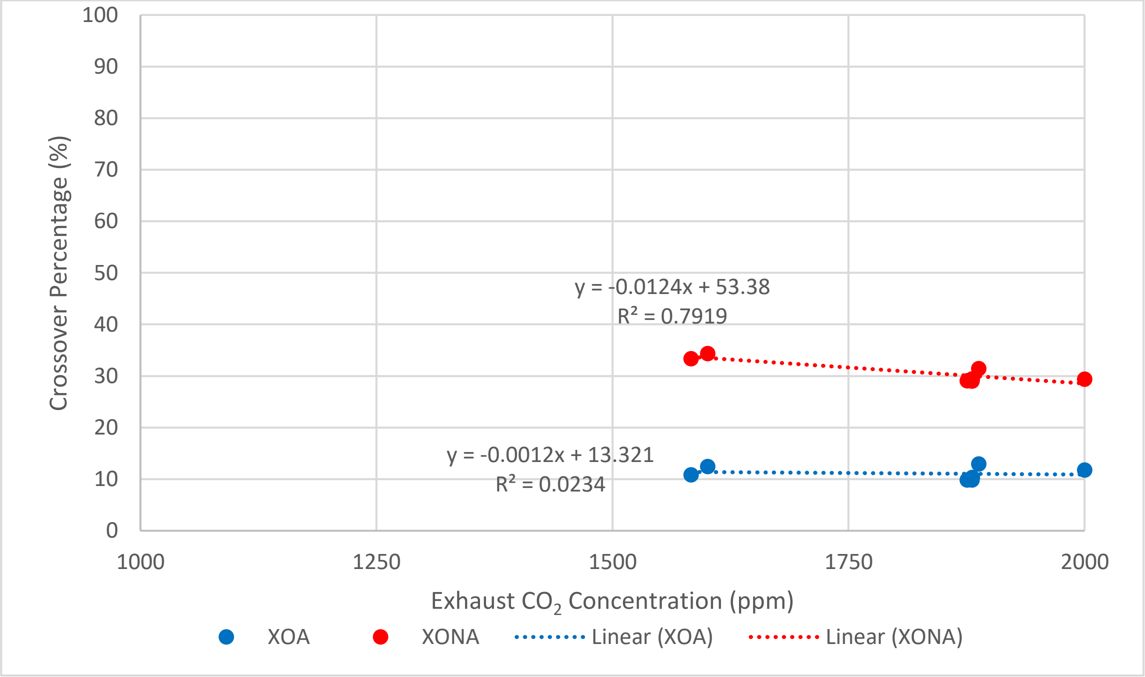

Figure 60: 150 CFM Horizontal O3

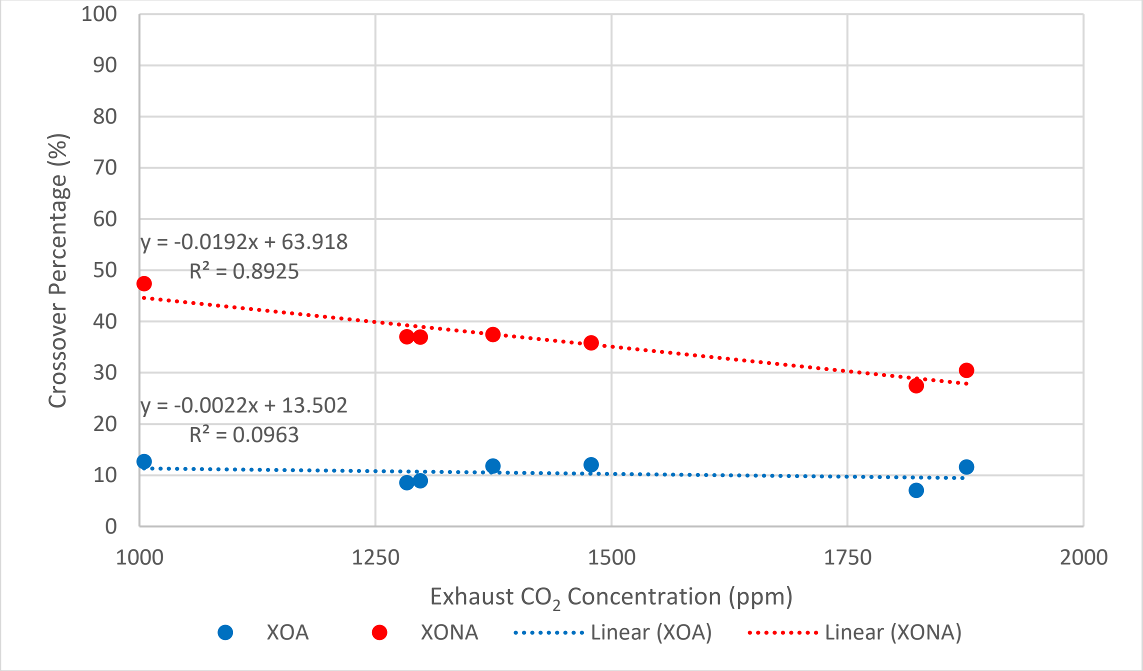

Figure 61: 200 CFM Horizontal O3

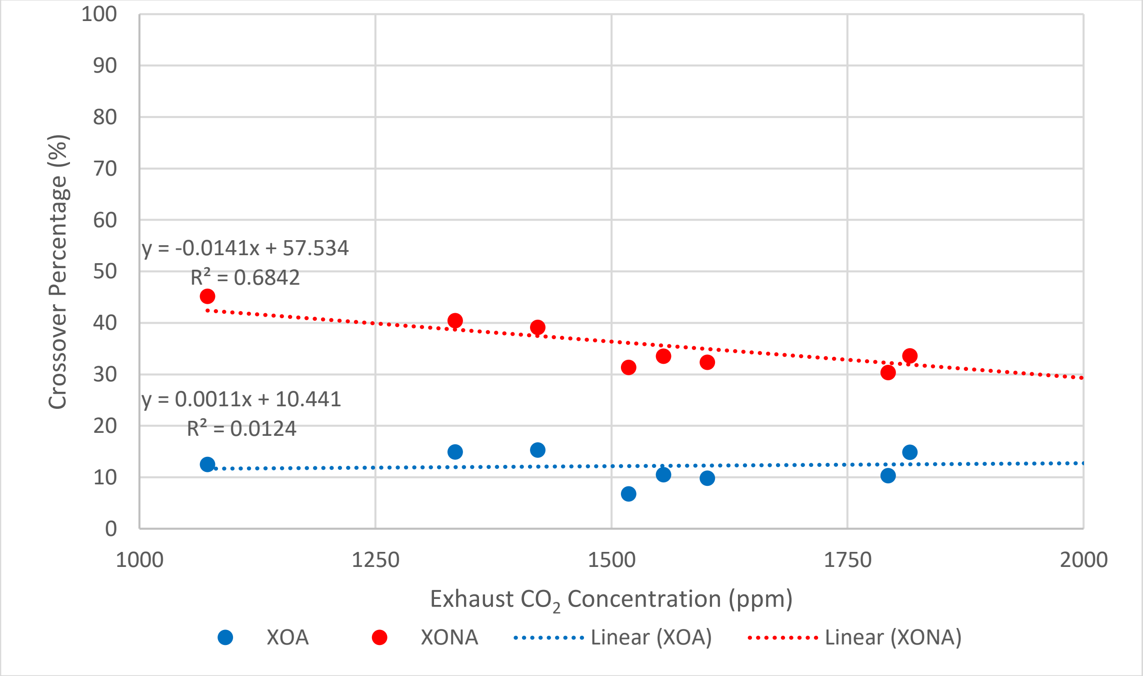

Figure 62: 250 CFM Horizontal O3

The four volumetric flowrates again revealed a linear decline for both the uncorrected (XO_{NA}) and corrected (XO_A) intake-to-exhaust mixing as the exhaust carbon dioxide concentration was increased, while the corrected values had a minor linear slope associated with them (0.0011 for 250 cfm). Another point of interest concerning the above four figures is the repeatability witnessed. There are several instances, namely in Figure 59 and Figure 60, where tests are conducted at very similar exhaust CO_2 concentrations, resulting in similar calculated crossover percentages. For example, at 100 cfm two experiments were conducted with exhaust concentrations of 1271 and 1282 ppm resulting in corrected crossovers of 14.17 and 14.24 percent. The ambient carbon dioxide corrected results are presented in greater detail in Figure 63.

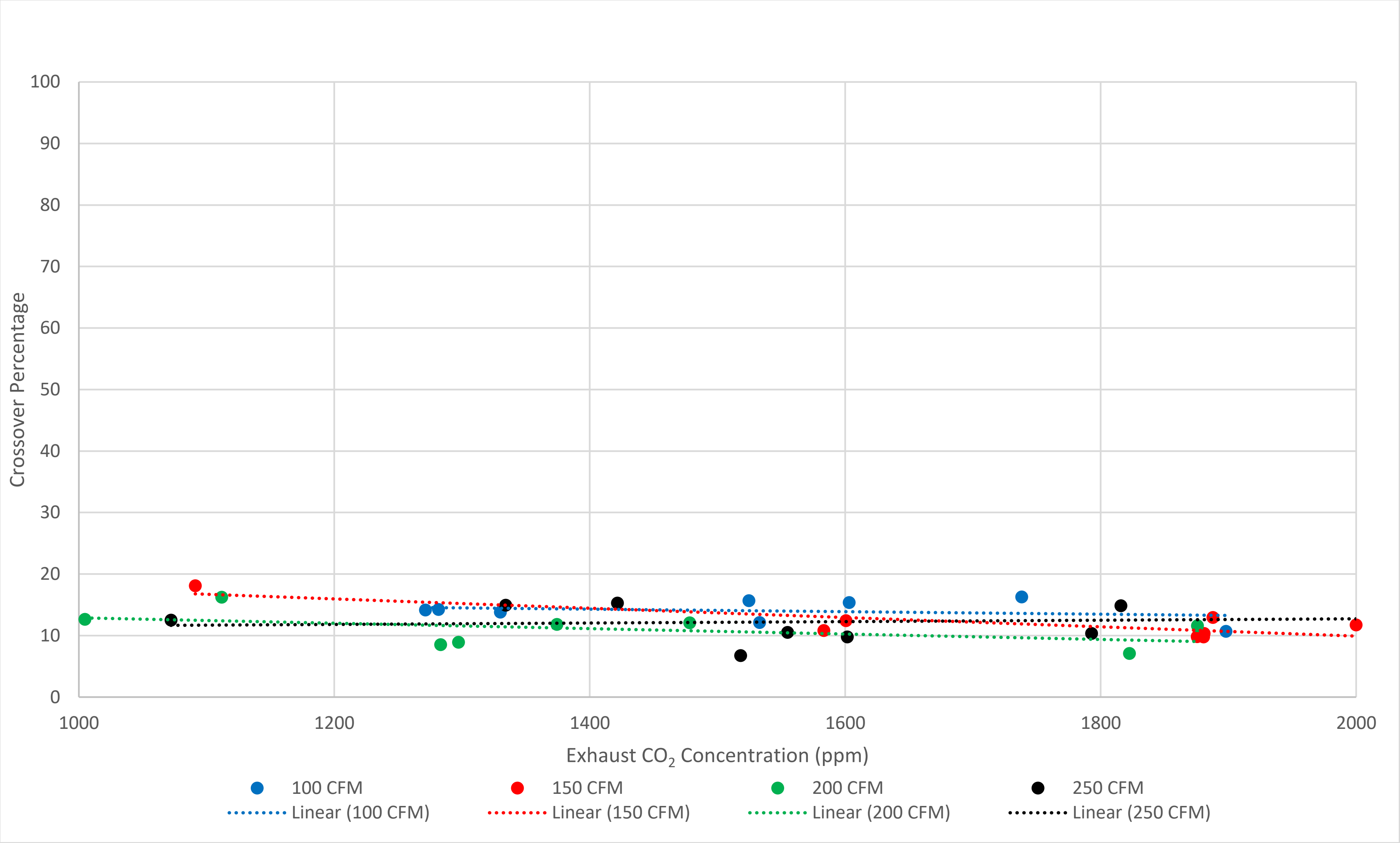

Figure 63: Horizontal O3 Flowrate Comparison – Normalized (XOA)

There are two main takeaways from Figure 63. Firstly, because the four flowrates have similar slopes associated with them, namely between -0.002 and 0.001 for 100 and 250 cfm, respectively, minor increases or decreases in the corrected crossover percentage across the exhaust range of 1000 to 2000ppm are observed. The second takeaway from the above figure concerns the expected mixing at a given flow rate. Given the proximity of results to one another, it is expected for a horizontal exhaust and intake arrangement with a separation of 48" or greater to result in a mixing between 10% and 15% for flowrates up to 250 cfm. The relation of the volumetric flowrates to each other can be seen in Table 12.

Table 12: Horizontal O3 Statistical Results

Flowrate (cfm)	**100**	**150**	**200**	**250**
Average XO_A (%)	14.04	11.99	11.1	12.24
Std. Dev. (%)	1.88	2.73	2.88	2.03
Std. Error (%)	0.66	0.97	1.02	0.54
Uncertainty (%)	5.33	4.64	6.03	5.16

Table 12 highlights the deviance noted previously for the 100 cfm experiment, and with this exception, it be seen the increase from 150 to 250 cfm is a marginal 0.25% rise. Because of the larger 48" spacing between the intake and exhaust, the average corrected crossover (XO_A) is less predictable through the flow rate range of 100 to 250 cfm. This being said, the uncertainty for O3 is still in-line with O1 and O2, with an average uncertainty of 5.3% and a total uncertainty range across the four flowrates of 1.4% from 4.6% to 6.0%

Horizontal Comparisons and Conclusions

A key takeaway after compiling the results from the horizontal experiments is the horizontal arrangement behaves similar to the vertical and inverse vertical arrangements. That is to say, mixing is decreased as separation is increased while mixing is increased as flow rate is increased, with the main difference of the horizontal setup being that there is less volatility between the flow-rates.

Figure 64 provides a bar chart for the comparison between each horizontal orientation, namely O1 through O3, for each of the four volumetric flow rates tested. Figure 64 allows ease of comparison between the volumetric flow rates at each orientation, with the first orientation (O1) being the leftmost column and the third orientation (O3) being the rightmost column. Three of the flowrates, namely 150, 200, and 250 cfm, show similar trends where the corrected CO_2 crossover percentage decreases as the intake and exhaust spacing increases, i.e O1 to O3, whereas at 100 cfm the opposite effect is observed with mixing increasing slightly from O1 to O3. The flowrate of 250 cfm has the largest gap between O1 and O3, showing a maximum of 18.3% and a minimum of 12.2%, respectively, for a total gap of 6.1%.

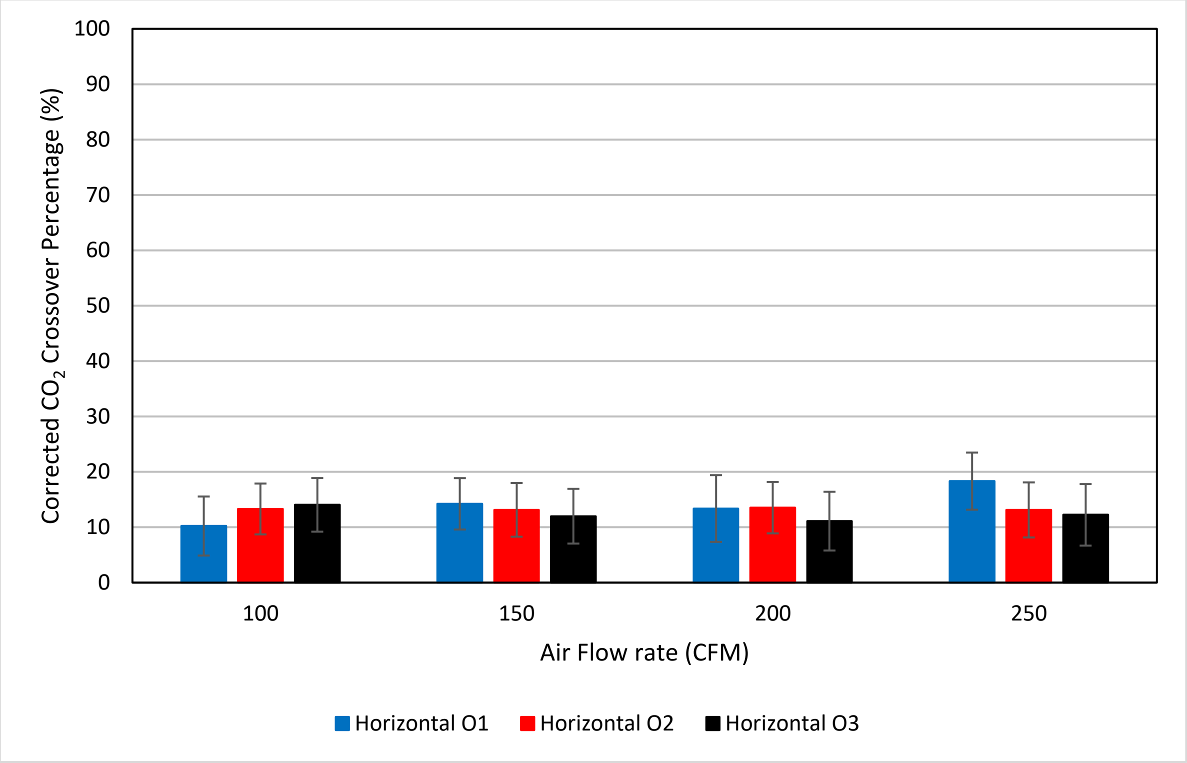

Figure 64: Horizontal Crossover Percentage vs. Flow Rate

Table 13 highlights the relative change for each flow-rate at a given orientation with respect to the previous orientation. In the horizontal orientation the relative change from O1 to O2 is significantly more than from O1 to O2 for both 100 and 250 cfm which can be attributed to the increase in distance. Because the separation for the third orientation is double the increase from O1 to O2, the expectation would be to see a larger relative change from O2 to O3 than from O1 to O2, however; this is not the case, and similar to the inverse vertical arrangement a smaller relative decrease is observed for O2 to O3, even with the distance being doubled.

Table 13: Horizontal Relative Change

Flowrate (cfm)	**100**	**150**	**200**	**250**
O1 to O2	30.1	-7.7	1.2	-28.3
O2 to O3	5.6	-8.8	-18.0	-6.8

The data for the horizontal arrangement is presented a different way in Figure 65, with the intake and exhaust spacing on the x-axis with lines of best fit applied to help visualize how the corrected crossover percentage changes as the horizontal spacing between the ducts is increased. Figure 66 assists in visualizing how the corrected crossover reacts from the first orientation (O1) to the second orientation (O2), and finally to the third orientation (O3) as it can be seen the distance is doubled from 12” to 24” and then from 24” to 48”.

A second order polynomial line fits the four flow rates nicely, showing a leveling effect for both 100 and 250 cfm at 48” of separation, while 150 and 200 cfm still require additional distance to stabilize. It should be noted that the corrected crossover percentages (XOA) for the four flow rates are within 4% of each other at 48% separation, whereas for the inverse vertical arrangement the four flow rates were within 10% of each other at 48” of spacing.

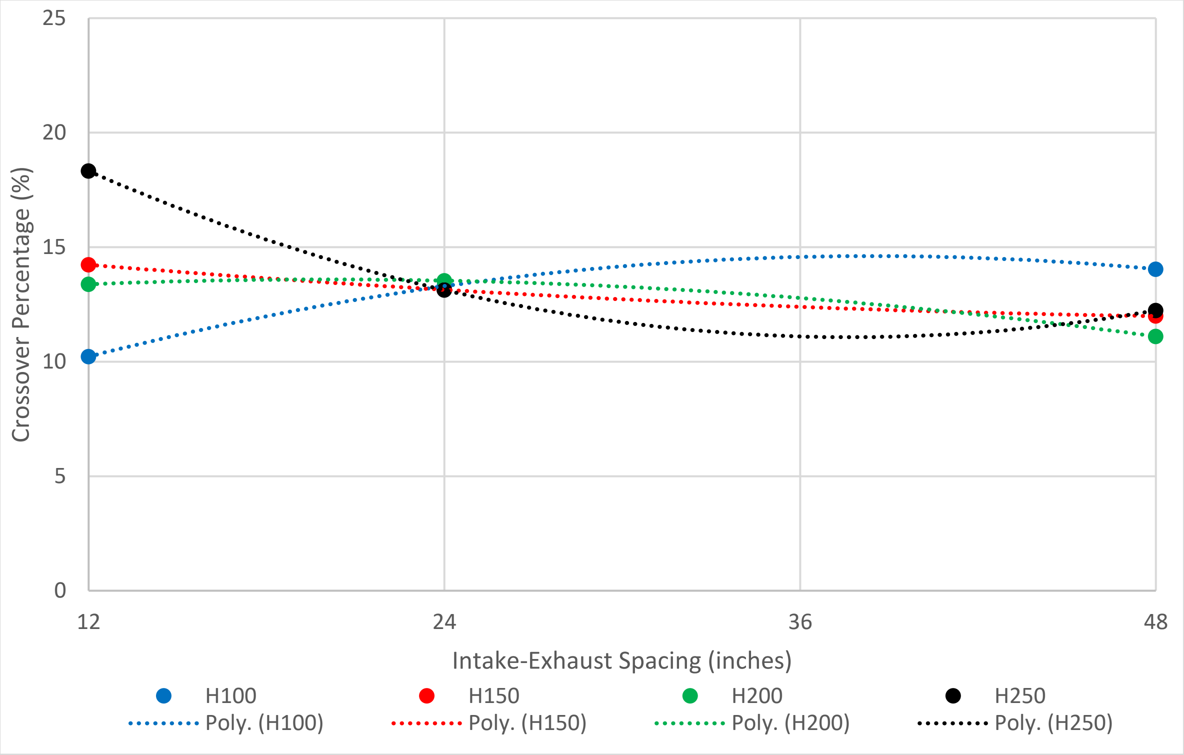

Figure 65: Horizontal Crossover vs. Intake-Exhaust Spacing

CHAPTER VIII

INLET-OUTLET AIRFLOW MIXING CFD SETUP

Overview

In conjunction with the airflow mixing experiments, an analysis of simulated airflow mixing was conducted by using Computational Fluid Dynamics (CFD) software in an effort to directly compare the results of the physical experiments to the simulated results.

Achieving a direct comparison to the wide range of physical mixing experiments required a significant investment and focus on CFD modeling and analysis. In regards to the CFD software package employed for this research, the ANSYS Fluent software was selected because it is widely used, powerful while supporting Graphic Processing Unit (GPU) acceleration. Numerous studies have been conducted on GPU acceleration for CFD modeling with NASA performing a study in 2009 that revealed a time to solution decrease of 25% (D. Jesperson). In addition to the CFD software, the Solidworks 3D Computer Aided Design (CAD) software was used with Fluent to create the physical model.

In terms of HVAC performance and building occupant health and comfort, it is essential to determine, evaluate, and analyze the cross-over airflow between the supply inlet and the return exhaust in order to quantify possible decreases in system performance and occupant comfort. Even though this cross-over airflow affects ERV performance, there is no evidence of previous studies addressing this problem. Therefore, an investigation was conducted, using CFD simulations to minimize the mixing of stale air and fresh air by determining the optimum center-to-center spacing between the inlet and outlet. The dilemma addressed in this study is that if connections are too close stale air can be sucked back into the structure; however, it is desirable from a real-world installation standpoint to place the outer wall intake and exhaust connections as close to each other as possible in order to minimize ducting and thus pressure drop.

Variables to be manipulated for the CFD simulations are the orientation (Vertical, Inverse Vertical and Horizontal), spacing (or distance in inches apart), flow rates, and ambient conditions. Two environmental conditions were simulated, with the first being 75°F/50% relative humidity air exhausted into a 0°F/50% relative humidity air-filled control volume, for the purpose of simulating a winter outdoor condition, also referred to as the Low Temperature (LT) scenario. The second environmental condition simulated was 75°F/50% relative humidity air exhausted into a 75°F/50% relative humidity ambient air filled control volume, even though this second environmental condition has the air exhausting to a control volume at the same conditions, which is why it is also referred to as the Equal Temperature (ET) scenario, they in fact have different carbon dioxide concentrations

The first of the above conditions provides insight into the buoyancy effects experienced from exhausting the much warmer air into the colder environment, while the second condition follows more closely with the physical experiments performed, as the exhaust air utilized the same laboratory air as the environmental conditions, albeit with additional CO_2 added. The simulations conducted for the CFD portion of this research are listed in Table 14 and represent 36 total unique simulations.

Table 14: CFD Simulations for Low Temperature (LT) and Equivalent Temperature (ET) Conditions

Center-to-Center Distance Between Exhaust and Intake	Volume Flow-Rates (One Low and One High)
O1 (12")	*100, 200 CFM*
O2 (24")	*100, 200 CFM*
O3 (48")	*100, 200 CFM*

Physical Model

Modeling of the ventilation grills, namely the ZN-160 ventilation grills as referenced in the equipment list, and the accompanying control volume was performed using Solidworks CAD software. The dimensioning in inches shown in the isometric engineering drawing in Figure 66 were taken directly via physical measurements of the grills used in the experimental study.

The fluid control volumes are subdivided into three parts. The first being the fluid volume inside the ventilation grill which is extracted in SpaceClaim, the second being a 10’x10’x2’ (200 ft^3) volume near the wall, and lastly a 10’x10’x8’ (800 ft^3) volume further from the wall. A front view of the wall can be seen in Figure 67, which highlights the horizontal and vertical measurements of the wall as well as the spacing’s for the three orientations and setups while the 3D model of the fluid control volume is visualized in Figure 68.

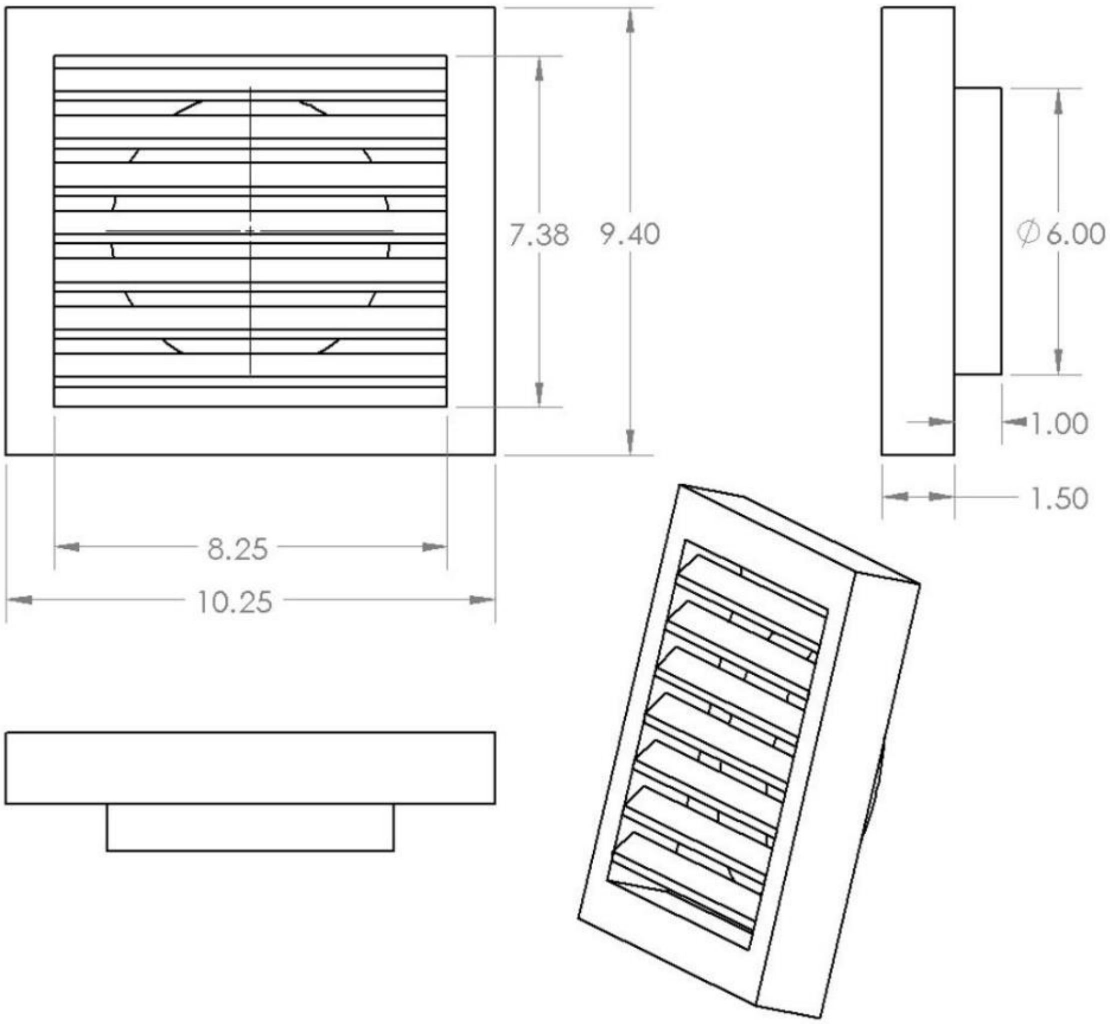

Figure 66: Ventilation Grill CAD Drawing

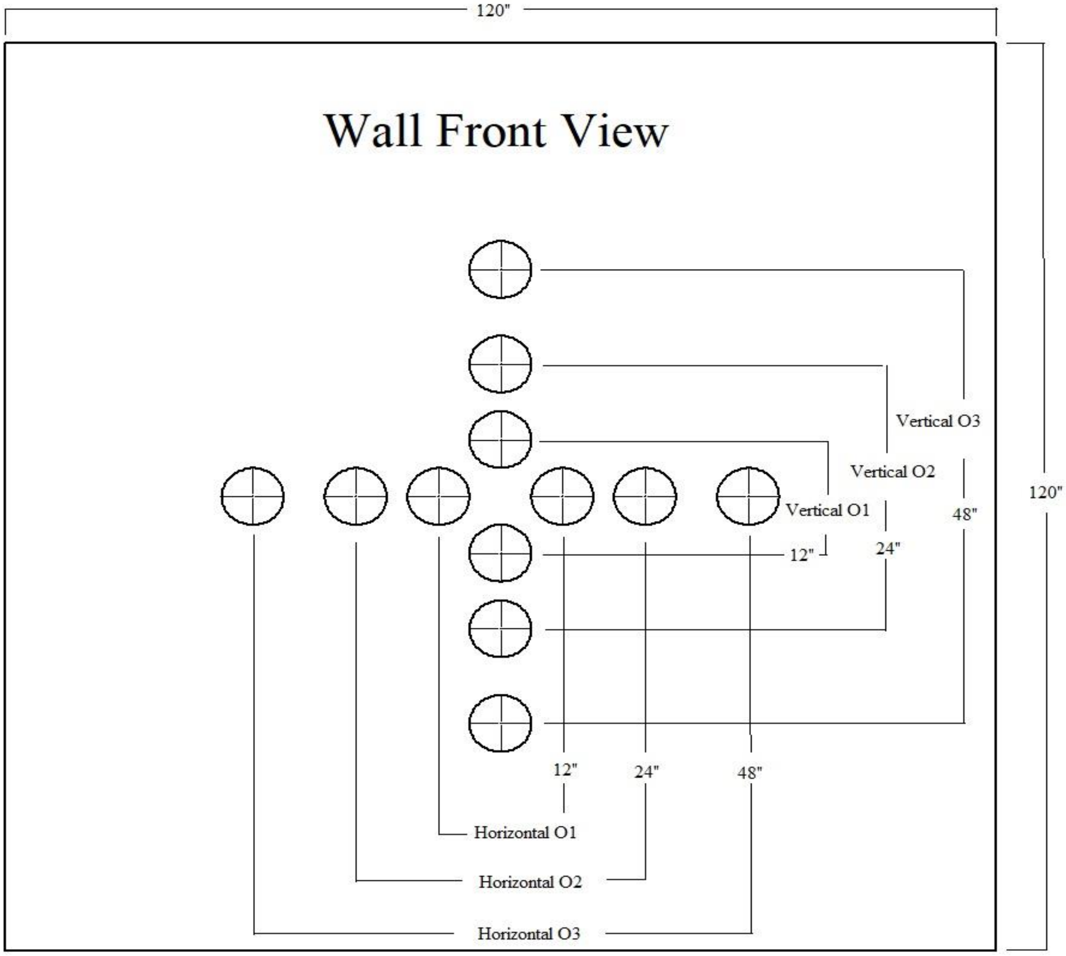

Figure 67: CFD Wall Front View

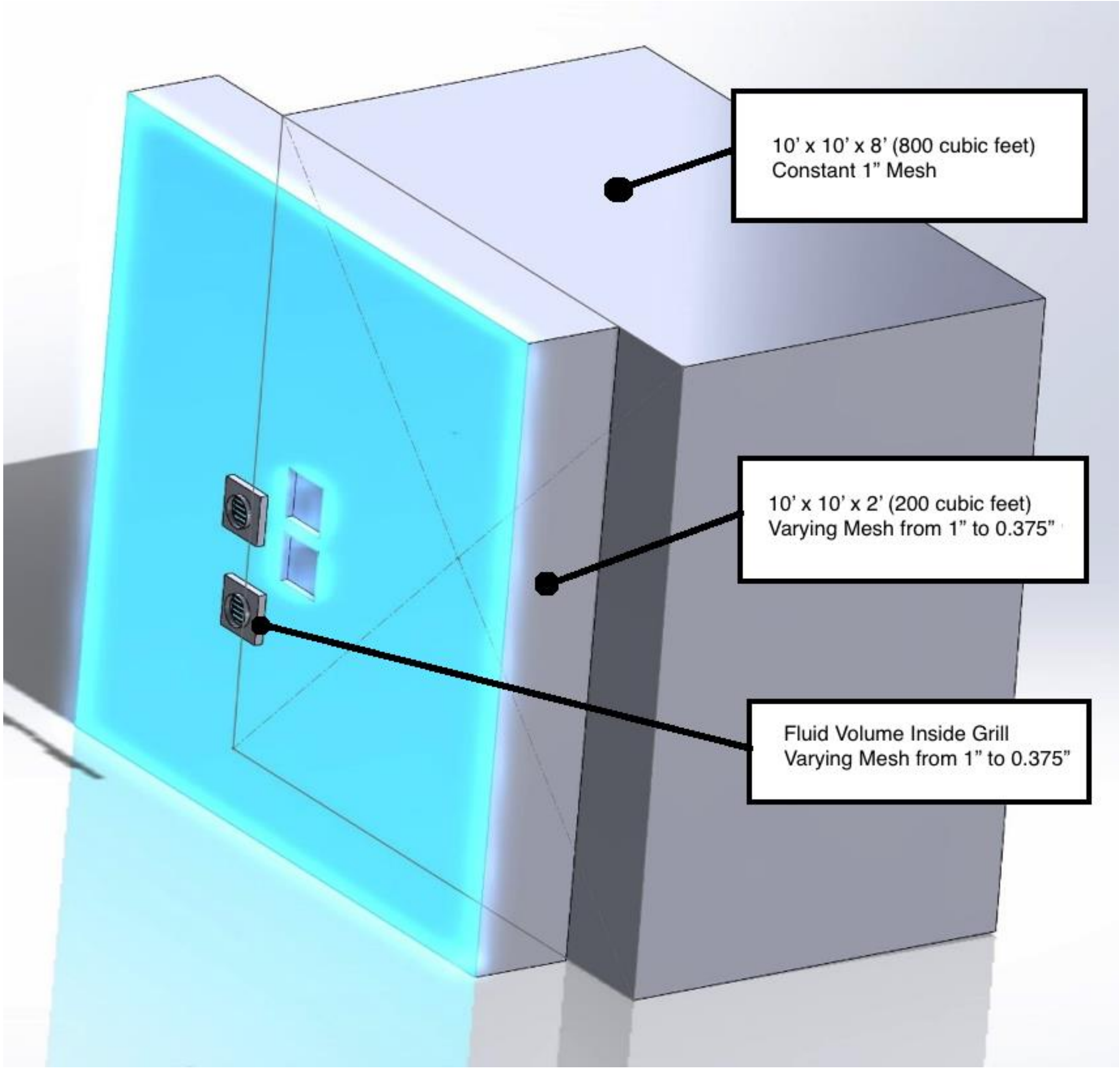

Figure 68: CFD 3D Model Breakdown

The grill arrangements as well as the grill spacings for the CFD study are varied in accordance with the physical experiments that were performed. These arrangements include vertical, inverse vertical, and horizontal orientations with three distinct spacings for each, resulting in a total of 9 configurations. Due to the computation time required for each simulation, only two flow-rates were selected to be analyzed, namely 100 and 200 cfm. These two flow rates were investigated for each configuration detailed in the physical experiments.

CFD Solution Parameters

Because the intake and exhaust model is located at the interface of the building and outdoor environment, a Large-Eddy Simulation (LES) was initially attempted, but then abandoned in favor of the more robust realizable k-e solver. This approach is also a more feasible option in lieu of a Direct Numerical Simulation (DNS) approach that requires a grid resolution to be at least as fine as the Kolmogorov microscales (Q. Chen & J. Srebric). Specifically, depending on the external Reynolds Number of the flows, a grid resolution of 10^{13} or finer would be needed, which is computationally prohibitive for the computer power available in this research.

It was anticipated that the pressure-velocity coupling would require that the model utilize the Semi-Implicit Method for Pressure Linked Equations (SIMPLE) or one of its variants, such as SIMPLE-Consistent (SIMPLEC) or SIMPLE-Revised (SIMPLER). The reason for this approach is because when scalar variables, such as temperature, are linked to the momentum equation the SIMPLE variants show a more robust convergence compared to other methods, such as PISO (D. Jang et al.). The SIMPLE pressure-velocity coupling method was selected due to it showing the most consistent results throughout the initial simulations involving the grid independence study.

The general parameters selected in ANSYS Fluent are a double precision, steady state, pressure-based, absolute velocity formulation solver with gravitational acceleration enabled at a rate of -9.81 m/s^2 on the y-axis. The CFD models enabled are the Energy Equation, Viscous

Model (Realizable k-e, standard wall treatments, full buoyancy effects), and the Species Model. Water vapor and dry air are the selected species for the low temperature (LT) simulations while carbon dioxide and dry air are selected for the the equal temperature (ET) simulations, with the mixing laws selected for the LT and ET simulations being shown in Figure 69.

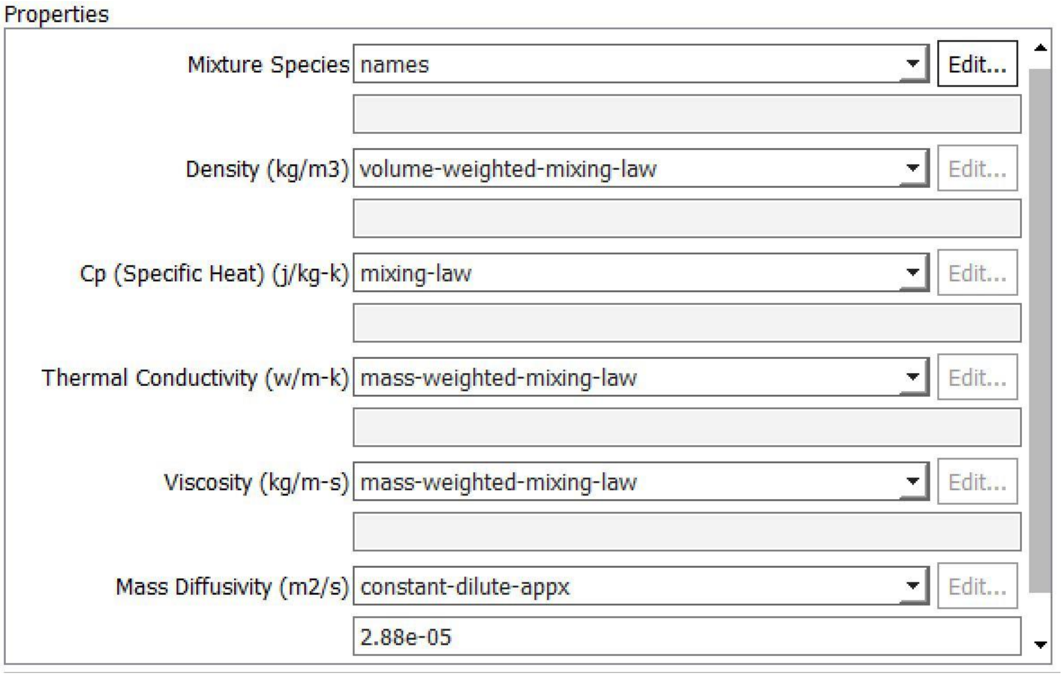

Properties

Mixture Species names

Density (kg/m3) volume-weighted-mixing-law

Cp (Specific Heat) (j/kg-k) mixing-law

Thermal Conductivity (w/m-k) mass-weighted-mixing-law

Viscosity (kg/m-s) mass-weighted-mixing-law

Mass Diffusivity (m2/s) constant-dilute-appx

2.88e-05

Figure 69: CFD Species Mixing Laws

The mixing laws selected for the physical properties enable the desired relative humidity percentage to be input as a species mass fraction for water vapor. This is obtained by first finding the vapor partial pressure (P_{H2O}) at the desired relative humidity and temperature, and the saturated vapor pressure (P_{H2O}^{*}) at the same temperature using Equation 18, while a more detailed method of finding the vapor partial pressure is provided in Appendix A. Because the molecular weight (MW) of dry air (DA) is 28.97g DA/mole, and the molecular weight of water is 18.016g H2O/mole, the molecular weight of the gas mixture can be calculated from Equation 19 and finally the mass fraction from Equation 20. An alternative method of determining the mass fraction is via a psychometric chart.

$$y_{H2O} = {}^{P_{H2O}}\!\big/_{P^*_{H2O}} \; ; y_{DA} = 1 - y_{H2O} \tag{18}$$

$$MW_{gas} = y_{DA} MW_{DA} + y_{H2O} MW_{H2O} \tag{19}$$

$$w_i = y_i \cdot \frac{MW_i}{MW_{gas}} \tag{20}$$

The calculated parameters for the low-temperature air properties are tabulated in Table 15. The relative humidity (RH) for both the indoor and outdoor air is set at 50%; however, the mass fraction in kg of water vapor to kg of dry air is provided next to it in parentheses. It is important to note that for the low-temperature simulations the mass fraction of water vapor in the outdoor is used to normalize the humidity in the crossover air. That is to say, the mass fraction of water in the outdoor air (0.00039kg/kg) is subtracted from the exhaust air as well as any simulated crossover air water vapor mass fractions. The air properties listed in Table 15 for the indoor and outdoor sections are directly used in the programming of the low-temperature CFD simulations, while the air properties corresponding to the indoor are are used for the equal-temperature simulations (all air at 75°F).

Table 15: Equal-Temperature and Low-Temperature CFD Air Properties

Indoor Air	T	23.9°C (75°F)
	RH	50% (0.00931 kg/kg)
	DP	12.8°C (55.1°F)
	P_v	1.479 kPa (0.215 psi)
	P_{vs}	2.963 kPa (0.429 psi)
Outdoor Air	T	-17.8°C (0°F)
	RH	50% (0.00039 kg/kg)
	DP	-24.9°C (-12.9°F)
	P_v	0.0745 kPa (0.0108 psi)
	P_{vs}	0.152 kPa (0.0221 psi)

CFD Grid Independence Study

The meshing of the control volume was primarily program controlled with the exception of two set body-sizing values inserted, or manual entries of maximum cell face size for a predefined volume. The 800 ft^3 volume was always meshed at a constant 1.0” mesh size while the 200 ft^3 volume, along with the internal volume of the ducts were meshed at varying sizes, from 1.0 to 0.375 inches maximum face size. The reasoning for this varying size is based on preliminary examinations of the flow characteristics, which revealed that the majority of the flow effects of interest occur near the wall thus requiring a finer mesh near the wall. Due to the small size of the cell faces, the method that the program selected was primarily tetrahedral dominant. Key mesh statistics, as well as simulation results, are reported in Table 16 with the primary surface monitors being outlet temperature and outlet humidity ratio.

Table 16: Grid Independence Study Statistics

Mesh Size (in)	**Cells**	**Outlet Temp. (°F)**	**Humidity Ratio** (h_{gv}/h_{ga})	**Solution Time (Hrs)**	**Skewness**	**Skewness (δ)**
1.0	3,236,001	25.5	0.0035445	-	0.1613	0.1376
0.75	10,148,325	39.3	0.0051340	15.1	0.1742	0.1305
0.625	18,871,163	42.8	0.0055219	32.2	0.1854	0.1255
0.45	25,535,567	45.3	0.0057970	47.7	0.1966	0.1196
0.375	43,340,416	44.9	0.0057432	140.0	0.1988	0.1173

As the mesh was refined for the mesh independence study, the mesh quality was slightly reduced (and conversely skewness increased) with each iteration; however, the standard deviation (δ) of these important mesh characteristics were all reduced. All levels of mesh refinement possessed an average skewness corresponding to an "excellent" cell quality as depicted in Table 17 (ANSYS). In Figure 70 the species concentration (humidity ratio) and the outlet temperature are plotted versus the quantity of mesh cells. It is readily apparent from observing Figure 70 that going from 25.5 to 43.3 million cells produces only a minor difference in these monitored values.

Table 17: CFD Skewness and Cell Quality

Value of Skewness	Cell Quality
1	Degenerate
0.9 - <1.0	Bad (Sliver)
0.75 - 0.9	Poor
0.50 - 0.75	Fair
0.25 - 0.50	Good
>0 - 0.25	Excellent
0	Equilateral

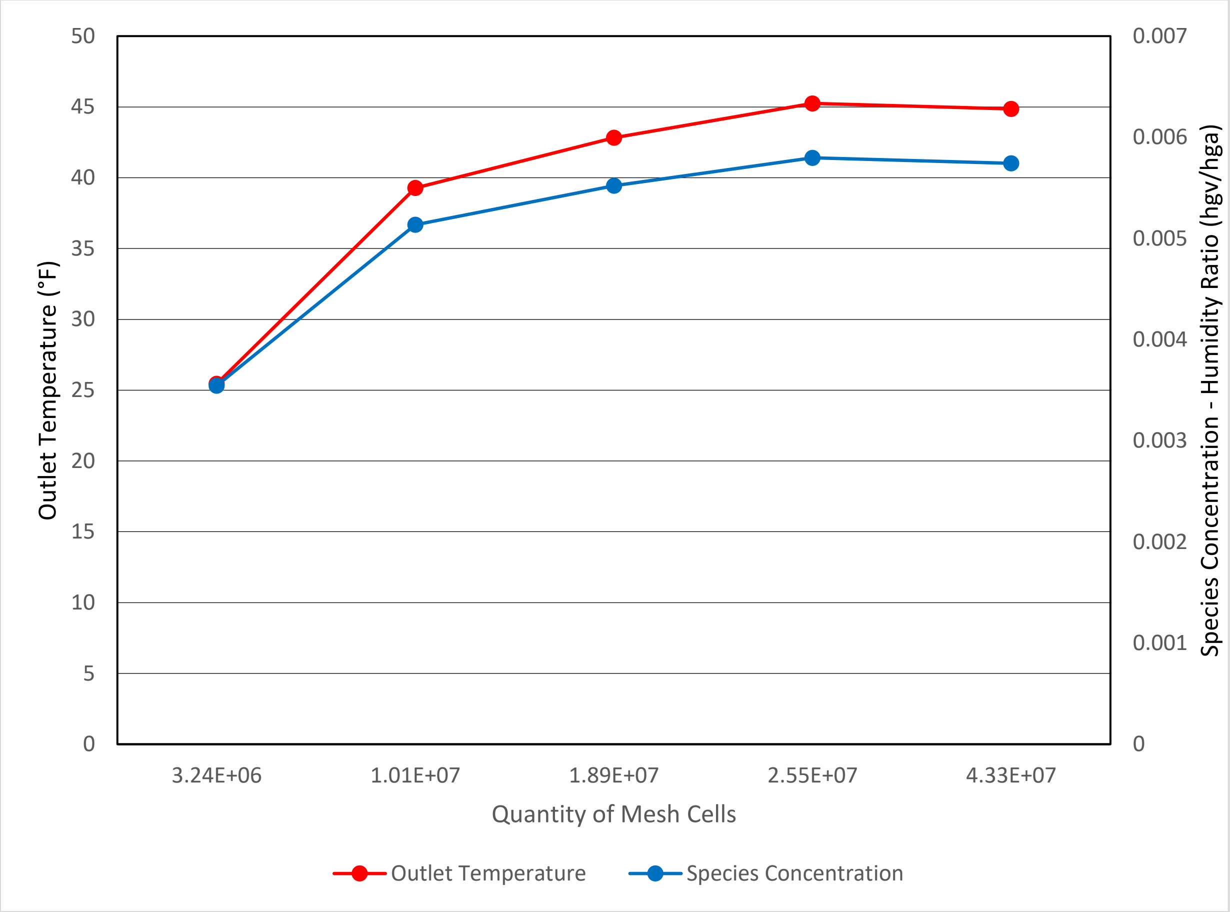

Figure 70: CFD Grid Independence Study Outlet Temperature and Humidity Ratio vs. Mesh Size

Referencing Figure 70, when the cell concentration is increased from 25.5 million cells to 43.3 million cells the outlet temperature shows a decrease of 0.4°F from 45.3 to 44.9°F, or a - 0.86% decrease, while the species concentration showed a -0.92% difference. Because the results for outlet temperature and species concentrations for the simulations carried out at both 25.5 and 43.3 million cells were less than a 1% difference from one another, the mesh corresponding to 25.5 million cells was selected for all simulations for this research. The reasoning behind this selection is that the coarser mesh reduces calculation time by approximately 4 days per simulation, or 108 days in total.

The variables of interest, such as the outlet temperature and humidity ratio, were monitored during the initial grid independence test as one method to determine convergence while the residuals were monitored as a second measure of convergence. Initially, simulations were set to run for 1,000 iterations to give an initial baseline of convergence and results during the selection of the solution parameters, such as which pressure-velocity coupling method to employ, however; once the solution parameters were finalized, the iteration count was increased until the variables of interest stabilized, namely the intake temperature. Figure 71 and Figure 72 show the result of increasing the iterations from 2,750 to 3,000. Due to the stabilizing effect witnessed with the addition of 250 iterations, all simulations presented herein are calculated for 3,000 iterations.

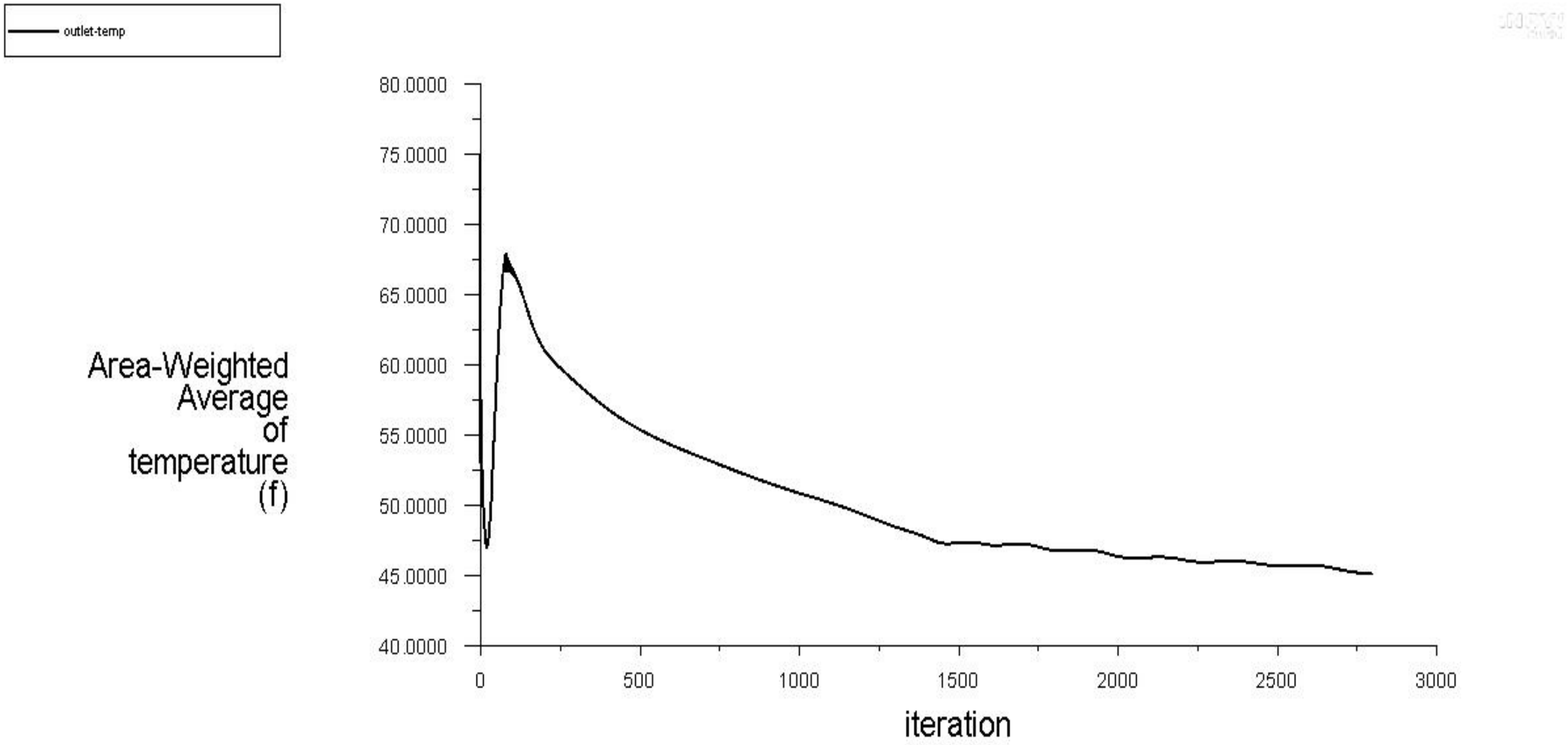

Figure 71: CFD Inlet Temperature vs. Iterations - 2,750 Iterations

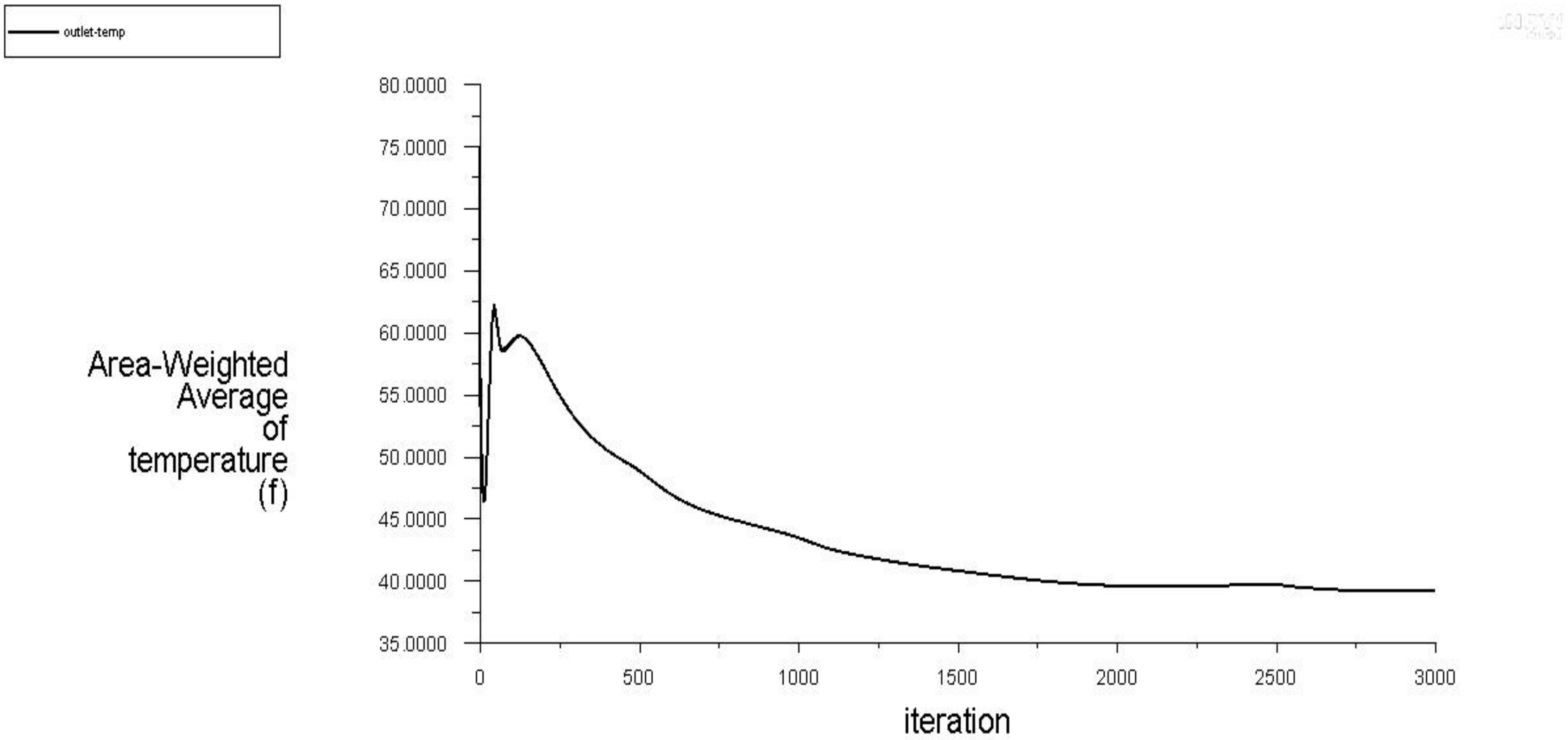

Figure 72: CFD Inlet Temperature vs Iterations - 3,000 Iteration

CHAPTER IX

CFD RESULTS

The results of the CFD simulations are presented in two parts. The first being the introduction and comparison between the two thermal conditions, namely the low temperature and equivalent temperature environmental scenarios. The first section will also detail the flow path of the exhaust stream via streamlines in CFX Post for select cases as well as the overall control volume temperature contours. The purpose of the equivalent temperature simulations is that it aligns with the experimental setup, in that all temperatures for the exhaust and ambient laboratory air are equal.

Environmental CFD Comparison

As mentioned in Chapter IX, the two environmental conditions evaluated are exhaust/ambient temperatures of 75°F/0°F and 75°F/75°F with the latter being the most realistic representation and comparison to the physical crossover experiments conducted.
For the equal temperature simulations, the “enable full buoyancy effects” solution parameter was de-selected as there are no thermal buoyancy effects when all objects are at the same temperature. As a result, the simulation time was reduced by approximately 8 hours resulting in a 88 hour simulation as opposed to the 96 hour simulation for the low temperature environmental condition. Similar to the physical experiments, the inverse vertical arrangement will be examined first, followed by the vertical, and finally the horizontal arrangement.

Inverse Vertical CFD Results

Beginning with the inverse vertical arrangement, the low temperature simulations were performed first, with the equal temperature simulations second. The exhaust humidity ratio, or h_{gv}/h_{ga}, was fixed at 0.00931 kg water vapor/kg dry air for all instances while the molar mass fraction, or w_i, of CO_2 with respect to one mole of air for the equal temperature conditions was fixed at 0.002277, or 2277 parts per million. As outlined previously, the duct spacings are denoted by Orientation 1 (O1),with a 12" separation, Orientation 2 (O2), with a 24" separation, and finally Orientation 3 (O3) with a 48" separation. The raw data for these simulations is presented in Table 18 for the low temperature conditions and Table 19 for the equal temperature conditions.

Table 18: Inverse Vertical Low Temperature CFD Results

		Exhaust (h_{gv}/h_{ga})	Intake (h_{gv}/h_{ga})	XO_A (%)
Orientation 1 (O1)	100 CFM	0.00931	0.00526039	**54.56**
	200 CFM	0.00931	0.00549210	**57.16**
Orientation 2 (O2)	100 CFM	0.00931	0.00375569	**37.68**
	200 CFM	0.00931	0.00323056	**31.78**
Orientation 3 (O3)	100 CFM	0.00931	0.00236331	**22.05**
	200 CFM	0.00931	0.00325281	**32.03**

Table 19: Inverse Vertical Equal Temperature CFD Results

		Exhaust ($\frac{MW_{CO2}}{MW_{air}}$)	Intake ($\frac{MW_{CO2}}{MW_{air}}$)	XO$_A$ (%)
Orientation 1 (O1)	100 CFM	0.00227727	0.00153838	**60.64**
	200 CFM	0.00227727	0.00155077	**61.30**
Orientation 2 (O2)	100 CFM	0.00227727	0.001223397	**43.86**
	200 CFM	0.00227727	0.00114247	**39.55**
Orientation 3 (O3)	100 CFM	0.00227727	0.00116142	**40.56**
	200 CFM	0.00227727	0.00115443	**40.19**

Crossover percentage, which similar to Equation 10 is defined as $XO_A(\%) = (\frac{Intake-C}{Exhaust-C}) \cdot 100$ for the equal temperature simulations and the low temperature simulations. For the equal temperature simulations, the constant C is defined as 0.0004, or the mass fraction of CO_2 in the air equivalent to 400ppm, which is the same concentration of CO_2 used to normalize the physical experiments. For the low-temperature simulations, the constant C is defined as 0.000398 kg water vapor per kg of dry air, which is the moisture content in the outdoor air as indicted in Table 15. As can be seen from the above Tables 18 and 19, there is a noticeable crossover increase from the low-temperature simulations to the equal-temperature simulations. This increase can be attributed to the large buoyancy effects encountered in the low temperature experiments as a result of the temperature difference of 75°F between the exhaust and the ambient environmental conditions in the control volume.

The equal temperature experiments resulted in a smaller range between the two flow rates for each orientation with the largest being a 4.31% decrease from 100 to 200 cfm while the low temperature simulations showed a maximum 10% increase from 100 to 200 cfm for the third orientation. The comparison between the results can be seen in Table 20, where the Low Temperature (LT) results are subtracted from the Equivalent Temperature (ET) results, or, $CFD_{Comp} = ET - LT$

Table 20: Inverse Vertical CFD Comparison for ET and LT

		LT (%)	ET (%)	$\mathrm{CFD}_{\mathrm{Comp}}$ (%)
Orientation 1 (O1)	100 CFM	54.56	60.64	**6.08**
	200 CFM	57.16	61.30	**4.14**
Orientation 2 (O2)	100 CFM	37.68	43.86	**6.19**
	200 CFM	31.78	39.55	**7.77**
Orientation 3 (O3)	100 CFM	22.05	40.56	**18.51**
	200 CFM	32.03	40.19	**8.15**

Table 20 reveals the extent of the crossover (XO) increase when equivalent exhaust and ambient temperatures are used in lieu of hot air exhausted into a cold environment. There is a minimum and maximum exhaust air crossover increase of 4% and 18.5%, respectively, when the equal temperature simulations are compared to the low temperature simulations. In addition to the increase in crossover due to the effects of increasing the working fluid temperature, it should also be noted that the exhaust and intake spacing are directly linked to the crossover percentages obtained in the simulations, as a rise in crossover is seen as the spacing distance is increased, such as O1 to O2 or O2 to O3.

In general, the discrepancy between the ET and LT simulations is less than 8%, with the exception of Orientation 3 at 100 cfm. It is possible that the result for the LT simulation for this instance would obtain more robust results by using a third-order solution method; however, solution methods are maintained constant for all simulations in an effort to create a baseline. A variety of CFD post processing images are presented in Figure 73 through Figure 75, encompassing the streamlines associated with the airflows as well as the temperature or CO2 mass fraction contours.

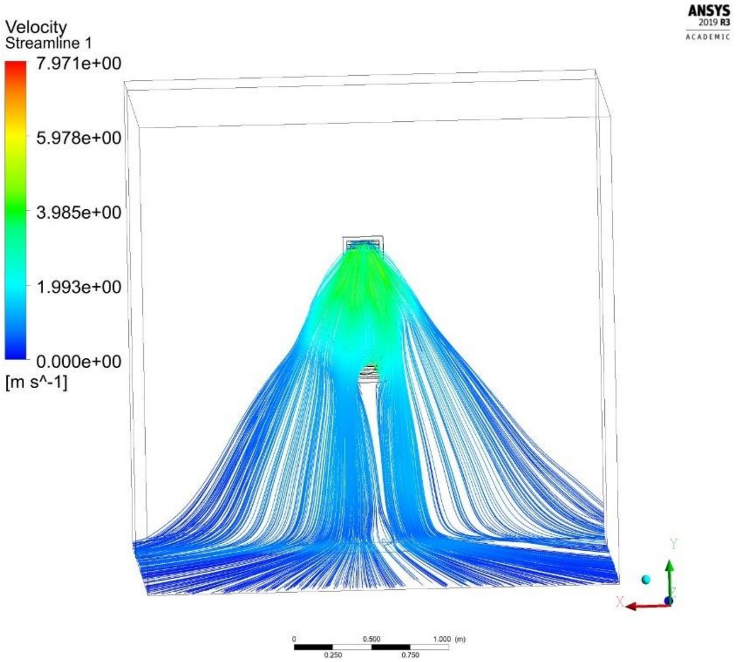

Figure 73: Inverse Vertical O2 200 CFM LT Streamlines

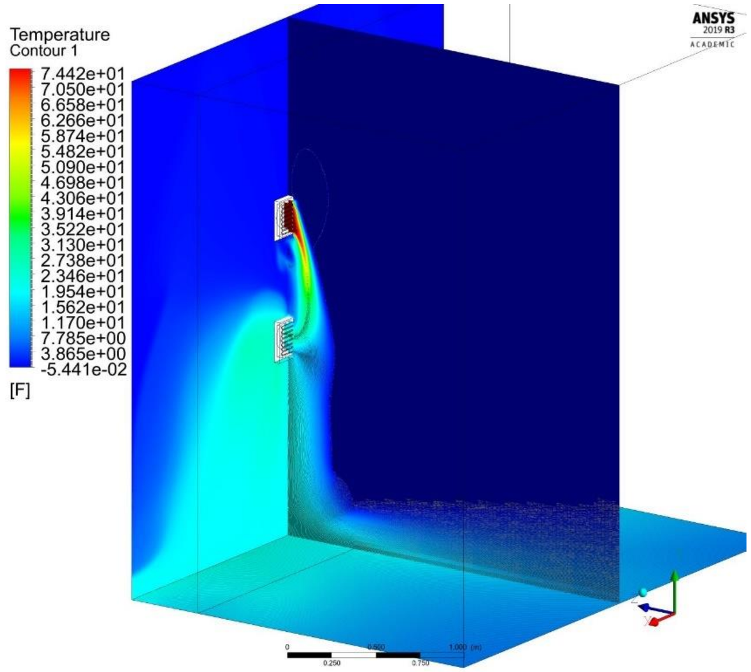

Figure 74: Inverse Vertical O2 200 CFM LT Temperature Contour

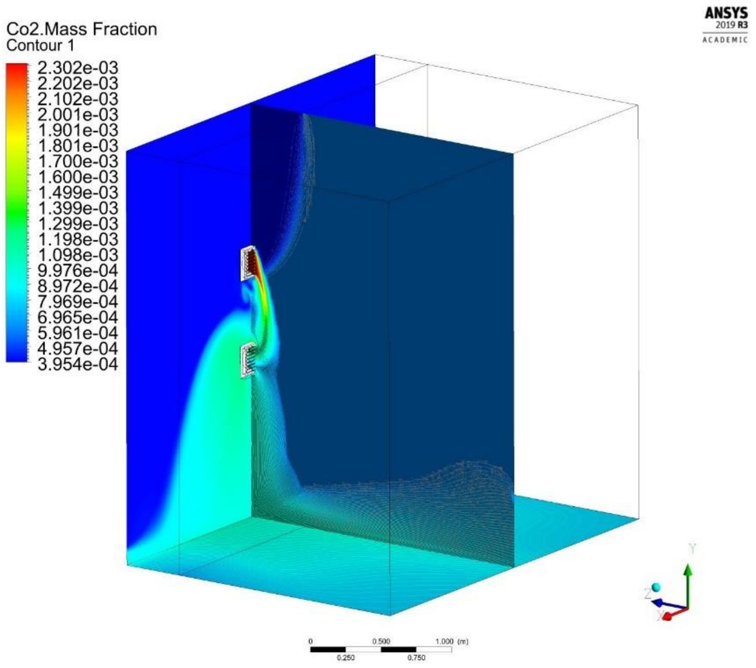

Figure 75: Inverse Vertical O2 200 CFM ET CO2 Mass Fraction Contour

Figure 73 represents the velocity streamlines as can be visualized from the exhaust with 2000 equally spaced points located at the 6-inch exhaust outlet. Streamlines are represented as both “backwards and forwards” meaning both flow in both the +Z and -Z axis is displayed, and it can be seen that there are negligible buoyancy effects in this instance as a large portion of the exhaust (>30%) is pulled into the intake located directly below the exhaust. Only the low temperature (LT) streamlines are presented for the inverse vertical setup as the equal temperature (ET) streamlines do not deviate significantly from the LT case due to the inverse arrangement. The temperature contour for the LT simulation reveals similar flow patterns to the CO_2 mass fraction contour in Figure 75. However, a build-up of CO_2 can be seen in the Y-Z plane with an area directly above the exhaust showing minor stratification.

Vertical CFD Results

The results of the vertical crossover CFD study follows the same pattern as the inverse vertical study presented in the previous section. The humidity ratio and CO_2 concentrations input into ANSYS Fluent for the air properties remain identical to the inverse vertical simulations as presented previously. As expected, the CFD simulations line up with the physical experiments, in that the results show a significant decline in airflow mixing when the exhaust and intake locations are reversed. However, in regards to the CFD simulations, every orientation for the low temperature (LT) simulations revealed a decline in crossover as the flow-rate is increased. This decline is most pronounced for the closer spacings of O1 and O2 with a minimum 50% decrease in simulated crossover for a doubling of volumetric flow rate of 100 to 200 cfm. The CFD results for the Vertical setup for the low temperature (LT) and equivalent temperature (ET) scenarios can be seen in Table 21 and Table 22 respectively.

Table 21: Vertical Low Temperature CFD Results

		Exhaust (h_{gv}/h_{ga})	Intake (h_{gv}/h_{ga})	XO (%)
Orientation 1 (O1)	100 CFM	0.00931	0.00196206	**17.55**
	200 CFM	0.00931	0.00073131	**3.74**
Orientation 2 (O2)	100 CFM	0.00931	0.00165038	**14.05**
	200 CFM	0.00931	0.00101138	**6.88**
Orientation 3 (O3)	100 CFM	0.00931	0.00137368	**10.95**
	200 CFM	0.00931	0.00078915	**4.39**

Table 22: Vertical Equal Temperature CFD Results

		Exhaust ($\frac{MW_{CO2}}{MW_{air}}$)	Intake ($\frac{MW_{CO2}}{MW_{air}}$)	XO (%)
Orientation 1 (O1)	100 CFM	0.00227727	0.00054474	**7.71**
	200 CFM	0.00227727	0.00052409	**6.61**
Orientation 2 (O2)	100 CFM	0.00227727	0.000537573	**7.33**
	200 CFM	0.00227727	0.000629243	**12.21**
Orientation 3 (O3)	100 CFM	0.00227727	0.000612669	**11.33**
	200 CFM	0.00227727	0.000623796	**11.92**

The equal temperature (ET) simulations of the vertical setup in general did not exhibit a decline in mixing with an increase in flow-rate. The first and third orientation (12” and 48” separation) revealed negligible increases or decreases in crossover as flow rate is increased, while the second orientation (24” separation) showed a 5% rise when the flow rate was doubled from 100 to 200 cfm. An interesting phenomenon appears when the equal temperature and low temperature cases for the vertical setup are compared directly and this can be seen in Table 23.

Table 23: Vertical ET and LT CFD Comparison

		LT (%)	ET (%)	CFD_{Comp} (%)
Orientation 1 (O1)	100 CFM	17.55	7.71	**-9.84**
	200 CFM	3.74	6.61	**2.87**
Orientation 2 (O2)	100 CFM	14.05	7.33	**-6.72**
	200 CFM	6.88	12.21	**5.33**
Orientation 3 (O3)	100 CFM	10.95	11.33	**0.38**
	200 CFM	4.39	11.92	**7.53**

As can be seen from Table 23, there is a trend where at the lowest flow rate of 100 cfm, the low temperature (LT) simulations revealed a higher crossover, with the exception of O3, being nearly 10% higher than the equal temperature scenario for O1. However, at the higher flow rates the equal temperature simulations revealed higher crossover with respect to the low temperature simulations, with crossover proceeding to rise as the spacing increased, increasing from differences of approximately 3% at O1 to 7.5% for O3.

This can possibly be due to the lower exit velocity at 100 cfm, which may allow the thermal buoyancy to cause the hot exhaust air to rise rather than be expelled far enough away from the wall interface such that it is not pulled back into the intake, as is the case with higher flow rates. Figure 76 and Figure 77 highlight the particle streamlines from the exhaust and the temperature contour for the low temperature (LT) simulations while Figure 78 and Figure 79 represent similar visuals for the equal temperature (ET) simulations.

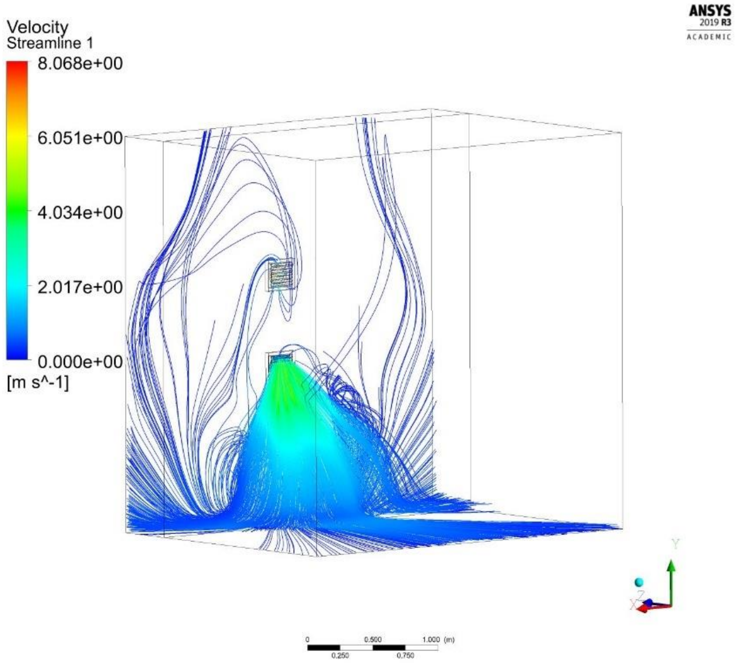

Figure 76: Vertical O2 200 CFM LT Streamlines

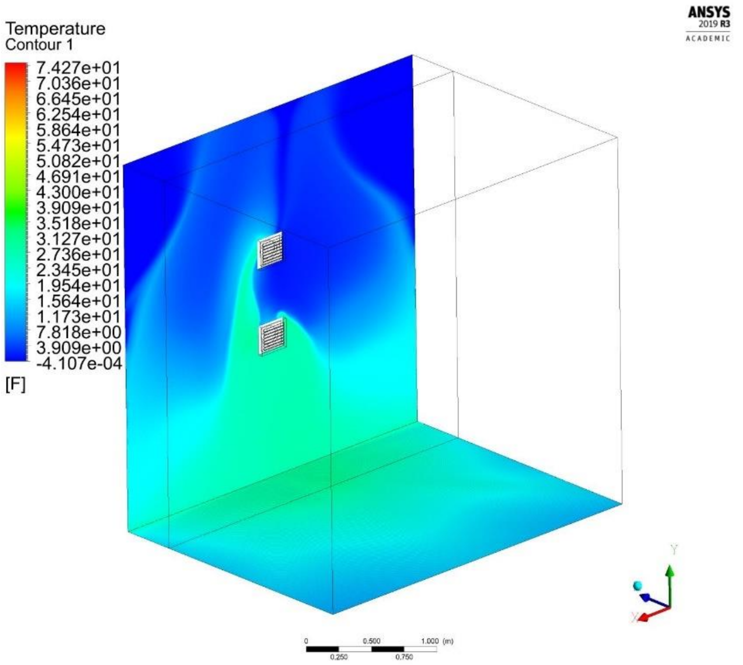

Figure 77: Vertical O2 200 CFM LT Temperature Contour

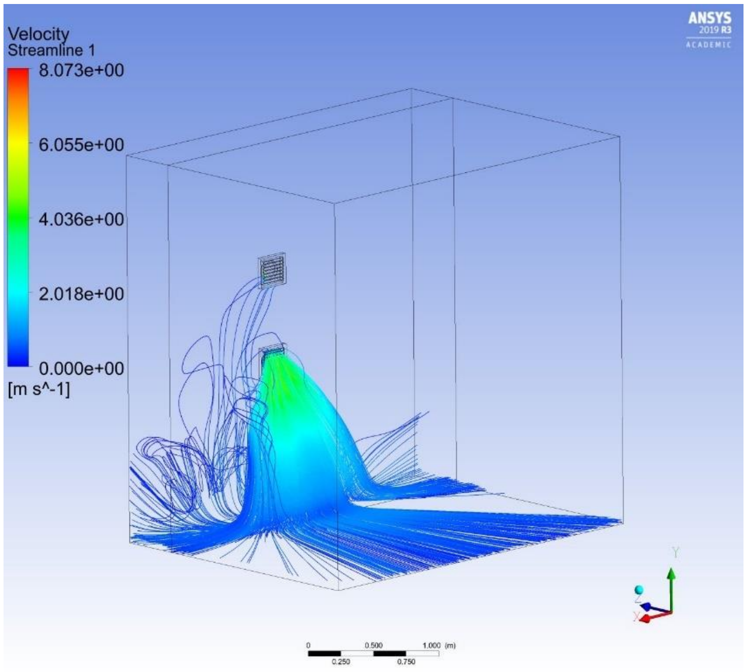

Figure 78: Vertical O2 200 CFM ET Streamlines

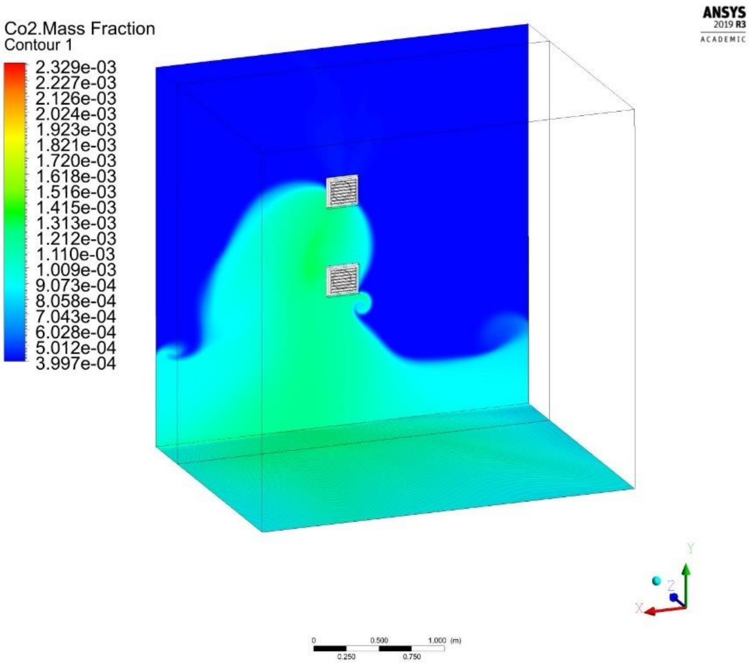

Figure 79: Vertical O2 200 CFM ET CO_2 Mass Fraction

The previous four figures visually represent what occurs for the 200 cfm O2 simulations in both the ET and LT cases. When comparing the streamlines for the LT and ET simulations as seen in Figure 76 and Figure 78, respectively, it is immediately visible that the hot, humid air that is exhausted rises and exits the control volume while the equivalent temperature air that is exhausted does not have any buoyancy effects and rather reveals a reflection from the floor, causing some of the exhausted air to be pulled into the intake. The buoyancy effect is most dominant for O1 and O2 at 100 cfm, while the reflection effect is most dominant for the higher flow rates of 200 cfm as well as when the spacing between the intake and exhaust is the greatest, namely O3 at 48” apart.

The temperature contour for the LT simulation highlights the heating of the floor and nearly symmetrical heating of the rear wall due to the buoyancy effects of the exhaust air. Figure

79 visually depicts the CO_2 mass fraction at the floor and back wall and reveals a build-up of CO_2 on the left side of the wall, which mirrors the reflections as seen in Figure 78 as caused by the high velocity air rebounding from the floor. The final round of CFD simulations that were performed are for the horizontal experimental setup.

Horizontal CFD Results

The horizontal CFD simulations possess the most consistent crossover percentage for the equal temperature scenario as all simulated crossover was within approximately 1.5% of one another while the low temperature simulations showed a very predictable pattern with decreasing crossover as intake and exhaust separation increased, as well as when the volumetric flow rate was increased. The low temperature simulations resulted in more diverse results with the highest crossover occurring at O1 and the lowest crossover occurring at O3. This can solely be attributed to the thermal buoyancy effects encountered due to the 75°F difference in exhaust air and ambient air (control volume) temperatures.

A higher order solution method and refined mesh may better predict the turbulent effects encountered for the low temperature scenario. This being said, there is a drop in mixing from 100 to 200 cfm for both O1 and O2 while O3 resulted in a slight increase in mixing as the flow rate is increased to 200 cfm. Table 24 and 25 detail the numerical results from the 12 horizontal CFD simulations conducted.

Table 24: Horizontal Low Temperature CFD Results

		Exhaust (h_{gv}/h_{ga})	Intake (h_{gv}/h_{ga})	XO %
Orientation 1 (O1)	100 CFM	0.00931	0.0015046	**12.42**
	200 CFM	0.00931	0.0011055	**7.94**
Orientation 2 (O2)	100 CFM	0.00931	0.0007681	**4.15**
	200 CFM	0.00931	0.0006275	**2.58**
Orientation 3 (O3)	100 CFM	0.00931	0.0009387	**6.07**
	200 CFM	0.00931	0.0010364	**7.16**

Table 25: Horizontal Equal Temperature Results

		Exhaust ($\frac{MW_{CO2}}{MW_{air}}$)	Intake ($\frac{MW_{CO2}}{MW_{air}}$)	XO (%)
Orientation 1 (O1)	100 CFM	0.00227727	0.0006382	**12.69**
	200 CFM	0.00227727	0.0006184	**11.64**
Orientation 2 (O2)	100 CFM	0.00227727	0.0006129	**11.34**
	200 CFM	0.00227727	0.0006077	**11.06**
Orientation 3 (O3)	100 CFM	0.00227727	0.0006080	**11.08**
	200 CFM	0.00227727	0.0006240	**11.93**

It is immediately visible from viewing the above two tables, namely Table 24 and 25, that the equivalent temperature (ET) simulations resulted in a significantly higher amount of mixing when compared to the low temperature (LT) scenario with the lowest divergence of 0.3% between the two scenarios occurring at O1 100 cfm and the highest being approximately 8.5%. The higher mixing values for the ET simulations can be attributed to the fact that no exhaust air is lost due to buoyancy effects, which is to say less exhaust air escapes the simulated control volume of 1000 ft^3.

When the air is exhausted at the same temperature as the ambient environmental conditions it has a neutral buoyancy and its velocity profile is defined by the flow rate and the geometry of the ventilation grill vanes. The results of these two simulations show that at cold outdoor temperatures a lower exhaust air transfer can be anticipated when compared to a similar setup for equivalent temperature outdoor temperatures. The relative increase in crossover is presented in Table 26 for the horizontal configuration.

Table 26: Horizontal Equal and Low Temperature Comparison

		LT (%)	ET (%)	CFD_{Comp} (%)
Orientation 1 (O1)	100 CFM	12.42	12.69	**0.27**
	200 CFM	7.94	11.64	**3.70**
Orientation 2 (O2)	100 CFM	4.15	11.34	**7.19**
	200 CFM	2.58	11.06	**8.49**
Orientation 3 (O3)	100 CFM	6.07	11.08	**5.01**
	200 CFM	7.16	11.93	**4.77**

Table 26 allows a direct comparison between the low temperature (LT) and equivalent temperature (ET) simulations where CFD_{Comp} is equal to the LT values subtracted from the ET values. The more pronounced mixing effect that occurs for the ET simulations can be observed as a direct result of this for the horizontal CFD simulations. With the exception of O1 at 100 cfm, there is approximately a 4% minimum increase in exhaust to intake crossover from the LT to the ET simulations and for most instances this corresponds to nearly double the values recorded for the LT simulations. For example, for O3 100 cfm there is a 5% difference between the LT result of 6.07% and the ET result of 11.06%, which relates to an 82.5% increase relative to the low temperature value of 6.07%.

Visual representations of the velocity streamlines originating from the exhaust duct were obtained in CFD-Post for the second orientation (O2) at 200 cfm for both the low temperature (LT) and equivalent temperature (ET) conditions. Figure 80 shows the low temperature streamlines as originating from the exhaust, while Figure 81 depicts the temperature contours for the wall and floor. The final two images, Figure 82 and Figure 83, depict the same setup and flowrate, except for the equal temperature case with Figure 83 depicting the CO_2 mass fraction contour on the floor and wall in lieu of the temperature contour.

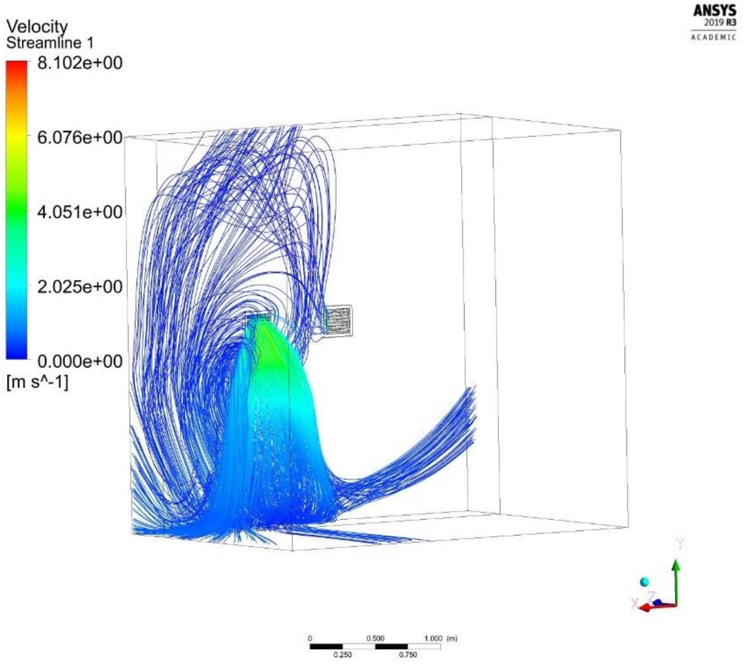

Figure 80: Horizontal O2 200 CFM LT Streamlines

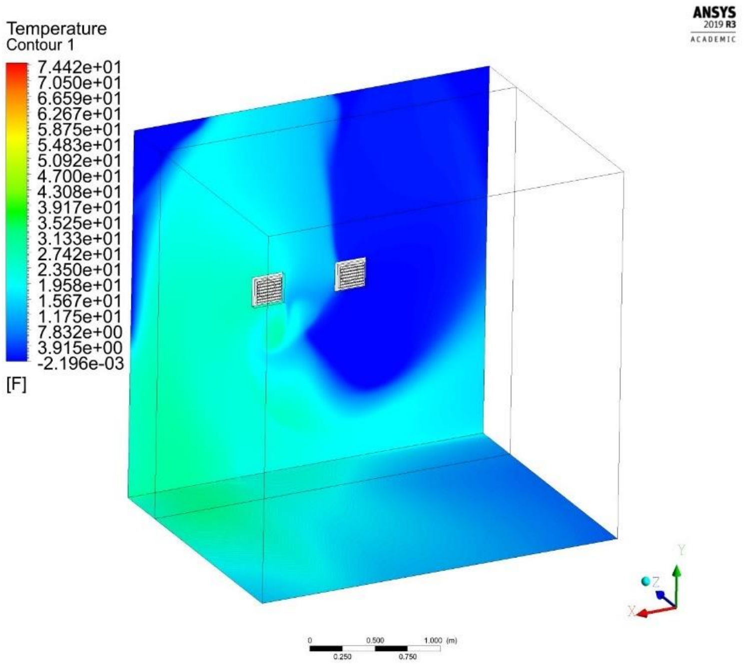

Figure 81: Horizontal O2 200 CFM LT Temperature Contour

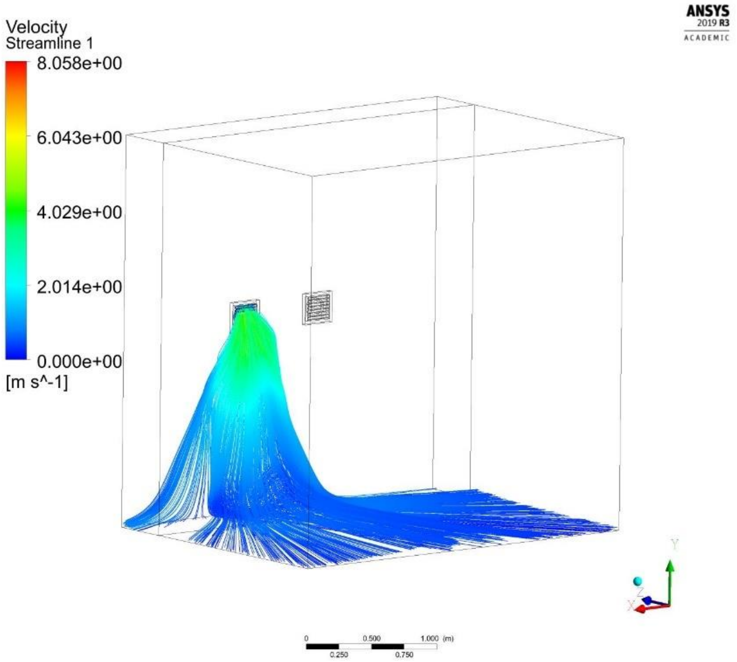

Figure 82: Horizontal O2 200 CFM ET Streamlines

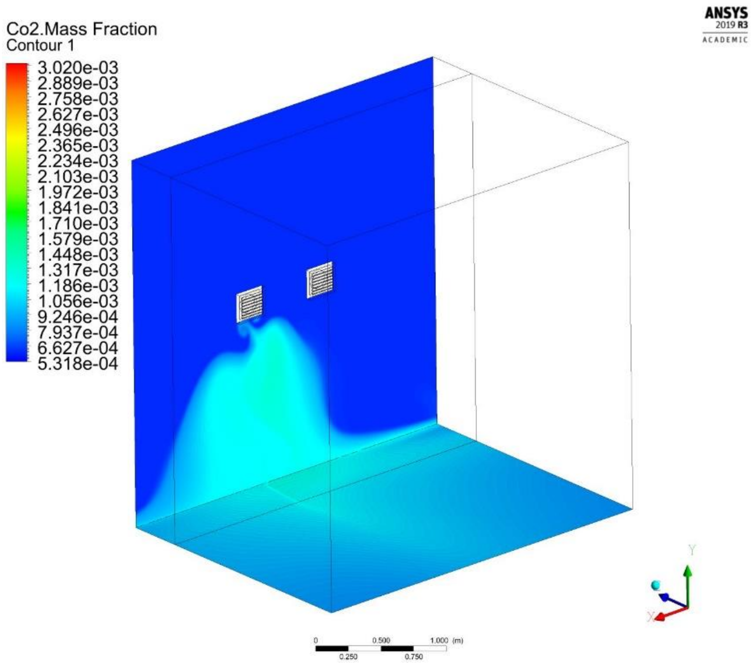

Figure 83: Horizontal O2 200 CFM ET CO2 Mass Fraction

Figure 80 through Figure 83 reveal a great deal about the physics of the flow for the equal and low-temperature scenarios in the horizontal configuration. It is immediately evident that there are strong buoyancy effects in Figure 81, with the velocity streamlines moving in the +y direction out of the control volume and little interaction with the floor. The effect of this on the temperature profile along the wall and floor reveals heating of the wall where the exhaust air begins to rise and coincides with the exhaust air streamlines. The CO_2 mass fraction contour in Figure 83 is provided as a direct comparison to the temperature contour of the LT simulation in Figure 81. This is because the temperature contour for the ET simulations do not provide any meaningful insights into the flow characteristics due to a result of the constant temperature in the control volume.

Minor reflection of the exhaust air-stream off the floor is observed in Figure 83, with the primary increase in CO_2 mass fraction along the wall occurring from the negative pressure in the area around the intake due to the suction effect as seen from the slight bowing effect in the -x direction of Figure 83. Due to the reduced reflections from the floor observed, it can be concluded that in order to avoid unwanted reflection the exhaust and intake vents should be positioned a minimum of 6 feet above the ground, which is 12” higher than presented in the simulations.

Experimental Results vs. CFD Results

In an effort to further validate the CFD results, the experimental results were directly compared to the low temperature (LT) and equivalent temperature (ET) simulations, which use the area-weighted average of the mass fraction of water vapor and CO2 concentration, respectively, at the intake and exhaust to calculate airflow mixing. It was determined that the results of the ET simulations most closely mirrored the physical experiments due the physical experiments being conducted at a constant temperature inside the laboratory which coincides with a lack of buoyancy effects present during the tests.

It should be noted that although the thermal conditions for the physical experiments most closely matched the CFD simulations for equivalent temperature, there were aerodynamic effects present in the real-life experiments that could not be accounted for and programmed into the CFD boundary conditions due to the unpredictable nature of air currents that may be present inside the laboratory. As a result, the boundary conditions for the CFD code were programmed in such a way that there were no cross-air currents, and the air in the control volume was assumed to have zero velocity in any direction prior to the insertion of the exhaust air stream, in other words it is assumed to be stagnant air.

The following three tables, namely Table 27 through

Table 29, representing the inverse vertical, vertical, and horizontal setups, respectively, exemplify the difference between the experimental (EXP) results and the equivalent temperature (ET) CFD results, denoted by Δ_{EXP-ET}.

Table 27: Experimental vs. CFD Results - Inverse Vertical

		LT (%)	ET (%)	EXP (%)	Δ_{EXP-ET} (%)
Orientation 1 (O1)	100 CFM	54.6	60.6	70.1	**9.5**
	200 CFM	57.2	61.3	76.9	**15.6**
Orientation 2 (O2)	100 CFM	37.7	43.9	50.9	**7.0**
	200 CFM	31.8	39.6	61.1	**21.6**
Orientation 3 (O3)	100 CFM	22.1	40.6	40.0	**-0.6**
	200 CFM	32.0	40.2	48.3	**8.1**

Table 28: Experimental vs. CFD Results - Vertical

		LT (%)	ET (%)	EXP (%)	Δ_{EXP-ET} (%)
Orientation 1 (O1)	100 CFM	17.6	7.7	6.3	**-1.5**
	200 CFM	3.7	6.6	8.5	**1.9**
Orientation 2 (O2)	100 CFM	14.1	7.3	6.3	**-1.1**
	200 CFM	6.9	12.2	8.9	**-3.3**
Orientation 3 (O3)	100 CFM	10.9	11.3	-	-
	200 CFM	4.4	11.9	-	-

Table 29: Experimental vs. CFD Results - Horizontal

		LT (%)	ET (%)	EXP (%)	Δ_{EXP-ET} (%)
Orientation 1 (O1)	100 CFM	12.4	12.7	10.2	**-2.5**
	200 CFM	7.9	11.6	13.4	**1.7**
Orientation 2 (O2)	100 CFM	4.2	11.3	13.3	**2.0**
	200 CFM	2.6	11.1	13.5	**2.5**
Orientation 3 (O3)	100 CFM	6.1	11.1	14.0	**3.0**
	200 CFM	7.2	11.9	11.1	**-0.8**

Beginning with Table 27, or the inverse vertical setup comparison, there are several points that can be concluded. First, the physical experiments had a higher overall crossover for nearly every setup. A trend can be observed for the 100 cfm flowrate, in that the difference between the experimental (EXP) and computational fluid dynamics (CFD) results decrease with each increase in exhaust/intake spacing. For example, for O1, O2 and O3 the difference decreases from 9.5% to 7.0% and finally -0.6%, respectively.

Secondly, the results for the 200 cfm simulations, as well as the closer spacings of O1 and O2, indicate that a third order solution method or finer mesh may be required to fully encompass the complexities of the flow. This can be concluded because for the inverse vertical experimental and CFD comparisons, there is between a 5% and 6% maximum deviance, which carries through to the other orientations.

Table 28, or the vertical setup comparison, shows a significantly smaller difference between the experimental results and the CFD results with maximum deviances of -3.3%

occurring at O2, 200 cfm. Comparisons for the third orientation are not available as physical experiments for the third orientation were not conducted. The CFD results for Orientation 1 and 2 at 100 cfm both reported less than a 1.5% difference, with -1.5 and -1.1%, respectively. The maximum difference for the vertical orientation is -3.3% for O2 at 200 cfm. While the majority of the vertical CFD ET simulations resulted in higher crossover values than the physical experiments, the difference between the physical and simulated results are small enough to be considered negligible due to the accuracies of the sensors and uncontrollable air currents in the laboratory while conducting a given physical test.

Table 29, or the horizontal setup comparison, revealed the most consistent differences between the physical experiments and the simulations, which can in part be attributed to the stable results obtained for the physical experiments. With a maximum deviation of 3% and a minimum of -0.8%, the horizontal orientation showed the closest match between the two methods of test. With all simulated results within 3% (and many within 2%) of the results obtained during the physical experiments.

There are several conclusions that can be drawn after assessing the results from comparing the physical experiments to the CFD experiments. At higher flowrates and closer intake and exhaust spacing’s, it appears that the simulations will benefit from a third order solution method and a finer mesh. Additionally, at orientations that are further apart, namely O2 and O3, the mesh can be refined in specific sectors, in lieu of globally, to help aid in resolution and keep compute time reasonable. The main two goals of the CFD simulations were to help visualize the exhaust flows and identify close convergence to the physical experiments to prove future experiments with intake and exhaust spacing can be relegated to CFD simulations. These simulations will obtain close fitting results to real-life scenarios in a reasonable amount of time while avoiding the cost and time of setting up individualized physical experiments. These goals were achieved as evidenced by the data and results presented previously, with the vertical and horizontal configurations showing approximately a 3% maximum difference from the physical experiments. Additionally, the 18 simulations were able to be solved with the computational power available in approximately 72 days, or 4 days per simulation, and this runtime can be significantly reduced by using advanced hardware such as supercomputers or cloud computing resources.

Effect on ERV Supply Enthalpy and Temperatures

After comparing the physical and simulated mixing results, a brief analysis regarding the effect that airflow crossover plays on the apparent effectiveness of an Energy Recovery Ventilator (ERV) is performed. A total of 130 unique ERV units were analyzed from the Home Ventilating Institute (HVI) database, representing a total of 385 unique data points, and are plotted in Figure 84 with the Adjusted Total Recovery Efficiency (ATRE) on the y-axis and the flow rate on the x-axis. The averaged ATRE for heating with outdoor air at 32°F and -13°F is 73% and 61%, respectively. It should be noted that there are fewer data points for tests at -13°F due to the high degree of difficulty and expense required to obtain a passing test at very low outdoor temperatures from a certified laboratory.

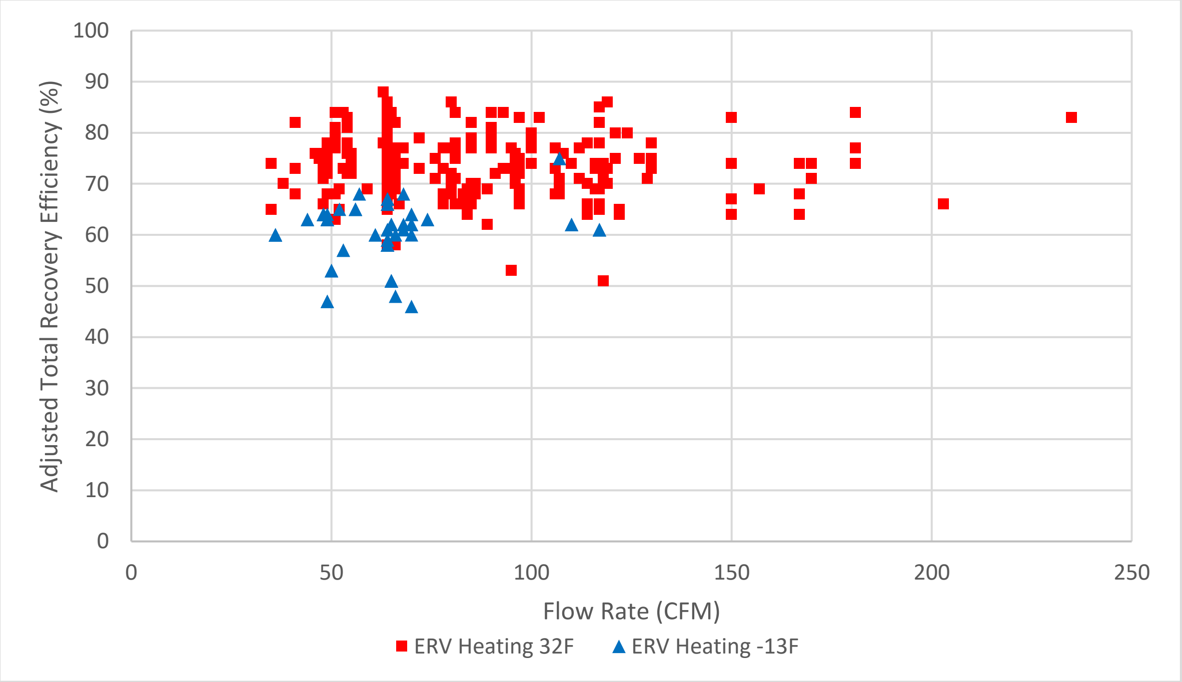

Figure 84: Energy Recover Ventilator ATRE vs. Flowrate for Low Temperature Conditions

Because the outdoor air for the low temperature simulations presented in this research is set to 0°F, the Apparent Unit Efficiency (AUE) can be reasonably approximated to 65% based off the certified values obtained via the HVI database used to create Figure 86. The AUE is needed in order to calculate possible air temperatures entering the building after passing through the exchanger.

Because the ATRE takes into account several measurements that could not be approximated via the simulated results, the Apparent Unit Effectiveness equation, as seen in Equation 18, is used instead to estimate possible increases in leaving supply air temperature (location X_2 in Figure 87) after passing through the ERV exchanger. A visual of the location for each of the variables used in Equation 18 is provided in Figure 85, and it should be noted that X_5

and X_6 are not used for this particular equation as they represent cross leakage across the ERV core which is assumed to be zero.

$$\varepsilon_{Apparent} = \frac{M_s \cdot (X_1 - X_2)}{M_{min} \cdot (X_1 - X_3)} \tag{18}$$

where,

M_s = mass flow rate of the supply air (lb/s)

M_{min} = mass flow rate of supply or exhaust, whichever is less (lb/s)

X = Dry bulb temperature, humidity ratio, or enthalpy at locations indicated in Figure 87 (Btu/lb)

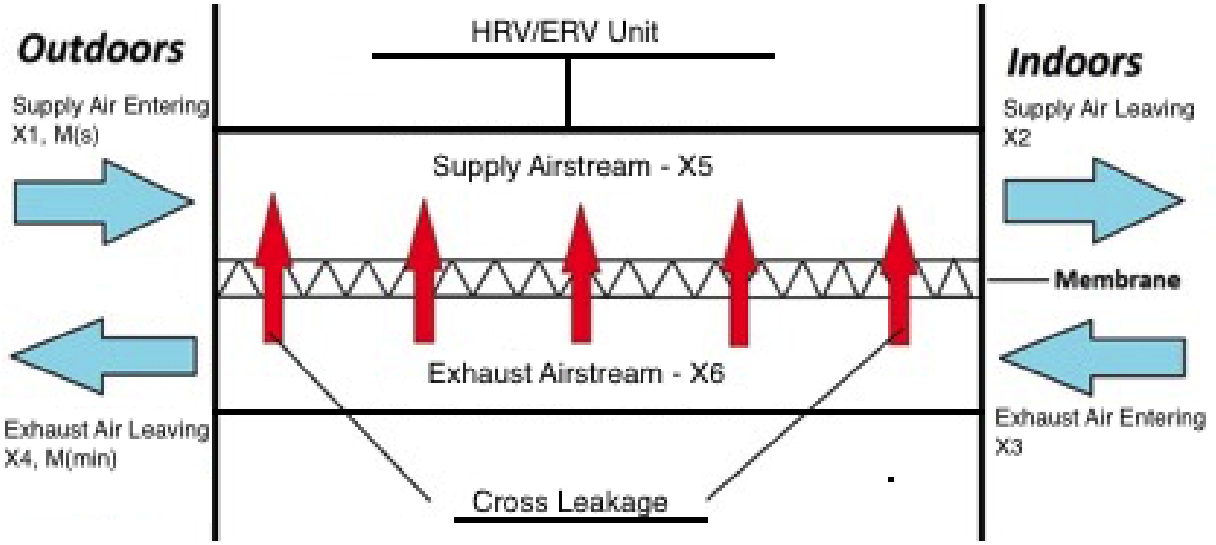

Figure 85: ERV Airflow Schematic for Apparent Effectiveness

The mass flow rates M_s and M_{min} are approximately equal, as M_{min} is equal to M_s due to the supply (or intake) having a lower mass flow rate than the exhaust, and thus these terms cancel out. The term X_2 must be solved for as X_3 is known and the temperature for X_1 is obtained via the low temperature simulations.

Due to both the dry-bulb temperature and humidity ratio being known, the enthalpy of the air at locations X_3 and X_1 can be calculated via Equation 19.

$$h = c_{pa} \cdot T + x(c_{pw} \cdot T + h_{we}) \tag{19}$$

where,

h = enthalpy (Btu/lb)

C_{pa} = Specific heat of dry air at constant pressure (0.24 Btu/lb·°F)

T = Temperature (°F)

C_{pw} = Specific heat of water vapor at constant pressure (0.444 Btu/lb·°F)

h_{we} = Evaporation heat of water at 32 °F (1061 Btu/lb)

x = humidity ratio (lb water vapor/lb dry air)

The ambient environmental air is set to the same temperature as the reference value of enthalpy for air, that is to say air at 0°F has an enthalpy of 0 Btu/lb. The temperatures and enthalpies at X_2, previously introduced in Figure 85, were calculated using the results from the low temperature simulations in conjunction with a constant ERV efficiency of 65%. These calculated values are tabulated in Table 30. The reference case, which assumes 0% exhaust to intake air crossover, are highlighted in the top row and provide an ideal scenario with no mixing.

Table 30: Projected Leaving Supply Air Temperature and Enthalpy

			T_1 (°F)	h_1 (Btu/lb)	h_2 (Btu/lb)	T_2 (°F)	T_3 (°F)	ε_{App} (%)-EQ.18
Reference Case			**0.0**	**0.00**	**18.68**	**48.8**	**75**	**65**
Inverse Vertical	Orientation 1 (O1)	100 CFM	40.9	15.50	**23.75**	**63.1**	75	65
		200 CFM	42.9	16.22	**24.00**	**63.8**	75	65
	Orientation 2 (O2)	100 CFM	28.3	10.81	**22.11**	**58.6**	75	65
		200 CFM	23.8	9.18	**21.54**	**57.1**	75	65
	Orientation 3 (O3)	100 CFM	16.5	6.49	**20.60**	**54.5**	75	65
		200 CFM	24.0	9.25	**21.56**	**57.2**	75	65
Vertical	Orientation 1 (O1)	100 CFM	13.2	5.25	**20.16**	**53.4**	75	65
		200 CFM	2.8	1.45	**18.83**	**49.7**	75	65
	Orientation 2 (O2)	100 CFM	10.5	4.29	**19.82**	**52.4**	75	65
		200 CFM	5.2	2.31	**19.13**	**50.6**	75	65
	Orientation 3 (O3)	100 CFM	8.2	3.43	**19.52**	**51.6**	75	65
		200 CFM	3.3	1.63	**18.89**	**49.9**	75	65
Horizontal	Orientation 1 (O1)	100 CFM	9.3	3.84	**19.67**	**52.0**	75	65
		200 CFM	6.0	2.60	**19.23**	**50.8**	75	65
	Orientation 2 (O2)	100 CFM	3.1	1.56	**18.87**	**49.8**	75	65
		200 CFM	1.9	1.13	**18.72**	**49.4**	75	65
	Orientation 3 (O3)	100 CFM	4.6	2.09	**19.05**	**50.3**	75	65
		200 CFM	5.4	2.39	**19.16**	**50.6**	75	65

The calculated temperature increases, using Equation 18 for apparent effectiveness for an ERV as provided by the CAN-CSA C439 standard, show minimum and maximum increases in the leaving supply air temperature (T_2) of 0.6°F and 15°F, respectively, when compared to the reference value of 48.8°F. Proportional increases in the enthalpy can be observed with minimum and maximum increases of 0.04 Btu/lb and 5.32 Btu/lb, respectively, when compared to the reference value of 18.68 Btu/lb.

A result of knowing both the temperature and humidity for the entering supply air (X_1), is that the air density can be calculated by using the partial pressures of dry air and water vapor; the process used is detailed in Appendix A; however, the density values used for future calculations were obtained directly from the CFD simulations. These density values can then be used with Equation 20 to calculate the mass flow rate of the entering supply air, and then used to calculate the amount of energy savings or losses observed (assuming X_1 and X_2 have the same mass flow rates), which would be the direct result of the mixing occurring for the low temperature simulations, as calculated via Equation 21.

$$\dot{m}_a = p\dot{V} \tag{20}$$

$$\Delta\dot{Q} = \dot{m}_a(h_2 - h_{ref}) \tag{21}$$

The calculated results of possible energy savings or losses are presented in Table 31, and it is immediately visible that regardless of arrangement, orientation, or flowrate, any mixing in a low-temperature environment relates to a decreased energy draw from a HVAC system when compared to reference air with zero mixing. This decreased energy usage is because less heat needs to be added to bring the air temperature up to a comfortable temperature.

Table 31: Projected Leaving Air Heat Loads

			p (kg/m^3)	$\dot{m}$ (lb/s)	$\dot{Q}$ (Btu/s)	$\dot{Q}$ (W)	$\Delta\dot{Q}$ (W)
Reference Case - 100 CFM			**1.224**	**0.127**	**2.38**	**2510.6**	**0.0**
Reference Case - 200 CFM			**1.224**	**0.255**	**4.76**	**5021.2**	**0.0**
Inverse Vertical	Orientation 1	100 CFM	1.225	0.127	3.03	3193.3	**682.7**
	(O1)	200 CFM	1.217	0.253	6.08	6412.0	**1390.7**
	Orientation 2	100 CFM	1.219	0.127	2.80	2959.4	**448.8**
	(O2)	200 CFM	1.220	0.254	5.47	5769.6	**748.4**
	Orientation 3	100 CFM	1.222	0.127	2.62	2761.6	**251.0**
	(O3)	200 CFM	1.220	0.254	5.47	5775.9	**754.7**
Vertical	Orientation 1	100 CFM	1.222	0.127	2.56	2704.6	**194.0**
	(O1)	200 CFM	1.224	0.255	4.80	5059.7	**38.5**
	Orientation 2	100 CFM	1.223	0.127	2.52	2660.4	**149.8**
	(O2)	200 CFM	1.224	0.255	4.87	5139.3	**118.1**
	Orientation 3	100 CFM	1.211	0.126	2.46	2596.2	**85.6**
	(O3)	200 CFM	1.224	0.255	4.81	5076.2	**54.9**
Horizontal	Orientation 1	100 CFM	1.223	0.127	2.50	2639.7	**129.1**
	(O1)	200 CFM	1.223	0.255	4.90	5166.0	**144.8**
	Orientation 2	100 CFM	1.224	0.127	2.40	2535.1	**24.5**
	(O2)	200 CFM	1.224	0.255	4.77	5030.3	**9.0**
	Orientation 3	100 CFM	1.224	0.127	2.43	2559.3	**48.7**
	(O3)	200 CFM	1.223	0.255	4.88	5146.4	**125.2**

As seen from Table 31, the increased crossover from the exhaust to the intake for all low temperature simulations causes the leaving supply air (X_2) to possess higher energy than the reference state, which has zero mixing. Delta Q refers to the additional amount of energy the leaving supply air has above the reference air. Cells in green represent instances where the equal temperature simulations were verified to be within 5% of the experimental values. Yellow cells are between 5 and 10% while cells are red are simulations that exceeded a 10% difference from the experimental results. Grey cells, namely both flowrates for vertical O3, did not have experimental results to compare against but can be assumed to be under 5% as is the case for the other vertical arrangements. As a result of these values representing higher energy than the reference state, less heat is necessary to increase the supply air to temperatures consistent with the ASHRAE standards for indoor comfort, namely ASHRAE Standard 55.

Assuming a 24/7 ERV operation and an electricity price of $0.20/kW-hr, energy savings over $2,000 USD are possible; however, if only cells in green are considered, a maximum energy savings of $440 is seen for the third inverse vertical orientation of 100 cfm. Geometries and flowrates that maximize energy savings whilst minimizing crossover are the vertical 12” spacing, and horizontal 12” and 48” spacing, all at flowrates of 200 cfm. These three geometries have energy savings of $207, $254, and $219 per year with exhaust-to-intake crossovers of 6.9, 7.9, and 7.2% respectively.

Because of the possibility of further energy savings as evidenced by the simulations and Table 31, certain installations may benefit from a small amount of mixing, so long as it does not adversely affect occupant comfort and health and falls within the scope of ASHRAE’s classes of air as referenced from the 62.1 Standard. To this end, this research sets the stage for future research examining methods for minimizing HVAC energy use while maximizing occupant health and comfort using airflow mixing as a cornerstone.

CHAPTER X

FUTURE WORK

The future work for this research consists of three parts. First, enhanced CO_2 sensors should be sourced and installed that possess a lower uncertainty than a base of +/-40ppm plus an additional +/-3% of the measured value. This will allow the vertical experiments at the third orientation to be completed and then the previous results can be re-verified using the advanced measurement devices.

Secondly, the CFD simulations should be updated to have a finer mesh resolution in specific areas of the control volume previously identified to have the greatest amount of turbulent airflow interaction. Additionally, the solution methods for high flowrate and large spacings should be updated to a third order solution method to increase resolution. However, this will greatly increase solution time and thus a high-performance computing (HPC) machine such as a supercomputer with significantly more compute nodes should be sourced to solve these simulations. In addition, a thorough analysis into the energy savings airflow mixing may provide to HVAC systems, such as an ERV, should be investigated and compared to the amount of fresh air required maintain occupant health and comfort.

Lastly, for the verification and validation of the experimental test facility a minimum of two energy recover ventilators (ERV's), previously accredited by a certified independent laboratory should be acquired and tested with a simulated outdoor condition of 95°F and 50% relative humidity at the maximum speed of the unit. This will allow a direct comparison to the published results which will assist in validating the facility. Additionally, a range of simulated outdoor temperatures (95°F - 110°F) and relative humidities (45% - 55%) should be tested at multiple volumetric flow rates. Once this is accomplished several tests at identical environmental conditions should be performed to identify repeatability.

CHAPTER XI

CONCLUSIONS

Major findings and contributions of this research on residential heat and energy recovery ventilators (HERV's), which is a technology that is increasingly being mandated in new constructions, are fourfold. First, a well instrumented test facility was designed and constructed in support of this research. Secondly, thorough extensive experimental testing, the determination of the ideal positioning of (HERV) exhaust and intake ports was realized. This positioning in turn minimizes exhaust contaminant transfer, which promotes IAQ, along with occupant health and comfort. Thirdly, visualizations of flow-patterns using Computational Fluid Dynamics (CFD) software, which were verified experimentally, were used to analyze low-temperature mixing scenarios that could not be achieved using the existing test apparatus. Lastly, the influence of mixing on the properties of air supplied to a building after passing through an Energy Recovery Ventilator (ERV) were assessed, which is an important step in promoting energy efficiency and reducing total HVAC energy usage.

The optimal placement of the exhaust and intake were determined to mitigate undesirable mixing from the exhaust air to the intake, common with HERV installations. In support of this endeavor, a novel testing facility was designed and constructed for the experimental collection of mixing data, which for this study consisted of 9 distinct intake and exhaust geometries at 4 volumetric flowrates, from 100 to 250 cfm. The measure of mixing, or crossover, in this study is defined as the ratio of the concentration of carbon dioxide present in the intake duct to the injected carbon dioxide concentration in the exhaust duct, which can also be expressed as a percentage. Experimental results identified a maximum crossover of 76.9% at an airflow rate of 200 cfm when the exhaust was positioned above the intake, also referred to as the inverse vertical arrangement. A minimum crossover of 6.3% at 100 cfm and 12” spacing was recorded when the intake was positioned above the exhaust, also referred to as the vertical configuration. However, at the same spacing of 12”, when flowrate increased to 250 cfm the crossover of 6.3% doubled to 13.5%. When the exhaust-and-intake was positioned side-by-side in a horizontal configuration, a maximum crossover of 18.3% was observed at 250 cfm and 12” spacing, and a minimum of 10.2% at a lower flowrate of 100 cfm and 12” spacing. Horizontal crossover dropped approximately 6% to 12.21% by quadrupling the distance of 12” to 48” at 250 cfm.

These research results highlight that airflow mixing at a building interface is significantly influenced by the exhaust-and-intake spacing for both the inverse vertical and horizontal configurations, while for the vertical configuration mixing is primarily influenced by the volumetric airflow rate. These findings are a significant contribution to HVAC design as this research shows inverted exhaust and intake port locations should be avoided, while vertical exhaust and intake arrangements are the most favorable. For installations with high flowrates (over 250 cfm) and port spacings of 48” or greater are implemented, a horizontal arrangement may be considered on a case-by-case basis.

CFD simulations using 75°F for both the exhaust and ambient air intake temperatures is a close representation of the experimental tests, and it resulted in less mixing when compared to experimental results. The low-temperature simulations, with a 75°F exhaust air temperature and 0°F ambient air temperature, which could not be experimentally tested, reported significantly less mixing due to the effect of thermal buoyancy. Maximum equal temperature crossover values of 61.3%, 12.2%, and 12.7% and maximum low-temperature crossover values of 54.6%, 17.6%, and 12.4% were reported for the inverse vertical, vertical, and horizontal arrangements, respectively. A direct verification of the equal temperature CFD results to the experiments for the inverse vertical setup revealed maximum and minimum differences of 21.6% and -0.6%, respectively; however, at lower flowrates of 100 cfm the differences were all under 10%, suggesting a finer mesh is necessary for higher flowrate applications. The vertical setup revealed a maximum difference of -3.3% at 200 cfm and a minimum of -1.1% at 100 cfm. Horizontal was similarly consistent across all flowrates and distances with maximum and minimums of 3.0% and -0.8% at 100 and 200 cfm, respectively. Because the CFD model was verified to show a close correlation to the physical experiments, it would thus appear that CFD modeling can accurately predict intake-and-exhaust mixing, which is significant in that designers can predict by using CFD exhaust-to-intake mixing in scenarios that would otherwise be difficult or cost prohibitive to experimentally verify.

In addition to the above CFD mixing study, after verification of the CFD model, simulated low-temperature results were used to determine the effect of exhaust-to-intake crossover on the properties of air returned to the interior of a building after passing through an ERV, which can significantly affect ERV performance. Specifically, some levels of mixing at locations and airflow rates that this research identified can in fact reduce HVAC system energy usage, which is desirable so long as occupant comfort and health is maintained within existing standards. Given an ideal reference scenario with an exhaust temperature of 75°F, outdoor temperature of 0°F, 0% mixing, and a 65% ERV efficiency, the temperature of the air returned to the building is 48.8°F, calculated using the apparent unit effectiveness for ERV's. Minimum and maximum returning air temperatures recorded from the low-temperature simulations of 49.7°F and 63.8°F were calculated using the equation for apparent effectiveness for an ERV. These values represent a 0.9°F and 15.0°F increase in air temperatures over the ideal reference case, respectively, which would appear to be due to mixing. Air enthalpy, a measure of the energy in the air that takes into account both air temperature and moisture content, was used to calculate possible energy savings to the residential HVAC system as a result of optimum intake and exhaust placement. A minimum energy savings of 9W and maximum of 1.39kW were calculated using the results from the results from the low-temperature CFD simulations. Assuming a 24/7 operation and an electricity price of $0.20/kW-hr, cost savings above $2,000 USD per year are possible; however, if the exhaust-to-intake crossover is maintained between 6 and 7%, then a savings of approximately $250 per year is observed.

Based on the analysis performed in this research study, one should avoid positioning the exhaust above the intake regardless of flowrate or distance, as the minimum crossover of 40% for this arrangement was greater than the maximum crossover of 18.32% for all other arrangements. This directive to designers, along with several more presented, are major contributions of this study, leading to improved IAQ and better HERV efficiency.

NOMENCLATURE

ASHRAE – American Society of Heating and Ventilating Engineers

BTU – British Thermal Unit

CAGR – Compound Annual Growth Rating

CFD – Computational Fluid Dynamics

CFM – Cubic Feet per Minute

EA – Exhaust Air

ERV – Energy Recovery Ventilator

GPU – Graphical Processing Unit

HRV – Heat Recovery Ventilator

HVI – Home Ventilating Institute

IAPWS – International Association for the Properties of Water and Steam

IAQ – Indoor Air Quality

LES – Large Eddy Simulation

LT – Low Temperature

ET – Equal Temperatures

OA – Outdoor Air

RA – Return Air

RH – Relative Humidity

SA – Supply Air

VOC – Volatile Organic Compound

P – Pressure

O1 – Orientation 1

O2 – Orientation 2

O3 – Orientation 3

V – Vertical

IV – Inverse Vertical

H - Horizontal

T – Temperature

DP – Dew Point

$\dot{m}$ - Mass Flow Rate

h - Enthalpy

HPC – High Performance Computing

Subscripts

v - Vapor

vs – Saturated Vapor

REFERENCES

Advanced Energy. *Top Advantages Of Scr Power Controllers Over Contactors And Solid-State Relays* . 2017, www.advancedenergy.com/globalassets/resources-root/white-papers/top-advantages-scrs-white-paper.pdf.

ANSI/AMCA 210-16. "*Laboratory Methods Of Testing Fans For Certified Aerodynamic Performance Rating"*, ANSI/AMCA, 2016. webstore.ansi.org/Standards/AMCA/ANSIAMCA21016.

ANSI/ASHRAE Standard 41.1-2013. "*Standard Method For Temperature Measurement",* ASHRAE, 2013. webstore.ansi.org/Standards/ASHRAE/ANSIASHRAEStandard412013.

Antoine, C. (1888), "Tensions des vapeurs; nouvelle relation entre les tensions et les températures" [Vapor Pressure: a new relationship between pressure and temperature], *Comptes Rendus des Séances de l'Académie des Sciences* (in French), **107**: 681–684, 778–780, 836–837

Aprilaire. *Series 800 Steam Humidifier Installation & Maintenance Instructions*. 2019, www.sylvane.com/media/documents/products/aprilaire-800-865-humidifier-installation-guide.pdf.

ASHRAE 51-16. "*Laboratory Methods of Testing Fans for Aerodynamic Performance Rating",* 2016. www.techstreet.com/standards/ashrae-amca-51-2016?product_id=1929730.

ASHRAE 55-2017. "*Thermal Environmental Conditions for Human Occupancy",* 2017. www.ashrae.org/technical-resources/bookstore/standard-55-thermal-environmental-conditions-for-human-occupancy.

ASHRAE 90.1-2016. "*Energy Standard for Buildings Except Low-Rise Residential Buildings",* 2016. www.ashrae.org/technical-resources/bookstore/standard-90-1.

ASHRAE Handbook-*Fundamentals*. ASHRAE, 2017, 2017.

ASHRAE, *ANSI/ASHRAE Standard 111-2008 (RA 2017). Measurement, Testing, Adjusting, and Balancing of Building HVAC Systems* 2008, American Society of Heating, Refrigerating, and Air-Conditioning Engineers, Inc.: Atlanta, GA.

ASTM. "Standard Specification for Temperature-Electromotive Force Tables for Standardized Thermocouples." *ASTM E230/E230M-17*, 2017.

Bermejo-Busto, Javier, et al. "Performance Simulation of Heat Recovery Ventilator Cores in Cascade Connection." *Energy and Buildings*, vol. 134, 15 Nov. 2016, pp. 25–36., doi:10.1016/j.enbuild.2016.11.014.

Boardman, Cr, and Samuel V Glass. “Moisture Transfer through the Membrane of a Cross-Flow Energy Recovery Ventilator: Measurement and Simple Data-Driven Modeling.” *Journal of Building Physics*, vol. 38, no. 5, 2013, pp. 389–418., doi:10.1177/1744259113506072.

CAN/CSA C439-18. “*Standard Laboratory Methods of Test for Rating the Performance of Heat/Energy-Recovery Ventilators”*, 2018. www.techstreet.com/standards/csa-c439-18?product_id=2003908.

Chen, Q, and J Srebric. *Application of CFD Tools for Indoor and Outdoor Environment Design*. International Journal on Architectural Science, 2000.

Chromalox. *Determining Energy Requirements - Air & Gas Heating*. www.chromalox.com/catalog/resources/technical-information/Heat-Loss-Calculations-and-Heater-Selection-Air-and-Gas.pdf.

Dwyer. “Series CDT-Carbon Dioxide/Temperature Transmitter.” Dwyer Instruments, Jan. 2017.

Elekor. “WattsOn-Mark II Precision Energy Meter Specifications” Elekor Technologies Inc. <http://www.elkor.net/pdfs/WattsOn-Mark_II_Datasheet.pdf

Engarnevis, Amin, et al. “Heat and Mass Transfer Modeling in Enthalpy Exchangers Using Asymmetric Composite Membranes.” *Journal of Membrane Science*, vol. 556, 2018, pp. 248–262., doi:10.1016/j.memsci.2018.03.007.

Engarnevis, Amin, et al. “Particulate Fouling Assessment in Membrane Based Air-to-Air Energy Exchangers.” *Energy and Buildings*, vol. 150, 25 May 2017, pp. 477–487., doi:10.1016/j.enbuild.2017.05.046.

Frost & Sullivan, *North American Energy Recovery Ventilation Markets,* 2007. store.frost.com/north-american-energy-recovery-ventilation-markets.html.

Global Info Research, *“Energy Recovery Ventilation System Market – Global Industry Analysis, Size, Share, Trends, Growth and Forecast 2018 – 2023”*, 2018.

Hoger, Ryan R. “Energy Recovery Ventilation.” LEED. 12 Dec. 2013.

Home Ventilating Institute, “*HVI Product Performance Certification Procedure*.” 25 Sept. 2015, www.hvi.org/ratings/Publication_920_rev_09292015.pdf.

Huizing, Ryan, et al. “Contaminant Transport in Membrane Based Energy Recovery Ventilators.” *Science and Technology for the Built Environment*, vol. 21, no. 1, 10 Sept. 2014, pp. 54–66., doi:10.1080/10789669.2014.969171.

Huizing, Ryan, et al. “Impregnated Electrospun Nanofibrous Membranes for Water Vapour Transport Applications.” *Journal of Membrane Science*, vol. 461, 17 Mar. 2014, pp. 146–160., doi:10.1016/j.memsci.2014.03.019.

Hyland, R. W., and A. Wexler. 1983b. Formulations for the thermodynamic properties of the saturated phases of H2O from 173.15 K to 473.15 K. *ASHRAE Transactions* 89(2A):500-519

IAPWS. 2011. *Revised release on the pressure along the melting and sublimination curves of ordinary water substance*. International Association for the Properties of Water and Steam, Oakville, ON, Canada. www.iapws.org.

Jang, D. S., et al. “Comparison Of The Piso, Simpler, And Simplec Algorithms For The Treatment Of The Pressure-Velocity Coupling In Steady Flow Problems.” *Numerical Heat Transfer*, vol. 10, no. 3, 1986, pp. 209–228., doi:10.1080/10407788608913517.

Jespersen, Dennis C. *Acceleration of a CFD Code with a GPU*. NASA, 2009, pp. 1–10, *Acceleration of a CFD Code with a GPU*.

Koester, S., et al. “Modeling Heat and Mass Transfer in Cross-Counterflow Enthalpy Exchangers.” *Journal of Membrane Science*, vol. 525, 2 Nov. 2016, pp. 68–76., doi:10.1016/j.memsci.2016.10.030.

Lee, Eul-Jong, et al. “Moisture Transfer Characteristics of a LiCl-Impregnated Paper Membrane Used for an Enthalpy Exchanger.” *Journal of Mechanical Science and Technology*, vol. 27, no. 5, 6 Dec. 2012, pp. 1527–1537., doi:10.1007/s12206-013-0333-2.

Mara Air. *“ERV Installation*”. 21 Apr. 2015, www.maraair.com/heat-recovery-ventilator-hrv/hrv1/.

Markets & Markets, *“Energy Recovery Ventilator Market by Technology Type (Plate Heat Exchanger, Heat Pipe Heat Exchanger, Rotary Heat Exchanger, Run-Around Coil), Application (Commercial, Residential), and Region (NA, EU, APAC, MEA, SA) - Global Forecast to 2022”*, 2017.

Min, Jingchun, and Jiangfei Duan. “Membrane-Type Total Heat Exchanger Performance with Heat and Moisture Transferring in Different Directions across Membranes.” *Applied Thermal Engineering*, vol. 91, 10 Sept. 2015, pp. 1040–1047, doi:10.1016/j.applthermaleng.2015.09.001.

Min, Jingchun, and Ming Su. “Performance Analysis of a Membrane-Based Energy Recovery Ventilator: Effects of Membrane Spacing and Thickness on the Ventilator Performance.” *Applied Thermal Engineering*, vol. 30, no. 8-9, 15 Jan. 2010, pp. 991–997, doi:10.1016/j.applthermaleng.2010.01.010.

Min, Jingchun, and Ming Su. “Performance Analysis of a Membrane-Based Enthalpy Exchanger: Effects of the Membrane Properties on the Exchanger Performance.” *Journal of Membrane Science*, vol. 348, no. 1-2, 14 Nov. 2010, pp. 376–382., doi:10.1016/j.memsci.2009.11.032.

National Instruments. “NI 9205 16 AI Differential/32 AI Single-Ended, ±200 mV to ±10 V, 16 Bit, 250 kS/s Aggregate Datasheet” National Instruments. <http://www.ni.com/pdf/manuals/374188a_02.pdf>

National Instruments. “NI 9213 16 TC, ±78 mV, 24 Bit, 75 S/s Aggregate Datasheet”. National Instruments. <http://www.ni.com/pdf/manuals/374916a_02.pdf>

National Instruments. “NI 9263 4 AO, ±10 V, 16 Bit, 100 kS/s/ch Simultaneous Datasheet” National Instruments. http://www.ni.com/pdf/manuals/373781b_02.pdf

National Instruments. “NI cDAQ-9174. NI CompactDAQ Four-Slot USB Chassis Datasheet” National Instruments. <http://www.ni.com/pdf/manuals/374045a.pdf>

Navigant Research, “*Indoor Air Quality Monitoring and Management in Smart Buildings*.” Energy Recovery Ventilation Systems Will Reach Nearly $3 Billion in Annual Revenue by 2020. 12 Aug. 2014.

O. Reynolds. An Experimental Investigation of the Circumstances Which Determine Whether the Motion of Water Shall be Direct or Sinuous, and the Law of Resistance in Parallel Channels, Philosophical Transactions of the Royal Society of London 174, 935-982 (1883).

Omega. *ANSI and IEC Color Codes for Thermocouples, Wire and Connectors*. www.omega.com/temperature/pdf/tc_colorcodes.pdf.

Sebai, R., et al. “Cross-Flow Membrane-Based Enthalpy Exchanger Balanced and Unbalanced Flow.” *Energy Conversion and Management*, vol. 87, 18 July 2014, pp. 19–28., doi:10.1016/j.enconman.2014.07.002.

United States, Congress, “Annual Energy Outlook 2015 with Projections to 2040.” *Annual Energy Outlook 2015 with Projections to 2040*, U.S Energy Information Administration, 2015, pp. 1–154.

United States, Congress, Energy Star. “ENERGY STAR Technical Specifications for Residential Heat-Recovery Ventilators and Energy-Recovery Ventilators (.” *ENERGY STAR Technical Specifications for Residential Heat-Recovery Ventilators and Energy-Recovery Ventilators (*, Energy Star, 2009.

Woods, Jason, and Eric Kozubal. “Heat Transfer and Pressure Drop in Spacer-Filled Channels for Membrane Energy Recovery Ventilators.” *Applied Thermal Engineering*, vol. 50, no. 1, 23 Aug. 2013, pp. 868–876. doi:10.1016/j.applthermaleng.2012.06.052.

Yoo, Seung Mi, and Raja Ghosh. “A Method for Coating of Hollow Fiber Membranes with Calcium Alginate.” *Journal of Membrane Science*, vol. 558, 27 Apr. 2018, pp. 45–51., doi:10.1016/j.memsci.2018.04.044.

Zhang, L, et al. “Heat and Moisture Transfer in Application Scale Parallel-Plates Enthalpy Exchangers with Novel Membrane Materials.” *Journal of Membrane Science*, vol. 325, no. 2, 1 Sept. 2008, pp. 672–682., doi:10.1016/j.memsci.2008.08.041.

Zhang, L.-Z., et al. “Selective Permeation of Moisture and VOCs through Polymer Membranes Used in Total Heat Exchangers for Indoor Air Ventilation.” *Indoor Air*, vol. 22, no. 4, 29 Nov. 2011, pp. 321–330., doi:10.1111/j.1600-0668.2011.00762.x.

Zhang, Li-Zhi. “Heat and Mass Transfer in a Quasi-Counter Flow Membrane-Based Total Heat Exchanger.” *International Journal of Heat and Mass Transfer*, vol. 53, no. 23-24, 2010, pp. 5478–5486., doi:10.1016/j.ijheatmasstransfer.2010.07.009.

Zhang, Li-Zhi. “Heat and Mass Transfer in Plate-Fin Enthalpy Exchangers with Different Plate and Fin Materials.” *International Journal of Heat and Mass Transfer*, vol. 52, no. 11-12, 2009, pp. 2704–2713., doi:10.1016/j.ijheatmasstransfer.2008.12.014.

Airxchange. “Acceptable Cross Leakage for Energy Recovery Ventilation According to ASHRAE Standard 62.1.” *Airxchange Tech Note*, 2005, Acceptable Cross Leakage for Energy Recovery Ventilation According to ASHRAE Standard 62.1.

Espinosa, F.a. Dominguez, and Leon R. Glicksman. “Determining Thermal Stratification in Rooms with High Supply Momentum.” *Building and Environment*, vol. 112, 14 Nov. 2016, pp. 99–114., doi:10.1016/j.buildenv.2016.11.016.

Feigley, Charles E., et al. “Performance of Deterministic Workplace Exposure Assessment Models for Various Contaminant Source, Air Inlet, and Exhaust Locations.” *AIHA Journal*, vol. 63, no. 4, 2002, pp. 402–412., doi:10.1080/15428110208984728.

Hooff, T. Van, et al. “On the Suitability of Steady RANS CFD for Forced Mixing Ventilation at Transitional Slot Reynolds Numbers.” *Indoor Air*, vol. 23, no. 3, 2012, pp. 236–249., doi:10.1111/ina.12010.

Khan, J.a., et al. “Effects of Inlet and Exhaust Locations and Emitted Gas Density on Indoor Air Contaminant Concentrations.” *Building and Environment*, vol. 41, no. 7, 26 May 2005, pp. 851–863., doi:10.1016/j.buildenv.2005.04.002.

Lee, Eungyoung, et al. “An Investigation of Air Inlet Types in Mixing Ventilation.” *Building and Environment*, vol. 42, no. 3, 3 Jan. 2006, pp. 1089–1098., doi:10.1016/j.buildenv.2005.11.006.

Mainkar, Millind, et al. “Thermal Mixing of Outdoor and Return Airflows in Typical Air-Handling Units.” *ASHRAE Transactions: Research*, 2004, pp. 194–205.

Ponschok, David. “Heat Recovery Ventilator(HRV) vs Energy Recovery Ventilator(ERV): What's the Right Unit for Your Home?” *EP Sales Inc.*, 2 Aug. 2018, www.epsalesinc.com/heat-recovery-ventilator-hrv-vs-energy-recovery-ventilator-erv-whats-right-unit-home/.

Zehnder. *Zehnder External Wall Grille Specifications*. Zehnder America, 16 Sept. 2019, zehnderamerica.com/wp-content/uploads/2019/09/Zehnder-External-Grille-specification-2019.09.16.pdf.

APPENDIX A

CALCULATION OF WATER VAPOR PARTIAL PRESSURES

The water-vapor pressure is the partial pressure of the water vapor in a gas mixture, which is standard air in this research, and it can be determined by using Equation 2, the Antoine equation, derived by Louis Charles Antoine, in 1888 from the Clausius-Clapeyron relation with constants *A*, *B* and *C* being presented in Table 1.

$$\log_{10} P = A - \frac{B}{C+T} \tag{2}$$

Table 32: Antoine Equation Constants

A	***B***	***C***	***T_min*, °C**	***T_max*, °C**
8.07131	1730.63	233.426	1	99
8.14019	1810.94	244.485	100	374

Several equations for determining water vapor saturation pressure have been introduced since with ever increasing accuracy. According to the ASHRAE Handbook-Fundamentals 2017, the saturation pressure over ice for the temperature range of -148°F to 32°F is given by Equation 3, and the saturation pressure over water for the temperature range of 32°F to 392°F is given by Equation 4 with constants C_1 through C_{13} being defined in Table 2.

$$ln p_{ws} = {C_1}/{T} + C_2 + C_3 T + C_4 T^2 + C_5 T^3 + C_6 T^4 + C_7 ln T \tag{3}$$

$$ln p_{ws} = {C_8}/{T} + C_9 + C_{10} T + C_{11} T^2 + C_{12} T^3 + C_{13} ln T \tag{4}$$

Table 33: ASHRAE Handbook Saturation Pressure Equations (2)

Constants for Equation 2	***Constants for Equation 3***
$C_1 = -1.0214165 \cdot 10^4$	$C_8 = -1.0440397 \cdot 10^4$
$C_2 = -4.8932428$	$C_9 = -1.1294650 \cdot 10^1$
$C_3 = -5.3765794 \cdot 10^{-3}$	$C_{10} = -2.7022355 \cdot 10^{-2}$
$C_4 = 1.9202377 \cdot 10^{-7}$	$C_{11} = 1.2890360 \cdot 10^{-5}$
$C_5 = 3.5575832 \cdot 10^{-10}$	$C_{12} = -2.4780681 \cdot 10^{-9}$
$C_6 = -9.0344688 \cdot 10^{-14}$	$C_{13} = 6.5459673$
$C_7 = 4.1635019$	

Equations 2 and 3 are within 300 ppm of the most recent International Association for the Properties of Water and Steam (IAPWS) formulas and are adequate for the scope of this research (IAPWS 2011).

It is important to note that the previous three equations provide saturated water vapor pressure that can in turn be used to calculate the actual water vapor partial pressure if the relative humidity (RH) is known. Specifically, RH is the ratio of actual water-vapor partial pressure, which is important for determining the driving water vapor pressure difference across the membrane, and the maximum partial pressure or saturation pressure that can be calculated from Equation 1 through 3 saturation pressure.

APPENDIX B

TEMPERATURE MEASUREMENTS

Airflow temperature measurements for the experimental tests were obtained using Type-T thermocouples, specifically thermocouple grade wires were used with the positive terminal consisting of copper and the negative terminal composed of a copper-nickel alloy. The maximum temperature range is rated from -454 to 752°F (-270 to 400°C) while the useful temperature range is listed as -328 to 662°F (-250 to 350°C). Type T thermocouples were selected in part due to the wide temperature range, but primarily due to their high accuracy as summarized in Table 34 (Omega, ASTM).

Table 34: Thermocouple Tolerance and Range

	Standard Limits		**Special Limits**	
Temp. Range	>32 to 662°F	>0 to 350°C	32 to 662°F	0 to 350°C
Tolerance*	1.8°F or 0.75%	1.0°C or 0.75%	1.0°F or 0.40%	0.5°C or 0.40%
Temp. Range	-328 to 32°F	-200 to 0°C		
Tolerance*	1.8°F or 1.5%	1.0°C or 1.5%		

The thermocouple grade wires employed in this research possess the special limits of error. Because all testing was conducted above 32°F (0°C), the accuracy is the greater of 1.0°F (0.5°C) or 0.4%. Using a 0.4% error calculation on the highest temperatures recorded, the values are approximately 0.5°F, and thus 1.0°F is used for all thermocouple error and uncertainty calculations.

Strictly for thermocouple measurements, the National Instruments 9213 I/O module can collect data from the Type-T thermocouples used in this research. When operated in high-resolution mode, the accuracy is <0.02°C with a gain error of 0.03%. While no exact value is given for error at a specific temperature, Figure 86 shows the measurement error for Type-T thermocouples under various operating conditions.

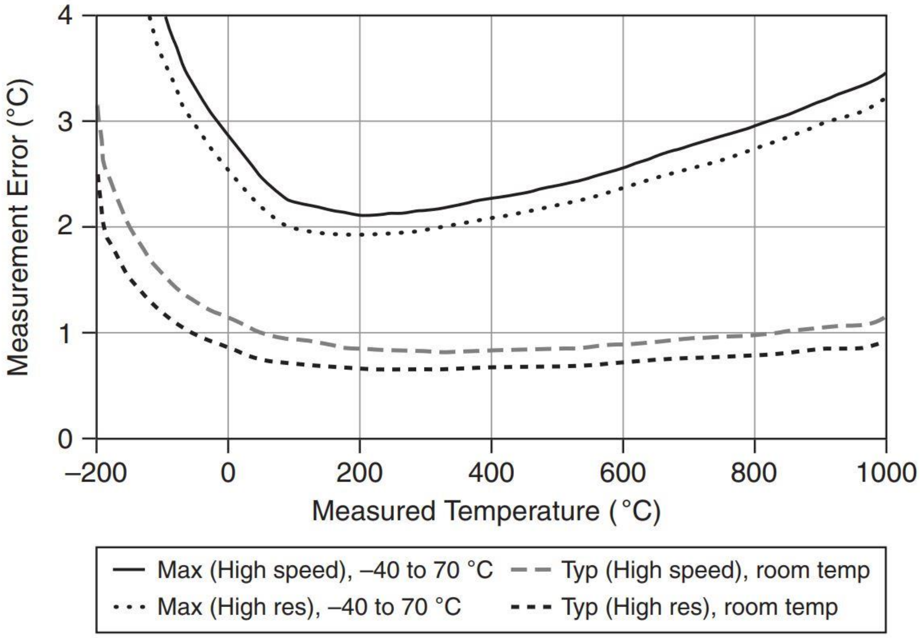

Figure 86: National Instruments 9213 Measurement Error

Figure 86 accounts for “gain errors, offset errors, differential and integral nonlinearity, quantization errors, noise errors, 50Ω lead wire resistance, and cold-junction compensation errors” (National Instruments). The NI 9213 is operated in high-resolution for this research and thus it is reasonable to expect a maximum measurement error of 1.35°F (0.75°C) for the temperature conditions measured, namely between 70 and 105°F (21.2 to 40.6°C).

Humidifier

The Aprilaire 801 Modulating Humidifier is used for the humidification of the ambient laboratory air to a specific setpoint and it was chosen due in part to its self-modulating abilities, which allows the operator to set a desired relative humidity in the controller. A continuous feedback loop relies on a humidity sensor and thermistor downstream to fix the steam output in order to maintain a constant relative humidity. The 801 humidifier is wired for 240V/16A which is capable of outputting up to 21 gallons per day with a 20 foot long steam hose (Aprilaire). In addition, the dispersion or absorption distance for the steam is classified as a maximum of 60” from the insertion point, with the current setup being 84” from insertion point to the humidity sensor. Figure 87 shows the humidifier installed next to the control panel. The steam is expelled from the top through the steam hose while drainage and water inlets are on the bottom.

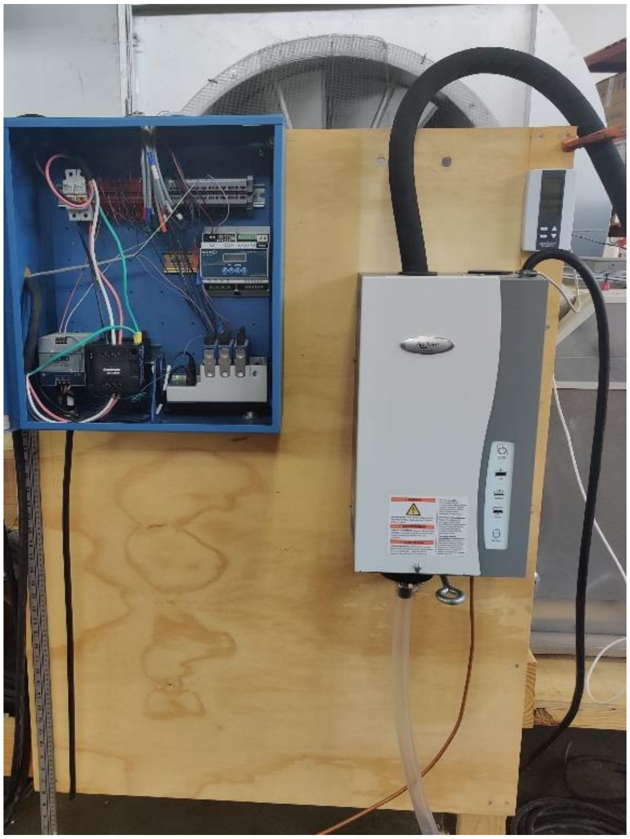

Figure 87: Humidifier Installation

Process Duct Heater

The second major piece of equipment for the experimental facility is the selection and installation of a process duct heater capable of increasing the temperature of ambient intake air to 110°F, which depending on laboratory conditions can be as much as a 50°F delta. In conjunction with the airflow required the anticipated energy in Btu's and kW's required to heat the air can be seen in Equation 7 and Equation 8, respectively (Chromalox).

$$P = Q \cdot \rho \cdot C_p \cdot \Delta T \qquad (7)$$

$$P = \frac{Q \cdot \rho \cdot 60 \cdot C_p \cdot \Delta T}{3412\ Btu/kW} \qquad (8)$$

where,

P = Minimum required process heater power in Btu or kW

Q = Volumetric flow-rate of air (ft^3/min)

ρ = Density of air at initial inlet conditions (lb/ft^3)

C_p = Specific heat of air at initial temperature (Btu/lb·°F)

ΔT= Temperature change (°F)

Taking into account values of 0.07631 for density and 0.2402 for specific heat, along with the maximum volumetric flow rate of 250 cfm the calculated heater requirement is 4.03 kW, and applying a 20% safety factor results in 4.83kW. Because process heaters are not sold in fractional kW values and to allow expansion to higher flow-rate testing, a 6kW heater was selected from Tempco, model TDH01005. This heater operates on 3 phase 480V with an approximate maximum amperage pull of 12.5. Figure 88 shows the installation of the process heater in the intake duct.

Figure 88: Process Heater Installation

Also visible in the above figure is the outlet from the steam humidifier, as depicted by the angled tube near the bottom of the duct. In conjunction with the process heater there were several control mechanisms procured to set the inlet air temperature.

The operation of the Tempco TDH01005 was controlled via a Proportional-Integral-Derivative (PID) controller used in conjunction with a Silicon Controlled Rectifier (SCR) power controller. A SCR power controller, namely the Watlow SCR B 3ph 277-600VAC, was chosen over a less expensive electro-mechanical contactor due to the myriad of benefits associated with SCR controllers, namely extremely fast switching (milliseconds) and the ability to eliminate potential Radio Frequency Interference (RFI), harmonics and arcing (Advanced Energy).

The method of controlling the signal sent to the SCR power controller is via a PID controller, namely the Watlow EZ-Zone PM, which allows the operator to set a desired temperature on the controller which is then compared to a reading obtained from an RTD placed in the flow stream. The PID controller initiates a continuous feedback loop to match the RTD to the set point by applying a signal to the SCR controller which in turn applies current to the process heater.